

Mini Review

Open Access



Recent advances in alloying anode materials for sodium-ion batteries: material design and prospects

Ata-ur Rehman¹ , Sanum Saleem², Shahid Ali¹ , Syed Mustansar Abbas³ , Minsu Choi⁴, Wonchang Choi^{4,*}

¹Interdisciplinary Research Center for Hydrogen Technologies and Carbon Management, King Fahd University of Petroleum and Minerals, Dhahran 31261, Saudi Arabia.

²National Metrology Institute of Pakistan, Islamabad 44800, Pakistan.

³Nanoscience and Technology Department, National Centre for Physics, Islamabad 45320, Pakistan.

⁴Department of Energy Engineering, Konkuk University, Gwangjin-gu, Seoul 05029, Republic of Korea.

Correspondence to: Prof. Wonchang Choi, Department of Energy Engineering, Konkuk University, Neungdong-ro 120, Gwangjin-gu, Seoul 05029, Republic of Korea. E-mail: wcchoi@konkuk.ac.kr

How to cite this article: Rehman Au, Saleem S, Ali S, Abbas SM, Choi M, Choi W. Recent advances in alloying anode materials for sodium-ion batteries: material design and prospects. *Energy Mater* 2024;4:400068. <https://dx.doi.org/10.20517/energymater.2024.06>

Received: 22 Jan 2024 **First Decision:** 12 Apr 2024 **Revised:** 28 May 2024 **Accepted:** 19 Jun 2024 **Published:** 12 Jul 2024

Academic Editors: Cheol-Min Park, Wei Tang **Copy Editor:** Fangyuan Liu **Production Editor:** Fangyuan Liu

Abstract

Sodium-ion batteries (SIBs) are close to commercialization. Although alloying anodes have potential use in next-generation SIB anodes, their limitations of low capacities and colossal volume expansions must be resolved. Traditional approaches involving structural and compositional tunings have not been able to break these lofty barriers. This review is devoted to recent progress in research on alloy-based SIB anodes comprising Sn, Sb, P, Ge, and Si. The current level of understanding, challenges, modifications, optimizations employed up to date, and shortfalls faced by alloying anodes are also described. A detailed future outlook is proposed, focusing on advanced nanomaterial tailoring methods and component modifications in SIB fabrication. Utilizing the latest state-of-the-art characterization techniques, including *ex-situ* and *operando* characterization tools, can help us better understand the (de)sodiation mechanism and accompanying capacity fading pathways to pave the way for next-generation SIBs with alloying anode materials.

Keywords: Alloying, anodes, sodium-ion batteries, volume expansion, optimizations



© The Author(s) 2024. **Open Access** This article is licensed under a Creative Commons Attribution 4.0 International License (<https://creativecommons.org/licenses/by/4.0/>), which permits unrestricted use, sharing, adaptation, distribution and reproduction in any medium or format, for any purpose, even commercially, as long as you give appropriate credit to the original author(s) and the source, provide a link to the Creative Commons license, and indicate if changes were made.



INTRODUCTION

Sodium-ion batteries (SIBs) have recently drawn attention as current lithium reservoirs are depleting which poses severe supply issues. This situation is further complicated due to polarization of the world's primary energy economies^[1,2]. Although energy density supplied by current generation lithium-ion batteries (LIBs) is fascinating, many other competitors have joined this race and gained subtle success at lower costs and higher safety, including SIBs^[3], lithium-sulfur^[4], Zinc-ion^[5], alkaline metal^[6], solid-state^[7], metal air^[8], redox flow batteries^[9], and supercapacitors^[10]. Each of these systems offers some advantages in terms of capacity, energy and power density, benignity, safety, and longevity. At the same time, each has certain limitations that need to be fixed soon to delimit their potential^[11,12]. Although battery systems with metallic anodes and sulfur cathodes offer ideal performances, they suffer from serious issues presently^[13-15]. SIBs share the same components and design assembly as LIBs but with different materials and kinetics. However, the larger ionic radius and molar mass of Na^+ than Li^+ pose more restrictions whereby the higher redox potential of Na results in lower energy density and theoretical capacity ($1,166 \text{ mA g}^{-1}$ for Na and $3,861 \text{ mAh g}^{-1}$ for Li)^[16,17]. From a cost perspective, lithium mineral ore price is highly fluctuating, with a 2023 price of around 7,000 Euro/Ton. Its price is expected to increase, although the energy per ton price is speculated to remain stagnant. However, it remains difficult to predict its price due to highly fluctuating geopolitical situations in the world^[18-20]. Nevertheless, the high abundance of sodium with uniform distribution across the globe presents much cheaper alternatives to LIBs. In addition, cell assembly for SIBs uses cheaper current collectors, i.e., Al foil, which is not compatible with LIBs anode due to Li-Al alloy formation^[21,22]. The compatibility of highly ionic conductive and safe electrolyte additives in SIBs has also opened future gateways for high-rate and wide temperature-sustaining batteries, particularly for grid-scale applications.

SIB anodes have potential to be explored for high capacity with several advantages along with a diverse selection of materials offering multiple mechanisms and optimization possibilities. Therefore, they have opened a wide research window for optimized SIB performance. Notably, graphite, a recognized commercial LIB anode, has a mismatched size for Na^+ shuttling. The low capacity and unstable performance behavior of current SIB anodes have impeded their commercialization^[3,23]. SIB anodes can be categorized into three basic types based on the prevailing Na^+ storage mechanism: intercalation, alloying, and conversion-type^[24].

Although research on SIBs was initially started with LIBs in the 1990s, the much higher performance of LIBs than SIBs has left little admiration for the advancement of SIBs^[25]. Recent improvements in SIB capacity have been bestowed by nanoengineering and adopting advanced tools for material performance with *in-situ* and postmortem analysis of SIB cells. These adaptabilities have let a paradigm focus on SIB advancements for next-generation batteries. Appreciably, many emerging cathodes, such as NaCoO_2 , NaMnO_2 , $\text{P2-Na}_{0.66}[\text{Ni}_{0.33}\text{Mn}_{0.66}]\text{O}_2$, $\text{NaV}_6\text{O}_{18}$, $\text{Na}_3\text{V}_2(\text{PO}_4)_3$ (NVP), and others, have shown promise for coupling with SIB anodes to provide a working potential in the range of 3-4 V and a capacity of 100-200 mAh g^{-1} ^[26]. However, metallic sodium, as an anode in SIBs, is currently not plausible due to immense dendrite formation, highly unstable solid electrolyte interphase (SEI), and other side reactions^[7,27]. Meanwhile, alloying anodes promise higher capacity provision than conversion and intercalating anodes. Still, significant volumetric changes can lead to pulverization, electrical contact loss, and huge capacity fading while also parting to slow down the kinetics. Thus, one of the front-line challenges in commercializing next-generation SIBs is finding a suitable alloying material as an SIB anode that can overcome these challenges without compromising capacity or efficiency in the long run^[28]. Targeting these limitations, many approaches, including nano-structural modifications, carbon coating, and introducing binary/ternary alloys and hybrids, have been adopted^[29,30].

There is no doubt that carbon materials have become the foremost choices as SIB anode materials. The incompatibility of the interlayer spacing of graphite for intercalation of large-sized Na^+ has given room for expanded graphitic carbon and hard carbon for opting as SIB anode materials. Interestingly, they are proven to be viable as SIB anode materials. In fact, hard carbon from various sources, including biomass-derived hard carbon, has been widely searched for an optimum capacity for delivering SIB anodes^[3,31-37]. The high porosity of carbonaceous materials helps sustain a high capacity by introducing more Na^+ in pores^[34,38,39].

Although diverse efforts have been devoted to the incorporation of defects and functionalities in carbonaceous materials for improved performances of SIB anodes as their effects on capacity and overall performance enhancement are evident in many instances, their participation in capacity-fading pathways hinders their benefits^[40,41]. For example, the trapping and reaction of Na^+ with defects in functionalities often lead to capacity fading, particularly in initial cycles, contributing to trap effect and some irreversible capacity loss over long cycling. Still, their role in capacity fading has not yet been unveiled^[42-44]. Although there are diverse approaches of doping in carbon to generate heterogenous surfaces and compositing these carbonaceous materials to alloying anode materials that bear both intrinsic and extrinsic defects, their participation in side reactions demands close monitoring to have an optimized performance. Also, in some instances, these defects *in-situ* generated during (dis)charging cycles remain undetected due to non-utilization of conclusive mechanistic approaches^[3,17,45]. Although many modifications have been made for carbonaceous anodes, none has fully satisfied the standard of a commercial SIB anode^[34,46-49]. This has led to a recent shift towards alloying and conversion/alloying anode materials that show more promise for high-energy-density SIBs.

While conversion-type anodes, including transition metal compounds such as oxides^[50], sulfides^[51], selenides^[52], tellurides^[53], phosphides^[54], and so on, have been widely focused, they have not achieved performance targets. Amongst all, alloying-type materials that mainly include Sn, Sb, Si, Ge, and P are the most explored SIB anode materials^[24,48]. Although these anode materials have high theoretical sodiation capacity, the alloying reaction ($x\text{Na}^+ + xe^- + M \rightleftharpoons \text{Na}_xM$) often results in high accompanying volume expansions, leading to severe pulverization and low capacity. Fully alloyed compositions with theoretical capacity, volume expansion, and average voltage are summarized in Table 1.

Although breakthrough has not been achieved yet, their extreme performance potentials have been extensively focused on as they can deliver very high and stable capacities^[55]. Many developments have recently been made to improve capacities of alloying SIBs, including electrode materials, morphologies, electrolytes, and binder modulations^[17,29,56-59]. Although hundreds of research papers have been added to the literature on alloying SIB materials in the past few years, unfortunately, no recent review has solely covered recent progress on alloying SIB anodes. Therefore, a comprehensive overview of research developments, particularly during the last six years, which are uniquely devoted to alloying anodes, namely Sn, Sb, P, Ge, and Si, is needed.

This review paper addresses alloy materials in five main sections: (1) Alloy-based Anodes for Sodium-Ion Batteries; (2) Materials Design Strategies; (3) Challenges Associated with Sodium-Ion Batteries; (4) Optimizations of Sodium-Ion Batteries; and (5) Summary and Future Prospects. In detail, the current review focuses on recent trends in material design strategies employed to have efficient SIB alloying anodes with details of unresolved challenges, such as initial huge capacity fading accompanied by multifold volume variations. Lastly, various modifications adapted to cope with challenges faced by alloying SIB anodes are briefly detailed, followed by concrete recommendations for future research. In this regard, using advanced characterization tools to unveil the mechanism through spatial and temporal tracing of species evolved during the de(alloying) process is highly encouraged to sustain alloying SIB materials.

Table 1. Various parameters (volume expansion, average voltage, and theoretical capacity) for sodiation reactions of alloy-based materials

| Metal | Alloyed compositions | Volume expansion (%) | Average voltage (vs. Na/Na ⁺) (V) | Theoretical capacity (mAh g ⁻¹) |
|-------|----------------------------------|----------------------|---|---|
| Si | NaSi/Na _{0.75} Si | 114 | -0.50 | 954/725 |
| Sn | Na ₁₅ Sn ₄ | 420 | -0.20 | 847 |
| Ge | NaGe | 205 | -0.30 | 576 |
| Sb | Na ₃ Sb | 390 | -0.60 | 660 |
| Bi | Na ₃ Bi | 250 | -0.55 | 385 |
| P | Na ₃ P | > 300 | -0.40 | 2,596 |

ALLOY-BASED ANODES FOR SIBS

Tin-based anodes for siBs

Tin (Sn) is an incredible choice as an anode material in SIBs because of its high theoretical capacity (847 mAh g⁻¹), good electrochemical performance, high electric conductivity (9.17×10^4 Scm⁻¹), environment friendliness, and relative abundance. In SIBs, varying alloying constitution ability of Sn has been reported. The number of sodium ions participating in the alloying reaction can reach 3.75 to form Na₁₅Sn₄ in a multistep sodiation process. Moreover, the high affinity of Sn-based materials with Na⁺ ions has motivated researchers to investigate other Sn-based materials such as their oxides, sulfides, selenides, phosphides, and composites^[24,60,61]. Despite their high theoretical capacity, Sn anodes face serious challenges. The foremost problem is the pulverization of active material due to colossal volume expansion (420%) during the alloying/dealloying process that, along with unstable SEI formation, can reduce the initial Coulombic efficiency (ICE) and overall capacity^[62,63]. Spontaneous particle aggravation during (de)sodiation can induce large Na⁺ migration paths, further hindering Na⁺ transfer kinetics^[64]. To address these drawbacks, researchers have adopted various strategies to present Sn-based materials as alternative SIB anodes, including nanosizing, mixing with conductive matrixes, heteroatom doping, and heterostructuring with additional modifications in selecting suitable electrolytes and additives^[28,65-68]. The most common modification is formation of an Sn-C nanocomposite by introducing a C matrix, such as the recently prepared freestanding Sn-based electrode comprising spherical Sn particles ingrained in carbon nanofibers (CNFs). When electrochemical performances of carbonate and ether-based electrolytes were compared, poor rate performance was observed when carbonate electrolytes were used. An outstanding cycling performance of 30,000 cycles with a capacity of 662 mAh g⁻¹ at 0.5 C has been achieved by utilizing dimethyl ether (DME) electrolyte^[69]. A μ -Sn anode for SIBs has recently been evaluated using operando scanning electron microscopy (SEM) and X-ray absorption spectroscopy (XAS) to reveal volume variations and structural evolutions during initial and extended cycling. Although some voids and volume expansion were formed, using ether-based electrolytes could overcome these drawbacks to achieve a high ICE of 91.3% with a capacity above 400 mAh g⁻¹ after 20 cycles^[70]. Many other ways have been proposed to improve the performance of Sn anodes for SIBs. For example, inclusion of K⁺ in the electrolyte can highly improve the performance of Sn alloying anodes, yielding an energy of 565 mAh g⁻¹ over 3,000 cycles at 2 A g⁻¹^[71]. Similarly, the utilization of a cross-linked binder has been proposed in a μ -Sn anode for SIB to ensure a high ICE and an extra-long cycle life with an improved capacity^[72]. Other approaches include presodiation and intermetallic formulations with potential to uplift the capacity of Sn anodes in SIBs^[61,73,74].

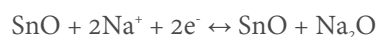
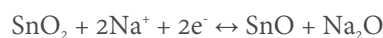
μ γñōp̄p̄= œ õy õñ ò p̄oy ÿ öýýõáññõñ ãñ ãp̄ý á œõùœ ÿ ñõ ñp̄õõ
 ãõ ȳp̄õñ ùñȳp̄ ùýýõñ ñ <¹ý p̄ ñp̄õñ ñp̄-õññõ ñ ñp̄õ ãñ p̄ññp̄ȳõ ù
 ñp̄p̄ȳȳȳ öýȳ= p̄oy ýñõ ùññ ñ ȳp̄ùý-çp̄oy ãññȳp̄ ýý ñ ùñññp̄-õ ññõõ

commonly exploited SIB anodes^[75]. Effective surface tuning of this anode enabled it to deliver a good capacity for 10 k cycles. When this anode was employed in full cell (taking NVP as the cathode), the cell delivered an energy density of 215 Wh Kg⁻¹ over a broad temperature range of -20 to 50 °C. The floret-like 3D morphology with improved Na⁺ diffusion kinetics and high sodium affinity has dually been validated by density functional theory (DFT) calculations. Moreover, their findings also support the formation of a stable hybrid SEI of diethylene glycol dimethyl ether (DEGDME) with inorganic fluoride-rich ionic conductive polyether electrolyte to achieve a capacity of 347 mAh g⁻¹ at 2 A g⁻¹ retained for 10,000 cycles. Such marvelous performance has left behind many other strategies and opened a new door for exploring new electrolyte formulations. The flair of DEGDME for better compatibility with NaPF₆ has been proven by DFT calculations that show a higher energy difference for electron promotion from the highest occupied molecular orbital (HOMO) to the lowest unoccupied molecular orbital (LUMO) than in commonly employed carbonate-based electrolytes.

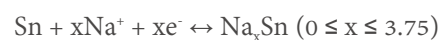
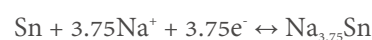
Tin-based oxides

Tin oxide is a promising class of anodic materials for SIBs owing to its intriguing features such as abundance, low toxicity, and high theoretical capacity. Tetragonal tin dioxide (SnO₂) and orthorhombic tin monoxide (SnO) are two main types of tin-based oxides. SnO has a layered structure with a Sn-O-Sn sequence. Its large spacing between layers allows easy insertion and extraction of Na⁺. The reaction mechanism of conversion and alloying is given as follows:

Conversion reactions:



Alloying reaction:



Due to their dual conversion and alloying reactions with Na⁺, high theoretical specific capacities of 1,375 and 1,150 mAh g⁻¹ are achieved for SnO₂ and SnO, respectively. However, the low reversibility of the conversion reaction can lead to rapid capacity declination during initial cycles that additionally suffer from large volume change and the low electrical conductivity of tin-based oxides hamper their practical applications. One effective strategy is by forming a hybrid, often involving designing a structure with nanosized tin oxides and combining it with nanostructures such as nanofibers (NFs), nanosheets, nanoflowers, yolk shells, and so on^[24]. Zhang *et al.* have prepared a flexible fibrous composite of CNFs decorated with N-doped carbon nanotubes (CNTs) and SnO₂ nanoparticles as bare nanostructured SnO₂ is prone to fracture and detachment from the conductive matrix, which loses electronic contact during an electrochemical reaction^[76]. Processed anodes can deliver a highly stable cycling performance and impressive rate capabilities for SIBs. The optimized composite showed a discharge capacity of 460 mAh g⁻¹ after 200 cycles and 222.2 mAh g⁻¹ at a high current density of 3.2 A g⁻¹. The continuous fibrous structure gave additional stability to the anode, thus retaining its fibrous morphology during sodiation/desodiation.

Oxygen vacancy creation in active nanostructures often can improve capacity and charge transfer kinetics. It has been observed that in SnO_2 , these vacancies could enhance Na^+ storage capacity and increase electrical conductivity. Oxygen vacancies can also cope well with volume changes in the process of (de)sodiation, improve the cyclic stability of SnO_2 anodes, and extend the lifespan of batteries. Ma *et al.* have utilized these oxygen vacancies effectively to present oxygen vacancy-bearing SnO_{2-x} and combine it with porous CNFs (PCNF) to construct a homogeneously confined nanoparticles ($\text{SnO}_{2-x}/\text{C}$) composite^[77]. The prepared composite was directly used as an anode without a binder or other conductive additives for SIBs. It displayed superb electrochemical properties including high reversible capacity, sustaining rate capability, and ultra-long cyclic stability even after thousands of cycles. The discharge capacity of 565 mAh g^{-1} over 2,000 cycles at 1 A g^{-1} was attained, whereas the bare SnO_2 showed a meager capacity retention of 57 mAh g^{-1} after 800 cycles. Heterostructure methodology along with C compositing is a promising approach to enhancing the cyclic capacity of electrode materials in SIBs. One such approach has been adopted by Fan *et al.* by preparing a SnO_2/N -doped graphene (SnO_2/NG) composite^[78]. Strong coupling between N-doped graphene and Sn^{4+} is developed because additional active sites are created due to doping. Optimal nitrogen doping level also enhanced reversible capacities and rate capabilities over un-doped anodes. SnO_2/NG composite with a high level of pyridinic-N (1.97%) gave an outstanding reversible capacity of 409.6 mAh g^{-1} at 50 mA g^{-1} over 100 cycles. It also presented superior rate capabilities of 416.5, 366.9, and 318.7 mAh g^{-1} at 200, 400, and 800 mA g^{-1} , respectively. Such outstanding electrochemical performance of the obtained composite is due to low electrochemical effects, polarization effects, and entrusting high Na^+ diffusion.

A unique composite structure of 1D ultrafine SnO_2 nanorods and 3D graphene aerogel ($\text{SnO}_2\text{NRs/GA}$) has been fabricated by a reduction-induced self-assembly method. Vitamin C was used to facilitate the reduction of graphene oxide (GO). The combination of 3D aerogel and 1D SnO_2 nanorods resulted in a synergistic effect that improved electrochemical performance of the material^[79]. As an SIB anode, the material delivered an initial discharge capacity of 232 mAh g^{-1} at 0.02 A g^{-1} in 100 cycles. The composite ($\text{SnO}_2 \text{NRs/GA}$) also demonstrated excellent cycling stability as an SIB anode, with a high reversible capacity of 96 mAh g^{-1} at a high current density of 1 A g^{-1} for 500 cycles. Demir *et al.* have demonstrated that an *in-situ* formulated $\text{SnO}_2@$ hard carbon obtained by hydrothermal carbonization methodology using bio-waste of apricot shells can be utilized for high-performance anodic material in SIBs^[80]. It was observed that the $\text{SnO}_2@$ hard carbon anode derived at $1,000^\circ\text{C}$ could effectively uptake more Na^+ ions and sustain a capacity of 184 mAh g^{-1} over 250 cycles than the corresponding anode obtained by mechanically mixing SnO_2 and hard carbon.

An amorphous tin oxide (a-SnO_x) with a nano-helical structure containing extended defects has been prepared via a solution and surfactant-free oblique angle deposition method (as shown in Figure 1A and B)^[81]. The challenging task is that such morphologies are not achievable by conventional methods that require heating materials to remove any remaining solvent or other additives that cause subtle structural damage to the amorphous phase. The low oxidation state of tin oxide in this amorphous structure has been dually verified by the X-ray absorption near-edge structure (XANES) where the anisotropy of a-SnO_x structure points towards lower local symmetry. These microstructural arrangements in the a-SnO_x phase cannot be achieved in the crystalline phase. They render it to store more Na^+ with synergistic influence of vertically aligned nano-helices, providing high porosity and surface areas. This uniquely crafted material has delivered an excellent performance as an SIB anode [Figure 1C and D], with a reversible capacity as high as 915 mAh g^{-1} after 50 cycles and a retention capacity of 48.1% at 2 A g^{-1} . These qualities are clearly much better than electrodes made up of crystalline nanoparticles.

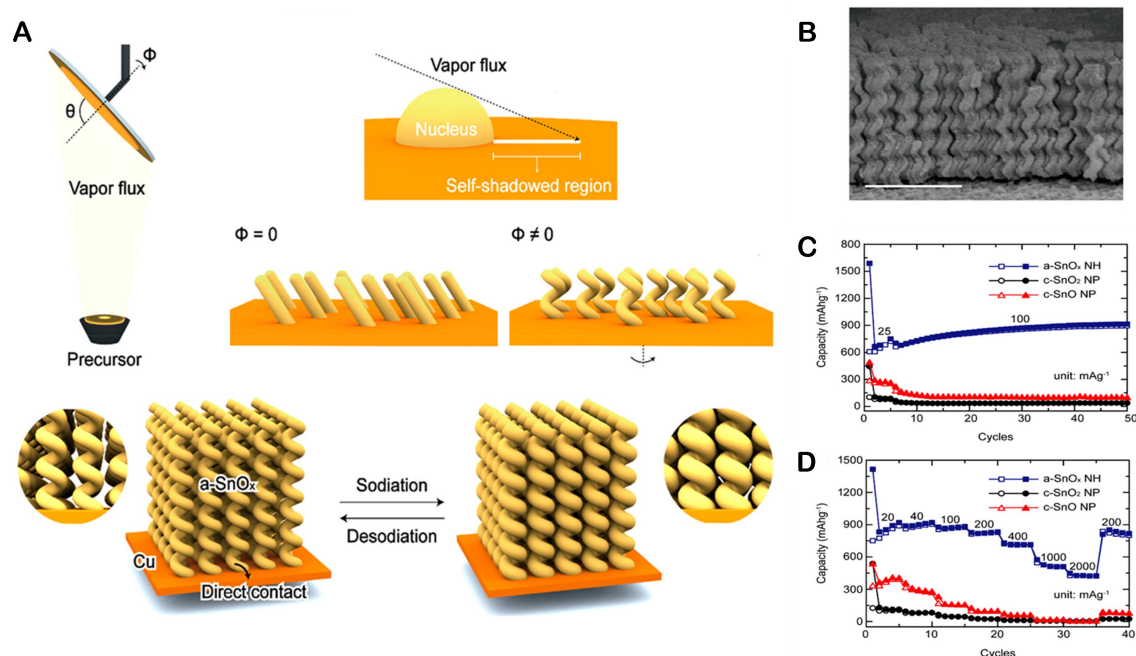


Figure 1. (A) Schematic illustration of the uniquely designed amorphous tin oxide using oblique angle deposition methodology, (B) SEM image, (C) cyclic performance, and (D) rate performance of the synthesized amorphous tin oxide nano-helices. Reproduced with permission from [81]. Copyright © 2019 American Chemical Society.

Han *et al.* have reported an intriguing structure wherein ultrafine SnO_2 nanoparticles are encapsulated into the inner space of holey CNTs by taking advantage of the melt infiltration method [82]. Holey CNTs provided a conductive network and ample void spaces for sodium-ion transportation useful for accommodating volume variations during the charging/discharging process. As an SIB anode, the material delivered a reversible discharge capacity of 184 mAh g^{-1} at a discharge current density of $1,000 \text{ mAh g}^{-1}$ over 200 cycles. Narsimulu *et al.* have used a one-step solvothermal method to prepare a freestanding, flexible, and binderless 3D porous nanocomposite of SnO_2 onto a conductive carbon cloth [83]. The distinctive morphology [Figure 2A] of the 3D composite demonstrated good reversibility and excellent rate performance when employed as an anode for SIBs [Figure 2B]. The 3D hollow fiber structure and spaces between the SnO_2 -NPs can accommodate undesirable volume changes during the charging/discharging process. The structural integrity is maintained due to bonding between SnO_2 and carbon cloth. Moreover, the excellent conductivity and ultra-small nature of SnO_2 nanoparticles enable quick ion electron diffusion passages. The composite displayed a high sodium storage capacity of 498 mAh g^{-1} at a current density of 0.2 A g^{-1} and 205 mAh g^{-1} at 0.2 A g^{-1} over 100 cycles, while a rate capacity was also ensured by the flexible unique morphology [Figure 2C]. Chen *et al.* have optimized and designed an *in-situ* hydrothermally architected nanosized SnO_2 anchored onto MXene sheets that entrust abundant active sites on the conductive MXene substrate, resulting in an outstanding rate capability and superior cyclic stability [84]. The composition could reversibly sustain 414.3 mAh g^{-1} of capacity over 100 cycles at 400 mA g^{-1} .

Tin-based sulfides

Many tin sulfides have been sorted as potential SIB anode materials due to their fascinating features, including high capacity, good electrical conductivity, mechanical endurance, and cost-effectiveness. The unique layered structure of tin sulfides, such as hexagonal SnS_2 and orthorhombic SnS , offers more Na^+

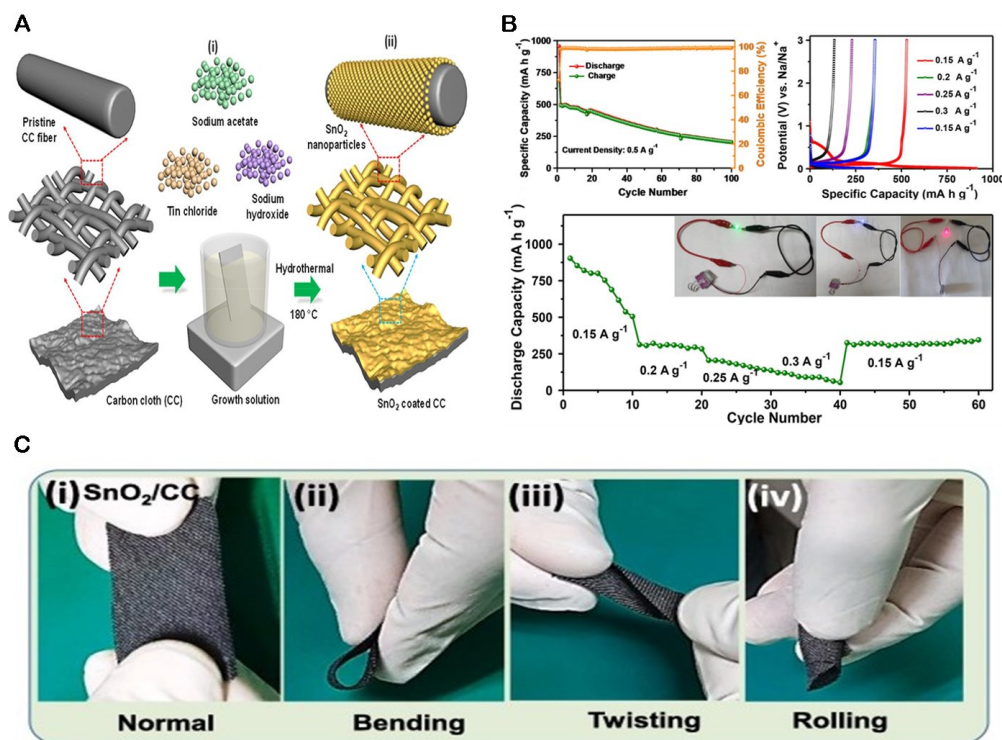
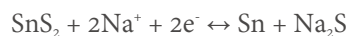
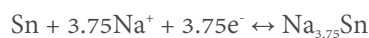


Figure 2. (A) Synthetic representation of solvothermal fabrication of SnO₂-NPs on carbon cloth. (B) Cycling and rate performance for SIBs. (C) Flexibility testing of the material at different angles (i-iv). Reproduced with permission from [83]. Copyright © 2021 Elsevier.

intake by conversion-alloying reactions:



The alloying reaction follows this conversion reaction:



Although the weak M-S bond endorses better reaction reversibility with theoretical capacity values of SnS₂ and SnS being 1,137 and 1,022 mAh g⁻¹, respectively, the large volume alteration during (de)sodiation in Sn-based sulfide anodes makes it difficult to attain high capacity and long-lasting stability. Many dedicated efforts have been made to confront these challenges. Using SnS₂/Co₃S₄ hollow nanocubes anchored on S-doped graphene prepared by the hydrothermal co-precipitation method as an SIB anode has shown a promising capacity [85]. The composite retained a capacity of 1,141.8 mAh g⁻¹ over 50 cycles at 0.1 A g⁻¹. Even at a higher current density of 0.2 A g⁻¹, it sustained a capacity of 845.7 mAh g⁻¹ after 100 cycles. This anode also exhibited an ultrafast charging behavior and delivered a capacity of 392.9 mAh g⁻¹ in less than three minutes at a current density of 10 A g⁻¹.

More economical electrode materials can be derived from various bio-waste utilizations that can positively influence the environment and add structural benefits. In this regard, He *et al.* have prepared an algal waste-derived anode SnS₂/EPC (enteromorpha prolifera derived carbon) that can deliver a high capacity of 443 mAh g⁻¹ at a current of 0.1 A g⁻¹ and a reversible capacity of 340 mAh g⁻¹ over 450 cycles at a high

current rate of 2 A g^{-1} ^[86]. Ding *et al.* have designed a 0D/2D heterostructure of SnS_2 quantum dots (QDs) with N-doped $\text{Ti}_3\text{C}_2\text{T}_x$ MXene^[87]. Controlled nucleation and growth during the hydrothermal process were achieved by using N-methyl pyrrolidone, leading to a uniform growth of SnS_2 QDs of around 3 nm onto the $\text{Ti}_3\text{C}_2\text{T}_x$ MXene matrix. The NH_3 generated during decomposition of the sulfur precursor allowed for *in situ* N-doping of $\text{Ti}_3\text{C}_2\text{T}_x$ MXene, which significantly improved the interfacial Na^+ transport. The composite delivered impressive sodium storage features, including a high specific capacity of 763.2 mAh g^{-1} at 100 mA g^{-1} and an extended cyclic stability (345.3 mAh g^{-1} at 100 mA g^{-1} over 600 cycles).

Controlled interlayer distances in a material can be constructed with another strategy that can ensure the provision of suitable ion transfer pathways. In this regard, a uniquely designed material, SnS_2 /reduced GO (rGO), with extended interlayer spacing has recently been presented by Jiang *et al.*^[88]. They introduced polyethylene glycol (PEG) as an intercalant. The PEG- SnS_2 /rGO composite had a conductive graphene channel that ensured high conductivity and an efficient charge transfer process. C-S covalent bonds also strongly cohered C-S covalent bonds between the graphitic skeleton and SnS_2 , which enabled their structural integrity during (de)sodiation. After 100 cycles at 0.1 A g^{-1} , a capacity of 770 mAh g^{-1} was attained with an equally competing rate performance capacity of 720 mAh g^{-1} at 2 A g^{-1} . A 3D 1T- SnS_2 structure wrapped with graphene (1T- SnS_2 /rGO) has been synthesized onto Ni foam by chemical vapor deposition (CVD) and spray coating^[89]. The unique compositing with 1T phase and rGO coating was chosen as an SIB anode. It showed initial charge and discharge capacities of 748.7 and 768.8 mAh g^{-1} , respectively [coulombic efficiency (CE) = 97.4%], along with a capacity retention of 84.6% after 100 cycles.

Similar to graphene, SnS and SnS_2 from n- and p-type semiconductors have a unique layered structure. The interface between the two materials develops a p-n junction when they are joined to produce a heterostructure, Sn-Sn S_2 . This p-n junction generates an electric field that can facilitate the electron transfer across the material. A monolithic composite SnS-Sn S_2 @GO was constructed by a single-step solvothermal method^[90]. Multilayered SnS-Sn S_2 @GO heterostructured nanosheets exhibited high capacity and stability as an anode for SIBs. After 100 cycles, the capacity sustained by the anode was 450.6 mAh g^{-1} (CE = 69.8%). The capacity sustainability in the composite was commended by the presence of GO, which could alleviate volume expansion effects of the intrinsic SnS-Sn S_2 material to a certain degree and give excellent cyclic stability.

Yang *et al.* have recently proposed a ZnS/ SnS_2 hybrid with N-doped C-fiber encapsulating the ZnS/ SnS_2 -like beads on the thread, as shown in Figure 3A^[91]. The material showed excellent structural and capacity retention, as shown in Figure 3B. In the SIB anode, the material retained a capacity of 174.5 mAh g^{-1} after 1,000 cycles (CE 62%). Its rate performance showed a capacity suspension of $\sim 312 \text{ mAh g}^{-1}$ at 2 A g^{-1} , while a capacity of 601.1 mAh g^{-1} was restored after reducing the current to 0.1 A g^{-1} . Huang *et al.* have presented an optimized SIB anode composed of SnO_2 @ SnS_2 heterostructured QDs (HQDs) evenly embedded on N-doped graphene (SnO_2 @ SnS_2 @NG)^[92]. The uniform patterning of SnO_2 @ SnS_2 on NG was assured by electrostatic interaction between NG and Sn^{4+} . DFT calculations showed effectiveness of hetero-interfaces in electron transport kinetics compared to SnO_2 and SnS_2 alone. The synergistic influence of low ion diffusion pathways and high ion diffusion coefficient benefited from the quantum-sized morphology with the dual benefit of added electrical conductivity by the graphitic network, which resulted in a superb SIB anode capacity of 450 mAh g^{-1} at a current density of 0.05 A g^{-1} and a capacity of 75 mAh g^{-1} at a current density of 5 A g^{-1} .

A heterostructured SnS_2 / Mn_2SnS_4 /C hybrid has been developed using a simple methodology [Figure 4A], showing a high SIB anode capacity^[93]. A prominent capacity (841.2 mAh g^{-1}) with a high ICE of 90.8% was

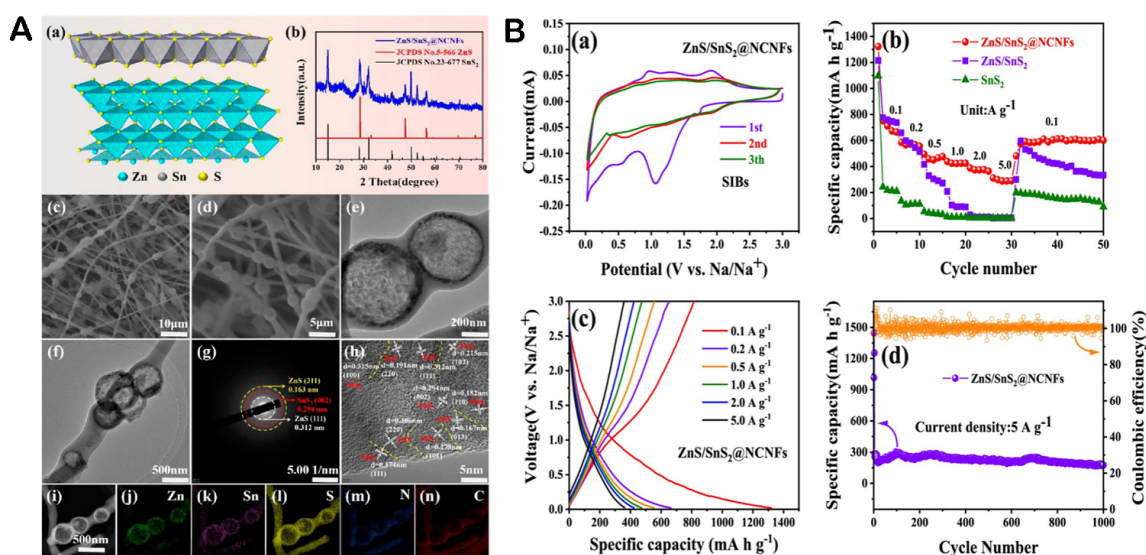


Figure 3. (A) (a) Crystal structure of individual ZnS and SnS₂. (b) XRD pattern of ZnS/SnS₂@NCNFs. (c-n) Electron microscopic details with elemental mapping of ZnS/SnS₂@NCNFs. (B) Electrochemical performance characteristics of ZnS/SnS₂@NCNFs for SIBs. Reproduced with permission from^[91]. Copyright © 2023 American Chemical Society.

achieved. After an extended period of cycling 500 times, the composite presented a capacity of 522.5 mAh g⁻¹ (at 5.0 A g⁻¹) with a value-added rate performance (488.7 at 10 A g⁻¹). The effective heterostructured interfaces with C networks efficiently tuned Na⁺/e⁻ diffusion channels, which boosted the performance of the hybrid. *In-situ* X-ray diffraction (XRD), complemented with cyclic voltammetry (CV) during (de)sodiation, was chosen to track mechanistic details, as shown in Figure 4B. The conversion reaction involved a sequential multistage conversion-alloying (de)sodiation mechanism with an initial lattice expansion [open circuit voltage (OCV)-1.1 V] and final disappearance of SnS₂ and Mn₂SnS₄, along with the corresponding origin of intermediate Sn₂S₃ (1.1-0.6 V, 2θ = 12.5) and final transformation to Sn (2θ = 23.8) and MnSn₂ (2θ = 34.3). Afterward, gradual appearance of Na₁₅Sn₄ (2θ = 21.4) and Na₉Sn₄ (2θ = 37.2) at discharging from 0.6-0.1 V by the alloying of Sn and Na⁺ was detected, representing the full sedation state. Similarly, during desodiation, the formation of Sn (0.1-1.0 V) followed by the origination of Na_xMnS and Na_xSn₂S₃ species (1.0-2.0 V) during conversion was traced at a fully charged state (2.0-3.0 V), depicting the formation of Sn₂S₃ and MnS. The corresponding (de)sodiation process, when traced with *in-situ* transmission electron microscopy (TEM) and selected area electron diffraction (SAED) pattern, confirmed *in-situ* XRD results and additionally provided information regarding volume expansions, which were much less than the reported 420% expansion. Maximum expansions observed in dis(charging) cycles were from 120 nm in the pristine particle to 129.3 nm in the fully sodiated state with 128.2 nm till the 5th desodiation step, as presented in Figure 4C.

Tin-based selenides

SnSe and SnSe₂ are among 2D transition metal chalcogenides with orthorhombic and hexagonal layered structures, respectively. Due to their wide interlayer spacing, tin selenides (SnSe₂) have been considered as promising materials for storing more Na⁺. They can also absorb significant volume changes. Theoretical capacities of SnSe₂ and SnSe are about 756 and 778 mAh g⁻¹, respectively. Although they show electrochemical behavior similar to Sn-based sulfides and oxides, the bond between Sn and Se is relatively weaker which supports faster Na⁺ kinetics. However, these selenides alone have compromised Na⁺ storage in most cases due to their low tolerance of volume expansion/contraction. Thus, Tin selenides have mostly been tested in a composite or hybrid form^[24]. Zhang et al. have prepared a SnSe₂@C nanocomposite, which

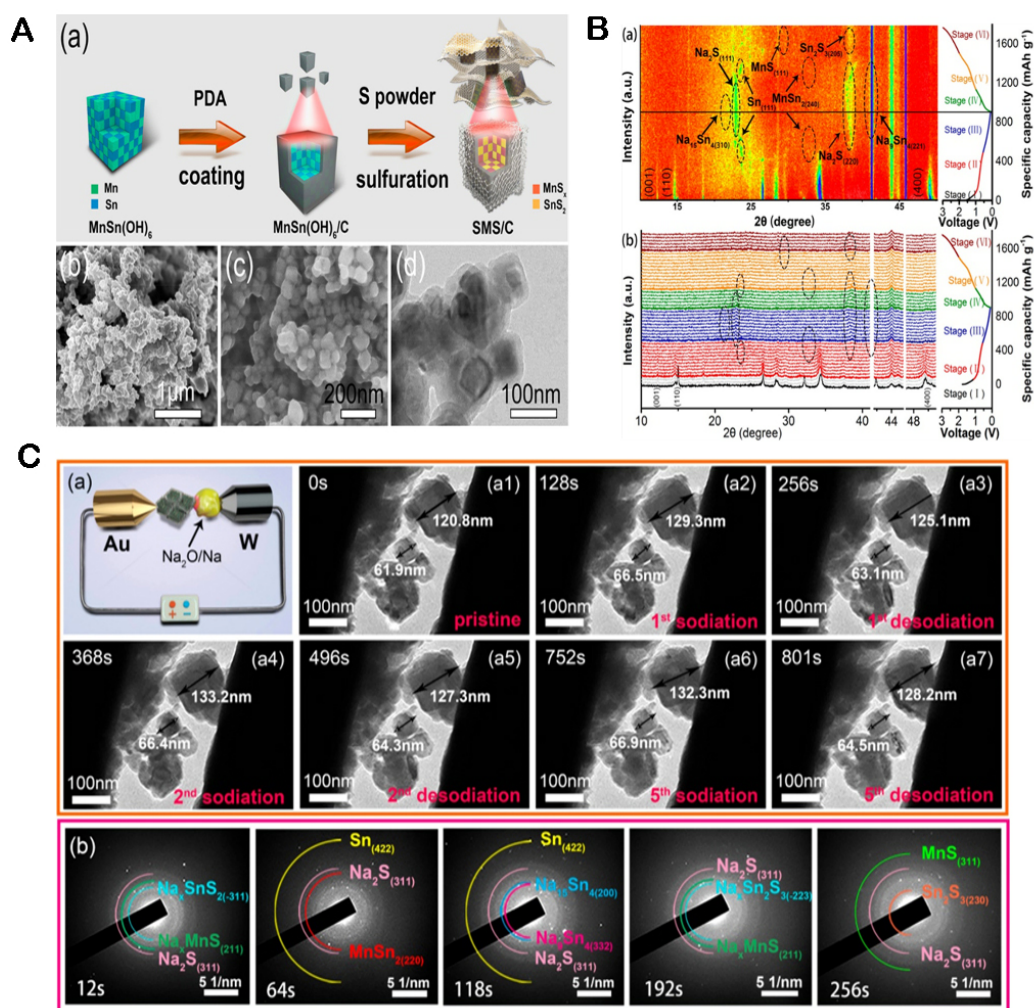


Figure 4. (A) (a) Schematic illustration of SMS/C composite and (b-d) SEM images. (B) (a) Contour plots and (b) *in-situ* XRD stack pattern during cycling. (C) (a) *In-situ* TEM and (b) *in-situ* SAED pattern of fabricated nano-cell during initial cycle. Reproduced with permission from^[93]. Copyright © 2019 American Chemical Society.

shows high sodium storage when evaluated for SIB anode applications^[94]. For the synthesis of this nanocomposite, carbonization of Sn-based metal-organic framework (MOF) and subsequent selenylation were carried out, which resulted in unique C-Sn bonds anchoring SnSe₂ nanoparticles encapsulated in carbon nanoshells. The SnSe₂@C nanocomposite delivered an admired stability and a superior rate capability of 324 mAh g⁻¹ at a current density of 2 A g⁻¹ for SIB.

Recently, the tin selenide (SnSe) nanosheet array on carbon cloth has been explored for a binder and current collector-free anode assembly that could pump high Na⁺, showing an initial capacity of 713 mAh g⁻¹ at 0.1 C, with capacity sustained at 410 mAh g⁻¹ after 50 cycles and 161 mAh g⁻¹ after 250 cycles^[95]. Operando XRD studies revealed that it improved phase reversibility compared to a SnSe bulky particle-derived anode. The capacity fading issue was due to the unviable design architecture of carbon cloth that needed further improvisation. Liu *et al.* have engineered a hierarchical nanobox-designed material using multistep synthesis, as shown in Figure 5A(a-d). The unique structuring strategy comprised a polydopamine (PDA) shell with a heterojunction bimetallic yolk of SnSe₂/ZnSe^[96]. The SnSe₂/ZnSe@PDA nanobox bearing bimetallic heterojunctions created lattice distortions and long-range disorders that not only improved thermodynamic stability of the material, but also affected electronic distributions at heterojunctions that

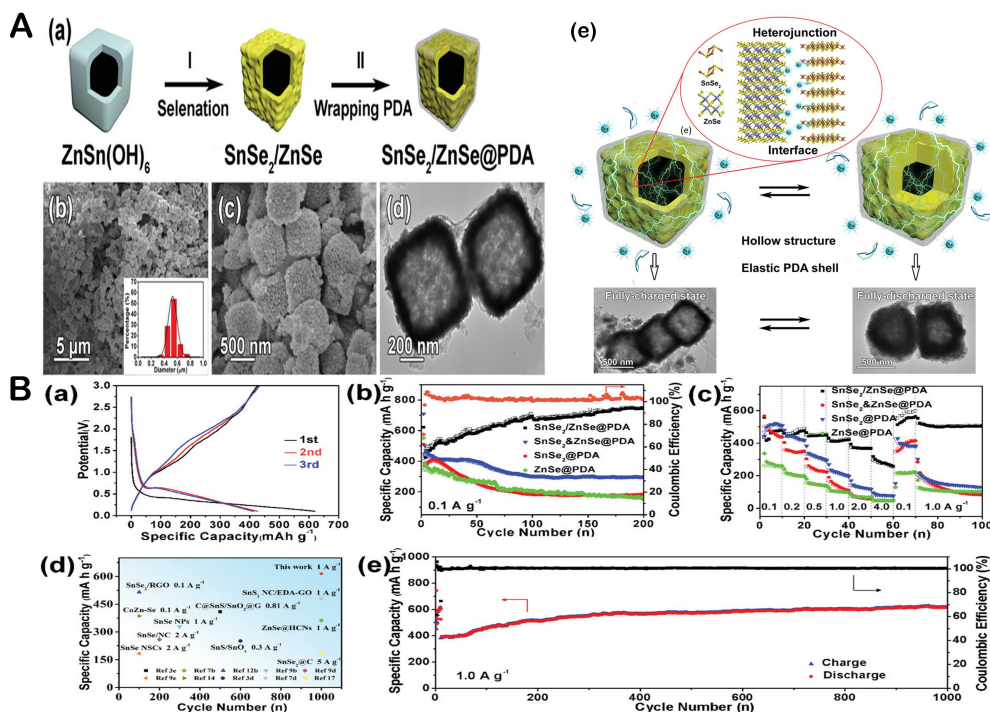


Figure 5. (A) (a) Strategic illustration of the synthesis of SnSe₂/ZnSe@PDA nanobox. (b-d) SEM images with size distribution of nanoboxes. (e) Schematic illustration and TEM showing structural changes in the composite during (dis)charging. (B) Electrochemical Na⁺ storage in SIBs: (a) charge/discharge, (b) cycling performance, (c) rate capability, and (d) Ragone plots of composite SnSe₂/ZnSe@PDA and reported anode materials. (e) Extended cycling of SnSe₂/ZnSe@PDA. Reproduced with permission from^[96]. Copyright © 2021 Elsevier.

could support Na⁺ mobility at heterojunctions. Hollow structures can suppress volume changes and increase the contact area between the electrode and electrolyte. The conductive and elastic PDA shell functioned as a buffer layer to guard against aggregation and disintegration of the SnSe₂/ZnSe yolk during cycling. The heterostructure nanobox SnSe₂/ZnSe@PDA displayed a capacity of mAh g⁻¹ at a current density of 1,000 mA g⁻¹ after 1,000 cycles without much capacity degradation, as shown in Figure 5B. *Ex-situ* XRD and postmortem TEM analysis revealed structural variations during (de)intercalation of Na⁺, whereby the structural resilience successfully mitigated volume changes and alleviated structural aggregation and pulverization.

The combined layering effect of SnSe₂ and Ti₃C₂T_x (MXene) has been explored in layered composite (SnSe₂/Ti₃C₂T_x) by exploiting electrostatic interaction with a reduction and selenylation strategy^[97]. The low conductivity and volume buffering dilemmas were tackled by MXenes that, in return, could get relief from self-stacking of multilayers. The optimized morphology enabled it to sustain a high SIB anode capacity of 245 mAh g⁻¹ at 1 A g⁻¹, which was 5.4 and 4.1 times greater than SnSe₂ and Ti₃C₂T_x, respectively. All these improvements were ensured by robust combination of SnSe₂ and MXene that successfully relieved the volume and capacity fading stresses by furnishing a high mesoporous surface area for effective electrolyte penetration and favored Na⁺ kinetics to achieve less capacity deterioration of just 0.06% per cycle after 445 cycles.

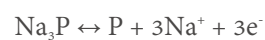
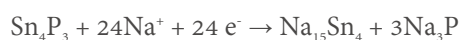
Wang *et al.* have designed a novel composite (MoSe₂/SnSe₂@C) showing promise as an SIB anode^[98]. The composite had a 2D van der Waals heterostructure representing a loose connectivity of the two distinct

layers in the material. At the phase interface, this structure enabled lattice deformation and electron redistribution, accelerating ion migration and charge transfer while the porous carbon increased its electronic conductivity. As a consequence, the MoSe₂/SnSe₂@C composite showed a good cycling performance for SIBs with a reversible capacity of 591.4 mAh g⁻¹ over 110 cycles at 0.1 A g⁻¹ and a capacity of 334 mAh g⁻¹ after 200 cycles at 0.5 A g⁻¹. *Ex-situ* high-resolution TEM (HRTEM) elucidated the sequential conversion of the material upon (de)intercalation with MoSe₂, showing higher reversible transformation than the SnSe₂ phase.

Tin-based phosphides

Sn can also form alloys with P that could reversibly intercalate Na⁺ in the assembly of anode for SIBs. Among various phosphides, the most common one is Sn₄P₃ with a rhombohedral crystal structure that has garnered more interest due to its superior electrical conductance, higher gravimetric capacity (1,132 mAh g⁻¹), higher structural endurance, and ability to operate the derived anode at a lower potential^[99]. Although other tin phosphides such as SnP_{0.94} and SnP₃ are also known, Sn₄P₃ has been explored the most widely as an SIB anode^[100,101]. Pan *et al.* have presented uniformly structured ultrasnall Sn₄P₃ nanoparticles using a low-temperature phosphatization methodology and constructed a 3D framework afterward by implanting these Sn₄P₃ nanoparticle assemblies onto graphene aerogel^[102]. As an anode, it showed an impressive initial performance with an initial discharge capacity of 1,180 mAh g⁻¹ at 0.1 A g⁻¹ that consequently reduced to about 657 mAh g⁻¹ over 100 cycles with a good rate capability (462 and 403 mAh g⁻¹ at current densities of 1 and 2 A g⁻¹, respectively). The same research group also proposed a rational synthetic design of Sn₄P₃ microspheres fully protected by thick hollow C shell [Figure 6A]. The material has impressive sustained capacity as an SIB anode, as depicted in Figure 6B^[103]. In the course of (dis)charging, this hollow protective carbon spherical shell efficiently accommodated volume variations. The enhanced electrochemical performance of Sn₄P₃@C was attributed to its distinctive morphological design. The Sn₄P₃@C composite has demonstrated good sodiation performance as an anode with a capacity of 420 mAh g⁻¹ over 300 cycles at a current density of 0.2 A g⁻¹. Also, after extensive cycling 4,000 times, stable capacities of 205 and 103 mAh g⁻¹ at large current densities of 2 and 5 A g⁻¹, respectively, were attained.

Similarly, the μ-sized Sn₄P₃ delivered an extremely high reversible capacity of 960.3 mAh g⁻¹ at 100 mA g⁻¹ with an ICE of 89.8% after 100 cycles in a diglyme (DGM)-based electrolyte. Also, a capacity retention of 75.1% was recorded after 100 cycles. Such excellent Na storage performance was due to the flexible, compact, and uniform SEI layer in the ether-based electrolyte, which successfully inhibited the separation and aggregation of active components and provided favorable kinetics^[104]. A fascinating biomimetic heterostructured Sn₄P₃ grown on CNT (Sn₄P₃@CNT/C) has been developed by a hydrothermal reaction. This biomimetic bottle brush was designed as a structure in which CNTs served as a “stem” to provide an electron-transferring superhighway and mechanical stability. To enhance the contact area of the CNT surface with the electrolyte along with shortened ion diffusion channels, Sn₄P₃ nanoscale assemblies functioned as a “fructus”. Furthermore, stresses generated during (de)sodiation were recurrently buffered. The Sn₄P₃@CNT/C hybrid anode exhibited an outstanding electrochemical performance with a steadily high capacity of 742 mAh g⁻¹ after 150 cycles at 0.2 C, together with 449 mAh g⁻¹ at 2 C after 500 cycles. The following conversion-alloying reactions occurred:



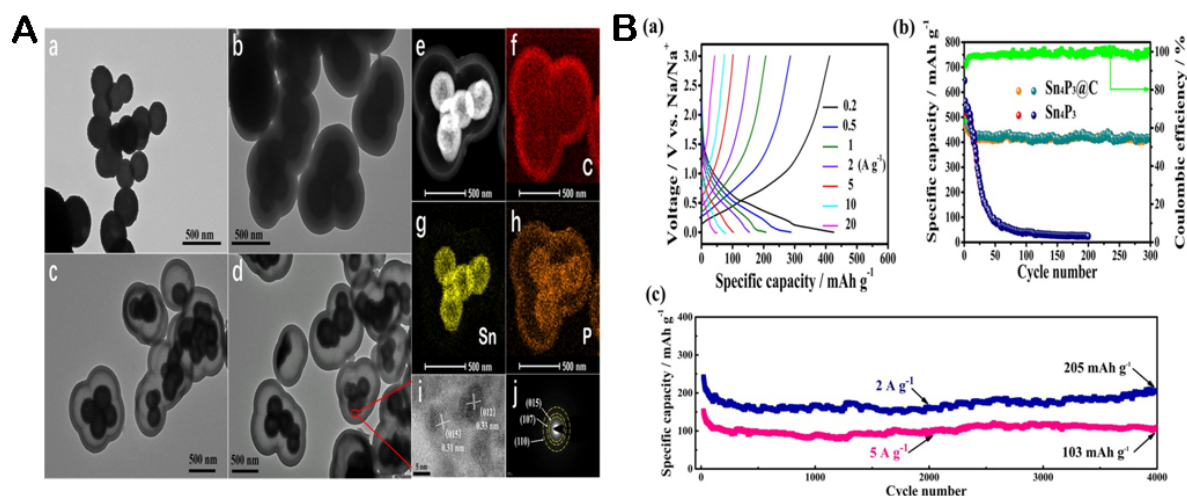


Figure 6. (A) TEM imaging studies showing (a) SnO₂ microspheres, (b) SnO₂/SiO₂ microspheres, (c) hollow microspheres of SnO₂@C, and (d) hollow microspheres of Sn₄P₃@C. (e-h) Elemental mapping images of Sn₄P₃@C, (i) HRTEM image of Sn₄P₃ with (j) SAED pattern of Sn₄P₃@C. (B) (a) Discharge/charge profiles of hollow Sn₄P₃@C electrodes at different current densities, (b) Comparison of cyclic performance of hollow Sn₄P₃@C with pure Sn₄P₃ electrodes at a current density of 0.2 A g⁻¹, and (c) Extended cycling of Sn₄P₃@C hollow microsphere anode at high ampere densities of 2 and 5 A g⁻¹, respectively. Reproduced with permission from [103]. Copyright © 2019 American Chemical Society.

Initially sodiated states formed included the irreversible formation of Na₁₅Sn₄ and Na₃P in the first cathodic scan (at 0.03 V). The anodic scan showed two consistent peaks at 0.55 and 0.68 V that corroborated the desodiation of Na₁₅Sn₄ and Na₃P to form Sn and P, respectively. This evidence was further proved by *ex-situ* XRD and TEM [105]. An interesting multiphase Sn_xP_y/rGO nanohybrid with pronounced Na⁺ storage characteristics has been reported. The multiphase structure with Sn in the form of Sn₄P₃ and SnP_{0.94} was protected by graphene, which, together with the multiphase Sn structure, enabled high volume shuttling along with an excellent structural reversibility as evidenced by *ex-situ* XRD, SEM, and HRTEM studies where both Sn₄P₃ and SnP_{0.94} were detected in disassembled electrodes. The Sn_xP_y/rGO electrode afforded an improved capacitive-dominated Na⁺ storage capacity of 421.8 mAh g⁻¹ over 100 (dis)charge cycles at a current density of 500 mA g⁻¹, resulting in a capacity retention of 84.7%. Additionally, a capacity of about 200 mAh g⁻¹ was conserved over 200 cycles at 2.0 A g⁻¹, which was superior to many other phosphide SIB anodes with unimpressive capacity retention at high current rates [101].

Fan *et al.* have recently fabricated template-assisted growth of Sn₄P₃ hollow nanospheres (HS) dually protected by multifunctional conductive MXene sheeted shells [106]. The highly controlled methodology ensured optimum morphological benefits for Na⁺ transport assisted by MXene encapsulation, as shown in Figure 7A. The role of conductive shell extends to maintaining the homogeneous ionic flux on the MXenes surface, which upon interaction with the electrolyte ensures a highly thin and stable SEI. The SEI composition in the cycled cells was traced using *ex-situ* X-ray photoelectron spectroscopy (XPS). In addition to other electrolyte decomposition products, species contributing to SEI stabilization and structural stability that ensured an ICE of about 84% along with a capacity of 390.5 mAh g⁻¹ at 1 A g⁻¹ after 500 cycles in the full cell taking the Sn₄P₃ HS@MXene anode coupled with the commonly used SIB cathode, NVP, were traced, as demonstrated in Figure 7B.

Fan *et al.* have reported a method of transforming 2D MXene to the highly conductive 3D conductive network by sandwiching Sn and Sn₄P₃ nanoparticles between MXene sheets [107]. Due to covalent interaction with Sn₄P₃ nanoparticles, the uniformly distributed ultra-small Sn nanoparticles (≈ 4 nm) contributed to

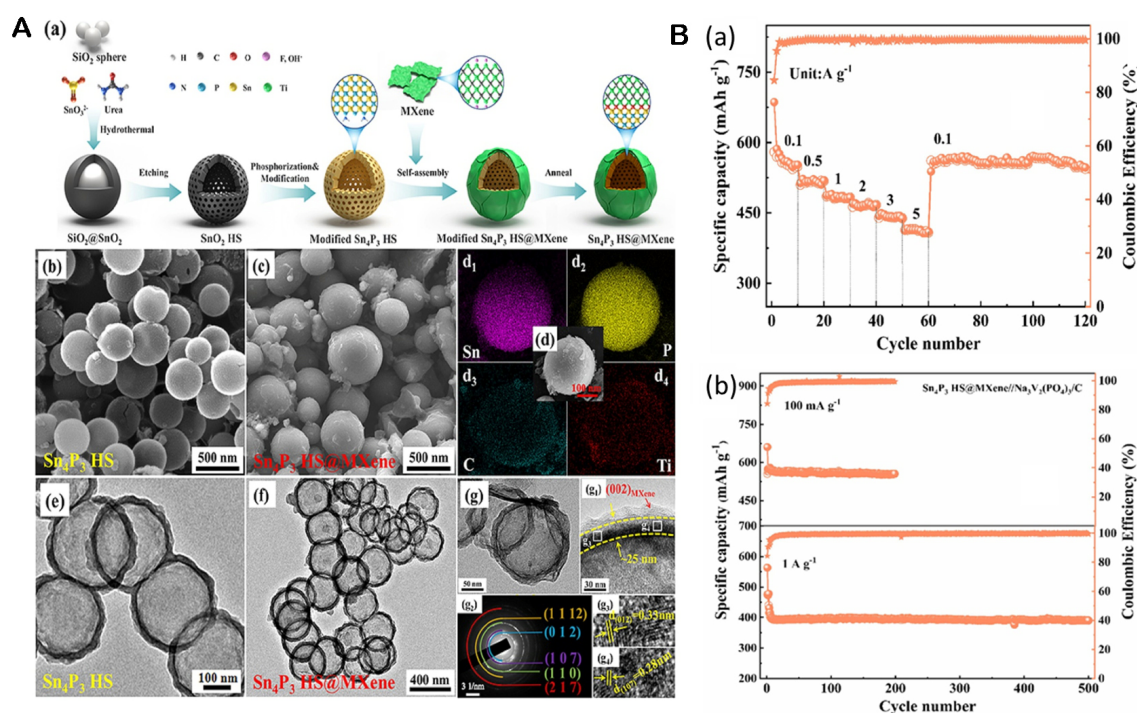
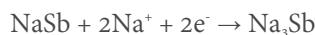
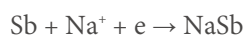


Figure 7. (A) (a) Schematic representation for synthesis of Sn_4P_3 HS@MXene nanocomposite. SEM images of (b) Sn_4P_3 HS and (c) Sn_4P_3 HS@MXene nanohybrids. (d) EDX mapping and elemental analysis of Sn_4P_3 HS@MXene. (e) TEM images of Sn_4P_3 HS, (f) Sn_4P_3 HS@MXene hybrid, and (g) HRTEM images of Sn_4P_3 HS@MXene. (B) Electrochemical performance of the Sn_4P_3 HS@MXene hybrid in full SIB cell. (a) Charge/discharge capacity at various ampere densities, and (b) cyclic stability at 100 mA g^{-1} and 1 A g^{-1} . Reproduced with permission from [106]. Copyright © 2023 Elsevier.

conductive frameworks both horizontally and vertically to MXene planes. Additionally, metallic Sn nanoparticles imparted further to the conductivity of the composite. This hybrid combination of conductive matrices synchronously activated tin phosphide electrochemically, leading to enhanced specific capacity. Volume changes of Sn and tin phosphides were coped by Sn/MXene during discharging/recharging cycles to enable the anode to deliver an ultra-stable cycle life with a capacity of 143.1 mAh g^{-1} over 1,000 cycles at 2 A g^{-1} . A capacity of 127.8 mAh g^{-1} over 1,000 cycles at a current of 5 A g^{-1} was retained under the capacitive-dominated mechanism. Another multiphasic graphene encapsulated Sn_4P_3 and $\text{SnP}_{0.94}$ hybrid showing high aptitude for SIB anodes has been reported to offer long cyclic stability and capacity [99]. Volume buffering offered by the encapsulated graphene shell, together with improved capacity, enabled the fabricated anode to sustain suitable capacity. An ICE of 53.6% was achieved under a pseudocapacitive storage process, whereas a capacity of 203.1 mAh g^{-1} at 1 A g^{-1} over 300 cycles was retained. Finally, electrochemical performances of representative tin-based anode materials explored for SIBs were compared.

Antimony-based anodes for SIBs

Antimony (Sb) has been ranked as one of the most promising SIB anodes with desirous properties, including high conductive character (electrical conductivity about $2.56 \times 10^6 \text{ Sm}^{-1}$), suitable theoretical capacity (660 mAh g^{-1} for Na_3Sb alloy), and low operational potential (about 0.5 V). However, as with other alloying anodes for SIBs, Sb also has many shortcomings that have plagued its utility on a commercial scale. Primarily, complex amorphous structural evolutions having different alloying capabilities with Na^+ and finally reaching full sodiation in the crystalline structure of Na_3Sb are still not well understood yet as intermediate states are difficult to be probed using XRD and other common techniques. CV charge/discharge curves of Sb have revealed a two-step sodiation process.



However, detailed Mossbauer and solid-state nuclear magnetic resonance (NMR)-derived spectroscopic evidence has proposed a multistep alloying with amorphous sodium depleted intermediates not in good agreement with various studies^[30,108]. Huge volume variations (390%) upon full sodiation have also impeded the utility of Sb anodes. Among common routes of modifications, nanostructuring, intermetallic alloy formations, and hybrid composite structural optimizations have been commonly chosen. Thin-walled, heteroatom-doped 1D Sb nanotubes (NTs) reported by Liu *et al.* have shown formidable performance as an SIB anode showing long cyclability with 342 mAh g⁻¹ capacity retaining ability at a current density of 1 A g⁻¹ over 6,000 cycles and a rate performance of 286 mAh g⁻¹ at a current density of 10 A g⁻¹^[109]. Manifestation of a high operational voltage (2.7 V) and a good energy density (252 Wh kg⁻¹) has also been demonstrated in a full cell configuration when coupled with Na₃(VOPO₄)₂F as a cathode.

Several Sb composites have been presented to improve Na⁺ storage performances of SIB anodes with more resilience for volume variations. In this regard, again, the favored choice was the utilization of C-based heterogeneous matrices. Qian *et al.* have previously proposed Sb/C SIB anodes showing a capacity of 575 mAh g⁻¹ over 100 cycles at 0.1 A g⁻¹^[110]. Xu *et al.* have prepared Sb nanoparticles in a N-doped C matrix by pyrolysis. These Sb nanoparticles showed superior cyclic and rate performances than bare Sb anodes and sustained a capacity of about 328 mAh g⁻¹ at 100 mA g⁻¹ (300 cycles)^[111]. The composite anode was also tested at higher current densities, showing an optimum capacity storage of 237 mAh g⁻¹ at a current rate of 5 A g⁻¹. Moreover, in full cell assembly using NVP cathode, a capacity of 139 mAh g⁻¹ was achieved.

It has been reported that 0D Sb nanodots interconnected with 2D C nanosheet composite (Sb-NDs/CN) have an optimum 3D network structure that provides a high surface area, short ion and electronic diffusion paths, and well-dispersed Sb nanodots that could prevent their agglomeration and afford volume buffering^[112]. As an SIB anode, the composite showed competing rate performance (271 mAh g⁻¹ at a current of 2 A g⁻¹) and good cyclic stability of about 380 mAh g⁻¹ at a current density of 0.3 A g⁻¹. A thin filmed, porous self-supported Sb-C framework has been proposed previously. It sustained a capacity of 306 mAh g⁻¹ over 5,000 cycles at 2.34 A g⁻¹ and supplemented with a high rate performance of 200 mAh g⁻¹ at a high current rate of 7 A g⁻¹^[113]. The superb performance was due to thin patterning with well-dispersed Sb nanodots (~3 nm size) ensured by a conductive C matrix for efficient Na⁺ and e⁻ transfer kinetics that ensured amorphous/crystalline phase reversibility.

Recently, we have tested an MOF-derived mesoporous carbon composite of Sb along with SiOC as an SIB anode. It showed stable performance. Upon sodiation, it showed multiple plateaus corresponding to the stepwise Sb transformation to Na₃Sb that mainly contributed to the capacity^[114]. After 200 cycles, a capacity of 403.81 mAh g⁻¹ was traced with 100% CE, while a rate performance of 366.83 mAh g⁻¹ at 5 A g⁻¹ was observed. Cycled electrodes were analyzed by SEM. They showed macro cracks after 200 cycles. SiOC layers effectively buffered volume changes of Sb during sodiation-desodiation cycles. Liu *et al.* have recently validated yolk-void-shell assembled antimony-graphdiyne (Sb@Void@GDY) nanocuboid structures for classical performance of an SIB anode^[115]. They bear definite voids to nullify the volumetric expansion/contraction of Sb during charge/discharge processes [Figure 8]. The unique synthetic strategy illustrated in Figure 8A was validated by XPS and TEM studies [Figure 8B]. Although the ICE was deliberately low (45.6%), the electrode showed more committed performance afterward and offered a capacity of 593 mAh g⁻¹ at 0.1 A g⁻¹ over 100 cycles, maintaining almost 100% of its capacity [Figure 8C]. The rate

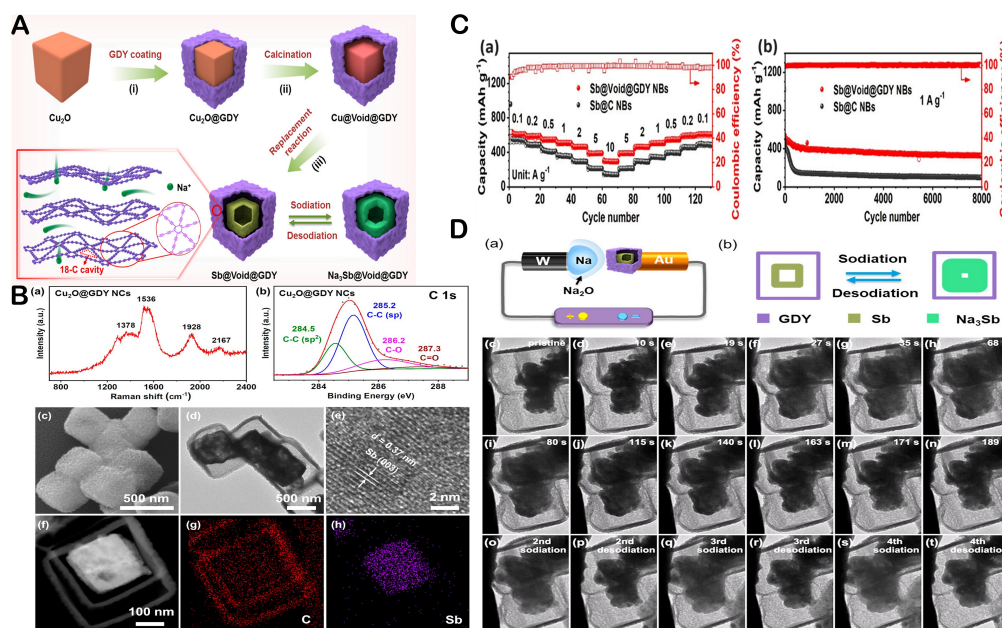


Figure 8. (A) Schematic diagram for the synthesis of Sb@Void@GDY nanoboxes. (B) (a) Raman spectrum and (b) XPS spectrum of Cu₂O@GDY NCs. (c) SEM image, (d) TEM image, (e) High-resolution TEM image, and (f-h) Elemental mapping of yolk-shell Sb@Void@GDY NBs. (C) Rate capability and extended cycling comparison of Sb@Void@GDY and Sb@C NB electrodes. (D) (a) Schematic layout of *in-situ* TEM device. (b) Schematic of structural changes of hollow yolk-shell Sb@Void@GDY NBs during (de)sodiation. (c-t) *In-situ* TEM images from a time-lapse video of the first four (de)sodiation cycles. Reproduced with permission from [115]. Copyright © 2023 American Chemical Society.

performance of the yolk-shell nanocuboid-based electrode was also impressive. At 10 A g⁻¹, a capacity of as high as 294 mAh g⁻¹ was sustained. Importantly, the electrode surpassed many reported anodes in the long cycling marathon where a capacity of 325 mAh g⁻¹ over 8,000 cycles was retained at a current density of 1 A g⁻¹. *In-situ* TEM [Figure 8D] was conducted by making a special nanocell assembly and real-time structural changes were recorded during electrochemical charge-discharge. An expansion of about 324% was noticed in the inner Sb core during sodiation buffered by intermediate voids between the yolk and shell structures. The full cell fabricated using the common cathode NVP and the fabricated yolk-void-shell Sb-Void-GDY anode delivered a capacity of 354 mAh g⁻¹ over 500 cycles at 1 A g⁻¹, furnishing a power of 4 kWh kg⁻¹ and an energy density of 235 Wh kg⁻¹.

Various other modifications such as the use of binders and additives have been made for Sb anodes to optimize their performances. For instance, the role of solution additives during the antimony electrodeposition synthesis has been validated recently by Nieto *et al.* [116]. They utilized surfactants such as SDS (bis(3-sulfopropyl) disulfide) and CTAB (cetyltrimethylammonium bromide) for forming morphologically controlled Sb films. These synthesized materials have been tested as anodes for SIB. The CTAB-assisted Sb anode cell showed better capacity and retention capability, while the SPS-synthesized electrode showed a high capacity of 190 mAh g⁻¹ at 5 C.

Among intermetallics of Sb, alloy heterostructures of Sb with an inactive metal, such as Cu, Ni, Fe, Zn, and so on, are often suitable for SIB anode utility. A Sb/NiSb hybrid has been used as a binder-free SIB anode, exhibiting a superior ICE of 86% along with stable cycling (with a capacity of 521 mAh g⁻¹ at 200 mAh g⁻¹ over 100 cycles), as depicted in Figure 9A [117]. The superior performance of Ni alloying was reflected in the morphological postmortem whereby Sb/NiSb disassembled electrodes (after 100 cycles) presented a stable,

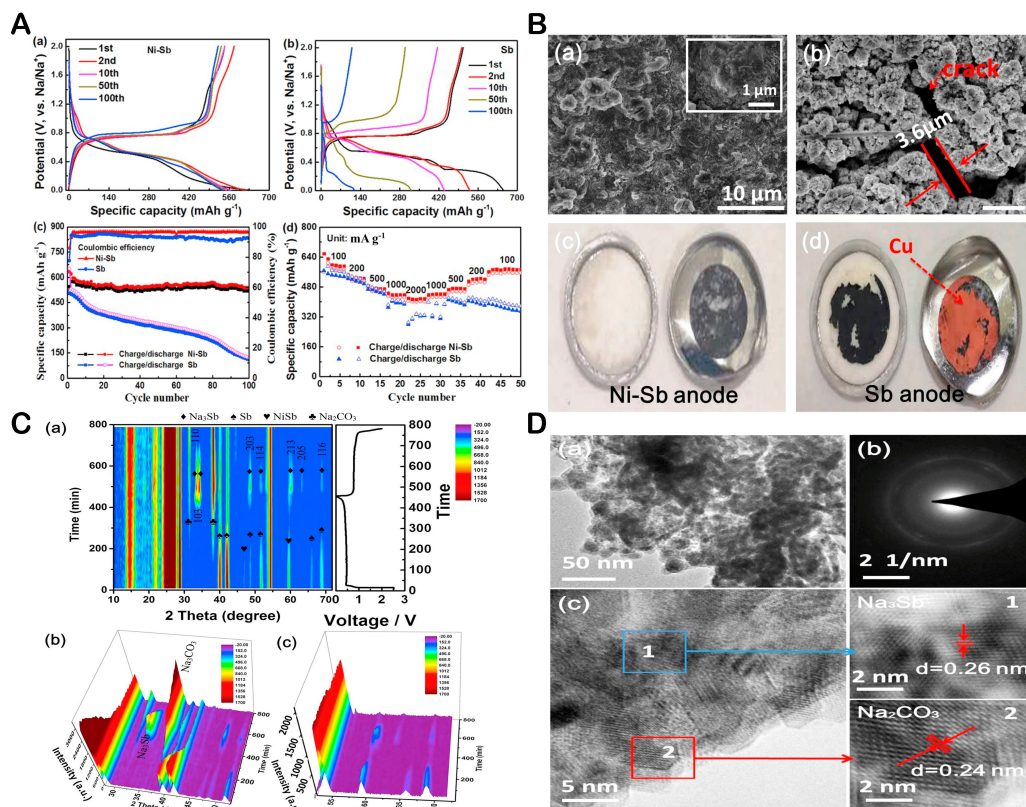


Figure 9. (A) (a and b) Charge/discharge profiles of Sb/NiSb and Sb anodes. (c) Cyclic performances of Sb/NiSb and Sb anodes at 100 mA g⁻¹ for 100 cycles. (d) Rate performances at different ampere densities (0.1–2 A g⁻¹). (B) (a and b) SEM images of Sb/NiSb and Sb-derived anodes after 100 cycles. (c and d) Digital photos of Sb/NiSb and Sb anodes after 100 cycles. (C) (a) Contour mapping (left) of Operando XRD results and corresponding charge/discharge profile (right); (b) Three-dimensional (3D) view graphics between 24° and 54° and (c) 54°–72° of the Sb/NiSb electrode. (D) (a) TEM, (b) SAED, (c) HR-TEM patterns of the fully sodiated Sb/NiSb anode (0.02 V vs. Na/Na⁺). Reproduced with permission from [117]. Copyright © 2020 Elsevier.

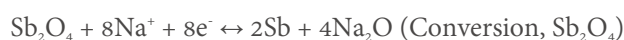
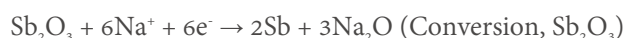
intact structure with SEI surface coverage without cracks in contrast to the Sb anode with prominent cracks and no SEI layer visible on the surface of the cycled electrode material. Digital photographs of the same cycled electrode materials also showed that, unlike the Sb/NiSb electrode material that was intact to the Cu collector without delamination, the Sb anode material got delaminated from the current collector almost completely [Figure 9B]. Detailed *in-situ* XRD [Figure 9C] and *ex-situ* HRTEM [Figure 9D] analysis paved the way for deep understanding of the mechanism of the (de)sodiation. It was concluded that the initial disappearance of Sb and NiSb peaks during initial sodiation resulted in Na₃Sb hexagonal phase formation in multistep sodiation. Additionally, amorphous Ni and Na₂CO₃ were formed (by decomposition to form SEI). During desodiation, the amorphous Sb formation was traced along with amorphous Ni, which contributed to the electrical conductivity.

A Mo₃Sb₇ intermetallic SIB anode with extra high capacity has been presented previously by Baggetto et al. [118]. It retained a rated capacity of 280 mAh g⁻¹ at a very high current rate of 30 C. Recently, SnSb hybrid with CNF/CNT with a good integration strategy has been reported [119]. It showed a high sodium storage capacity of 210 mAh g⁻¹ at 0.5 A g⁻¹ over 700 cycles and sustained a capacity of 161 mAh g⁻¹ at 1 A g⁻¹ over 1,000 cycles. The suitable interconnected 3D CNT/CNF framework could help sustain dispersion of SnSb without aggregation. The framework structure ensured efficient electronic transport and multiple ionic pathways for fast sodium ion transport.

Current potentials of Sb alloys are inhibited by the formation of powdery material that is not compatible with binders, thus hampering ion penetration and electron transport. Recent endeavors to overcome these issues are much more focused. Shen *et al.* have fabricated a self-supported intermetallic Sb-Zn alloy anode via pulse electrodeposition^[120]. When this anode was employed as a binder-free anode for SIB, it achieved an initial capacity of 377 mAh g⁻¹ at 300 mA g⁻¹. After cycling over 320 cycles, it still maintained a capacity of 261 mAh g⁻¹. The rate performance of the electrode was found to be 308 mAh g⁻¹ at 1,600 mA g⁻¹. In comparison, the fabricated anode using constant potential electrodeposition methodology showed much lower performance. Operando XRD studies showed active participation of Zn and Sb to originate NaZn₁₃ and Na₃Sb phases that could transform during the charge/discharge process. The optimum performance of the electrode was ascribed to alloying, structural, and cooperative effects of Zn.

Antimony-based oxides

Oxides of antimony have good alloying potential with Na⁺. In particular, Sb₂O₃ and Sb₂O₄ have high theoretical capacities of 1,103 and 1,120 mAh g⁻¹, respectively. The Sb₂O₃ with a cubic structure subsequently underwent a conversion-alloying process to yield Sb and Na₂O reversibly. However, the low conductivity of Na₂O limited its capacity. Akin to tin oxides, low conductivity, huge volume variations, and pulverization problems also persist in Sb₂O₃ and Sb₂O₄ anodes^[24,121,122]. The conversion-alloying reaction is illustrated as follows:



Octahedral Sb₂O₃ has been prepared by a low-cost and facile alkaline aqueous synthesis method^[123]. As an SIB anode, the material exhibited superior performance (435.6 mAh g⁻¹, 0.1 A g⁻¹ current density, and 50 cycles) to commercial Sb₂O₃ powder. Its electrochemical performance was attributed to the unique structure that provided active surfaces for effective electrolyte wetting and fast kinetics that provided many active sites and improved interactions on interfaces between electrodes and electrolytes. A nickel-supported Sb₂O₃ SIB anode with a good performance (445 mAh g⁻¹) and a CE of 89% over 200 cycles has been previously reported^[124]. The template-assisted synthesized 3D scaffold excellently buffered volume variation in this electrode. Volume deformation during (de)sodiation cycles was also minimized with the designed nano-scaffold structure.

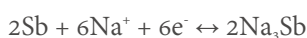
A porous Sb₂O₃@Sb hybrid reported previously by Ma *et al.* showed a low ICE of 67.9%^[125]. However, this hybrid delivered highly regaining capacity in subsequent (de)sodiation cycles with a refined capacity of 658 mAh g⁻¹ over 200 cycles (CE 99.8%) and an outstanding rate performance (200 mAh g⁻¹) at a very high ampere density of 29.7 A g⁻¹. Furthermore, a full cell demonstration (using NVP cathode) showed a competing cyclability with 473 mAh g⁻¹ over 100 cycles (CE 92.7), along with a rate performance of 432 mAh g⁻¹ at 5 A g⁻¹. Operando XRD and *in-situ* Raman excellently traced intermediate phases that provided a mechanistic understanding of capacity retention in the Sb₂O₃ conversion-alloying anode. An electrospun Sb₂O₃@NC freestanding membrane fabricated for SIB anode utilization retained good reversibility in capacity (527.3 mAh g⁻¹ over 100 cycles at 0.1 A g⁻¹)^[126]. The sodium storage behavior involved a capacitive mechanism that demonstrated a high potential. The anode showed a high sustaining capacity of 400 mAh g⁻¹ at 1 A g⁻¹ over extended cycling of 700 times.

$\text{Sb}_2\text{O}_3@\text{Sb}$ has also been reported by Ye *et al.* using etching synthetic protocols^[127]. The ginger-like Sb having decorated nanosized porous Sb_2O_3 on its surface efficiently participated in the volume buffering process. The anode showed a capacitive-dominated mechanism of Na^+ storage with an optimum storage capacity of 526.2 mAh g^{-1} over 150 cycles at 1 A g^{-1} . A uniquely presented Sb_6O_{13} with a thin C coating over it has been recently demonstrated as an SIB anode^[128]. It showed a cyclic stability of 89.64% (delivering 239 mAh g^{-1} at 1 A g^{-1}) over 170 cycles. An alloying-conversion type SIB anode comprising exfoliated GO encapsulating Sb_2O_3 has proven its viability for mitigating volume expansion and other issues that impede the performance^[129]. The proposed anode delivered a capacity of 345 mAh g^{-1} at 25 m A g^{-1} over 100 cycles while a capacity of about 100 mAh g^{-1} at 1 A g^{-1} with good stability in full cell configuration was achieved, corresponding to an energy density of 100 Wh Kg^{-1} . The high surface area and 2D structure of the graphene ensured high electrolyte penetration. A hydrothermally treated nanocomposite $\text{Sb}_2\text{O}_3\text{-CNT-graphene}$ with high surface area exposed offered adequate electrolyte wetting in an SIB assembly, demonstrating a capacitive output of 360 mAh g^{-1} over 100 cycles at 0.1 A g^{-1} with a good rate performance (140 mAh g^{-1} at ampere density of 2 A g^{-1})^[130].

A recent endeavor to improve SIB anode performance of Sb_2O_3 has been proposed with exfoliated graphene Sb_2O_3 in different compositions^[129]. The optimum performing SIB electrode showed interesting features unveiled by *in-situ* impedance spectroscopy whereby varying charge transfer capabilities were detected in the alloying phase, unlike those in the conversion phase. The material showed a respectable potential of 2.95 V in full cell configuration with layered ($\text{Na}_{0.33}\text{Ni}_{0.33}\text{Mn}_{0.66}\text{O}_2$) NNMO cathode. The cell delivered an energy density of around 100 Wh kg^{-1} with 100 mAh g^{-1} capacity at 1 A g^{-1} .

Antimony-based sulfides

The promise of a high theoretical capacity (up to 946 mAh g^{-1}) of antimony sulfide (Sb_2S_3) has been plagued by a very low electronic conduction ($< 1 \times 10^{-5} \text{ Scm}^{-1}$), impractical Na^+ diffusion, and huge volume variations in the (de)sodiation process as an SIB anode material. The sodium diffusion process involves the following reactions:



The conversion/alloying reaction involves an overall transfer of 12 mol of Na^+ . However, a full capacity impact cannot be utilized due to above-mentioned shortcomings. Various nanostructuring, C-matrix addition, and other bimetallic and multimetallic alloys and hybrids have been extensively searched for improved performances of Sb_2S_3 -based materials as SIB anodes^[24].

Deng *et al.* have adopted a “green approach” utilizing natural stibnite ore and sulfur-doped carbon sheets (SCSs)^[131]. $\text{Sb}_2\text{S}_3/\text{SCS}$ composites were developed for SIBs through a quick and effective wet chemical process. The composite $\text{Sb}_2\text{S}_3/\text{SCS}$ delivered an ICE of 68.82% in comparison with an ICE of 61.27% for stibnite. However, a wide difference in the capacity storage was observed after 100 cycles, where capacities of 455.8 and 190.1 mAh g^{-1} were retained by $\text{Sb}_2\text{S}_3/\text{SCS}$ and stibnite, respectively. Xie *et al.* have proposed a novel material approach by compositing carbon-silicon oxide with Sb_2S_3 to attain 1D NFs (denoted as $\text{Sb}_2\text{S}_3/\text{CS}$)^[132]. The superior material's junction resulted in a competitive capacity (321 mAh g^{-1} over 200 cycles at 0.2 A g^{-1}). Homogeneously sized electrospun fibers fully encapsulated Sb_2S_3 with a high void to effectively buffer volume expansions, which entrusted a highly stable performance.

To improve the cycle stability and rate performance of Sb_2S_3 , bimetallic sulfide heterostructure has been developed by adding In_2S_3 and Sb_2S_3 . To further mitigate the low conductivity, CNTs have been incorporated to attain resultant microspheres^[133]. The creation of voids with high surface-active properties led to shorter pathways for rapid Na^+ transfer pathways that entrusted a high reversible capacity of 400 mAh g^{-1} and a long cycle life of around 1,000 cycles with a stable rate capacity (355 mAh g^{-1} at 3.2 A g^{-1}). The performance of the composite alloying anode was traced to operate under a pseudocapacitive dominated process whereby the incorporation of redox inactive in-aided Sb_2S_3 achieved its structural stability during redox. *Ex-situ* HRTEM and Raman mapping of the disassembled cell anode material distinctly revealed metallic Sb, InSb, and Na_3Sb with reversible transformations.

Ternary structured hollow nanorods have been prepared by a solvothermal methodology^[134]. They encompassed Sb_2S_3 at the innermost with intermediate FeS_2 sandwiched by N-doped C from outside. The intact structural design could present an outstanding behavior as an SIB anode. It delivered very promising ICE (82.4%), rate capacity (537.9 mAh g^{-1} at 10 A g^{-1}), and excellent stability (534.8 mAh g^{-1} , CE = 85.7%) after extensive 1,000 cycling at 5 A g^{-1} . Heterogeneous interphases in the superstructure furnished high conductivity and excellent SEI stabilization and accommodated volume variations. *In-situ* XRD traced the reaction mechanism, with peaks of major active species Sb_2S_3 , Sb^0 , and Na_3Sb detected along with other peaks of Na_xFeS_2 and Na_2S . These were also verified by *ex-situ* HRTEM. The origin of Na_2S was related to accelerated reaction kinetics.

To address pulverization and slow kinetics issues, a $\text{Sb}_2\text{S}_3@\text{SnS}@\text{C}$ nanocomposite has been prepared by Lin *et al.*^[135]. The formulated hollow-tube-heterostructured $\text{Sb}_2\text{S}_3@\text{SnS}@\text{C}$ was fabricated by a multistep process. First, Sb_2S_3 NTs were prepared, followed by solvothermal compositing to form $\text{Sb}_2\text{S}_3@\text{SnS}$. Finally, the hybrid was added to C source for coating nanotubular structures. As an SIB anode, the composite sustained a high capacity (442 mAh g^{-1} over 200 cycles at 1 A g^{-1}) and an excellent rate capacity (448 mAh g^{-1} at 5.0 A g^{-1}) that outperformed pure Sb_2S_3 and $\text{SnS}@\text{C}$ composites. It also showed an extended cyclability with a capacity of 200 mAh g^{-1} over 1,300 cycles at 5.0 A g^{-1} . The outstanding cycling stability under the capacitive-dominated mechanism (above 92%) was credited to the synchronous influence of effective heterojunctions with an inner hollow tube-like structure and a protective outer carbon layer, which maintained structural firmness along with mitigation of other issues.

Zhang *et al.* have proposed a blending wet chemical synthetic strategy for Sb_2S_3 with the 2D MXenes for optimum SIB anode configuration^[136]. The MXene surface-supported Sb_2S_3 nanoparticles were able to shutter volumetric stresses along with conductive MXene sheets for steadily fast ion/ electron pathways at favored kinetics. The optimized composite ($50\% \text{ Sb}_2\text{S}_3 @ \text{m-Ti}_3\text{C}_2\text{T}_x$) showed a superior capacity retention (156 mAh g^{-1} at 0.1 A g^{-1} ampere density for 100 cycles) and steady performance with a capability of 72 mAh g^{-1} over 1,000 cycles at 2 A g^{-1} . Very recently, another MXene hybrid with N-C ribbons (bio-derived from *Aspergillus niger*) blended with Sb_2S_3 has been presented as an SIB anode^[137]. The 1D ribbon and Sb_2S_3 with 2D MXene sheet combination resulted in a flexible composite. A schematic illustration with corresponding morphological characterization affirmed successful formation of the hybrid along with superior SIB anode performance [Figure 10A]. The freestanding SIB anode overcame many conventional limitations along with efficient control over polysulfide shuttling. This anode showed a capacity of 394 mAh g^{-1} after 1,000 cycles at 1 A g^{-1} , along with a rate performance of 148 mAh g^{-1} at 10 A g^{-1} . In full cell configuration using the prepared anode and NVP@CNF cathode with a quasi-solid-state electrolyte [poly(vinylidene fluoride-co-hexafluoropropylene) (PVDF-HFP)], the anode showed a superior performance (364.1 mAh g^{-1} at 0.1 A g^{-1} over 100 cycles), an excellent rate performance, delivering a capacity

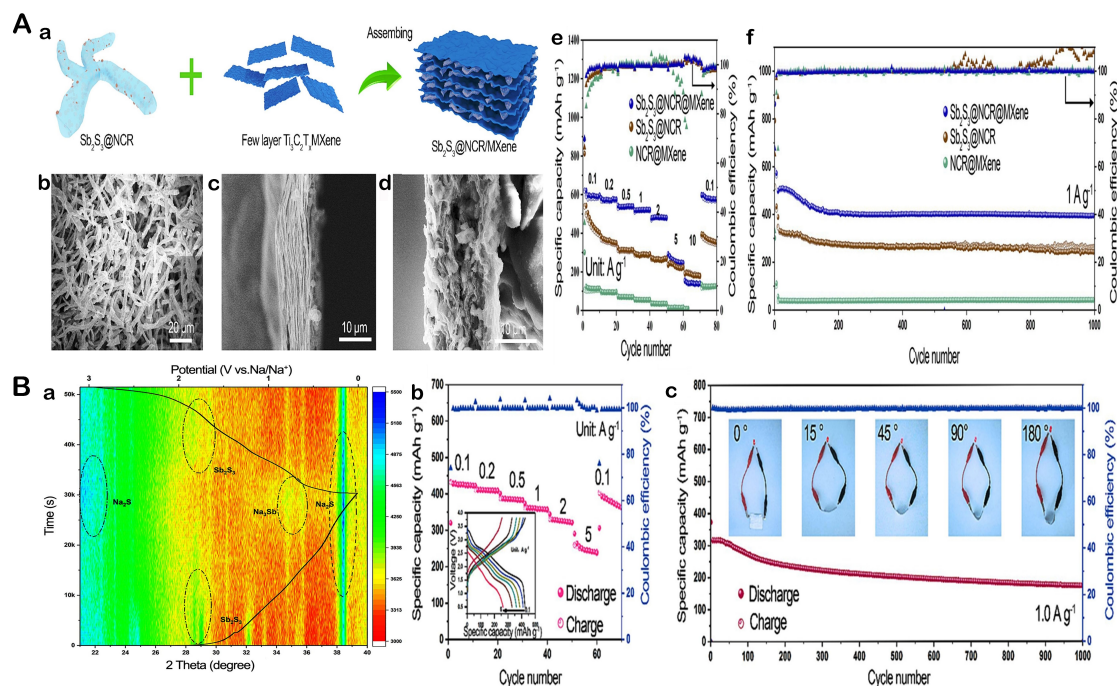


Figure 10. (A) (a) Stepwise schematic illustration of synthesis of N-C Sb_2S_3 @NCR/MXene, (b) SEM image of N-C ribbons (NCR), (c) Cross-section SEM images of $\text{Ti}_3\text{C}_2\text{T}_x$ film, and (d) Cross-section SEM images of Sb_2S_3 @NCR/MXene, (e) Rate performances at various current densities, (f) Extended cycling at 1.0 A g^{-1} . (B) (a) Galvanostatic charge-discharge profiles at 0.1 A g^{-1} and contour maps of in situ XRD pattern for the initial cycle, (b) (Dis)charge profiles with rate behavior at different ampere densities in full cell configuration, (c) Long-term cycling stability at a high current density of 1 A g^{-1} . Inset shows lighting a red LED light when the fabricated full cell battery is bent from 0° to 180°. Reproduced with permission from [137]. Copyright © 2023 Elsevier.

of 263 mAh g^{-1} at 2 A g^{-1} . A highly remarkable extended cycle capacity (173.2 mAh g^{-1} CE 99.6%) was observed after 1,000 cycles. *In-situ* XRD showed the material's evolution with a highly reversible intermediate phase, ensuring stable SIB anode performance [Figure 10B]. Such highly selective material selection with flexible electrode design is highly desired for the commercialization of Sb_2S_3 -derived SIB anodes.

Zhu *et al.* have reported MoS_2 @ Sb_2S_3 heterostructure composites enveloped by rGO [138]. The MoS_2 @ Sb_2S_3 hybrid material with high porosity and a 3D interconnectivity could effectively wet the electrolyte and enhance the kinetics with accelerated ion/electron diffusion at short diffusion pathways. When employed as a negative electrode for SIBs, the composite anode showed fascinating performance (162.1 mAh g^{-1}) after 1,100 cycles. A dual capacitive and diffusion-controlled operated SIB hybrid anode has been fabricated with a simple hydrothermal assisted method by adding Sb salt, rGO, and thioacetamide into a teflon-lined autoclave [102]. The spherical nano-flowered Sb_2S_3 @rGO composite sustained 75.4% (about 544.8 mAh g^{-1} sustained) of its initial capacity (ICE 72.6%) after 200 cycles at 0.1 A g^{-1} . The 3D assembly assured volume buffering and overall improved kinetics with structural endurance to sustain a rate performance of 434.4 mAh g^{-1} at 2 A g^{-1} .

Antimony-based selenides

Sb_2Se_3 , a small band gap semiconductor with natural abundance and benignity, has shown a fascinating theoretical capacity of about 670 mAh g^{-1} as an SIB anode with 12 mol of Na^+ per mol of Sb_2Se_3 [139,140]. Simple

conversion and alloying reactions for Sb_2Se_3 can be written as follows:



The persistence of volume changes and sluggish diffusion kinetics in these Sb-based materials are real bottlenecks to achieving high reversible capacities. Recently, many modifications have been reported. They are dominated by those adapting heterostructuring approaches that often utilize carbonaceous compounds. A 2D Sb_2Se_3 layered anode has been investigated with a focus on mechanistic understandings^[141]. Compared to a bare Sb_2Se_3 electrode with a huge capacity loss, an amorphous carbon composited Sb_2Se_3 anode retained high gravimetric and volumetric capacities of 378 mAh g⁻¹ and 688 mAh cm⁻³, respectively, after 50 cycles. The electrode also offered superior rate performance behavior with gravimetric and volumetric rates of about 270 mAh g⁻¹ and 492 mAh cm⁻³, respectively, at 2C. The capacity drop of the bare Sb_2Se_3 electrode was related to the formation of Na_3Sb accompanied by huge volume expansion, causing large capacity losses after ten cycles. An encapsulated structured Sb_2Se_3 by rGO has been proposed to achieve high reversibility for the de(sodiation) process^[139]. This Sb_2Se_3 /rGO was able to preserve promising capacities (448 and 386 mAh g⁻¹) at high ampere rates (1.0 and 2.0 A g⁻¹, respectively). Besides their long-term stability for 500 cycles, composited nanorods of Sb_2Se_3 in the rGO matrix showed high structural endurance. The detailed reaction mechanism was investigated using *in-situ* XRD, *ex-situ* TEM, and SAED studies. It was verified that the multistage process involved initial intercalation of Sb_2Se_3 with Na^+ , followed by conversion and (de)alloying with good reversibility [Figure 11].

Sluggish sodium diffusion has been one of the limiting factors for the low capacity of Sb_2Se_3 -based SIB anodes. Wang *et al.* have enhanced the capacity by achieving higher Na^+ -diffusion in their N-doped C-coated ZnSe/ Sb_2Se_3 with superior pseudocapacitive dominated Na^+ storage^[142]. The micro-spherical porous ZnSe/ Sb_2Se_3 @NC anode exhibited a higher capacity than corresponding Zn or Sb selenide even with C compositing. Over 120 cycles, the multimetallic ZnSe/ Sb_2Se_3 @NC anode could sustain a capacity of 438 mAh g⁻¹ at 0.2 A g⁻¹ with a rate storage capacity of 316 mAh g⁻¹ at 10 A g⁻¹ of ampere density. Multiple factors, including superior robust hollow morphology offering fast diffusion kinetics ensured by the synergistic influence of ZnSe and Sb_2Se_3 , N-doped C (for volume buffering and conductivity enhancement), and ether-based electrolyte with superior wettability, all coherently enhanced the stability to enable the electrode for an extended cyclic performance over 250 cycles (with a capacity of 295 mAh g⁻¹ at 2 A g⁻¹).

A detailed and conceptual representation of the improved performance of the Sb_2Se_3 @CNT hybrid has been reported recently by Ihsan-ul-Haq *et al.*^[143]. The as-synthesized composite could attain a stable rate capability of 454 mAh g⁻¹ at 12.8 A g⁻¹ with 62% capacity retention over 200 cycles at 10 A g⁻¹. Moreover, a power density of 175 Wh kg⁻¹ (at 0.5 C) and an energy density of 5,784 W kg⁻¹ have been achieved in full-cell configuration. Detailed theoretical (*ab initio*) and experimental investigations were performed along with *ex-situ* cryo-TEM, CV, and XPS. The CV of the prepared electrode showed highly preserved peaks at potentials of 0.78, 1.36, 1.58, and 1.88 V, proving it reversible desodiation and favorable kinetics. In contrast, the CV of commercial Sb_2Se_3 signaled highly thick SEI with more electrolyte degradations. Subsequent cycling CV curves showed erratic behavior, signaling unstable SEI and poor reversibility. The cryo-TEM utilization of frozen (-175 °C) electrodes showed a highly thin SEI of about 35.7 nm with a high uniformity in the synthesized Sb_2Se_3 @CNT electrode. Interestingly, the commercially used anode showed a highly irregular and thicker SEI with a thickness of 71.8 nm, which was about double the thickness of the as-prepared electrode.

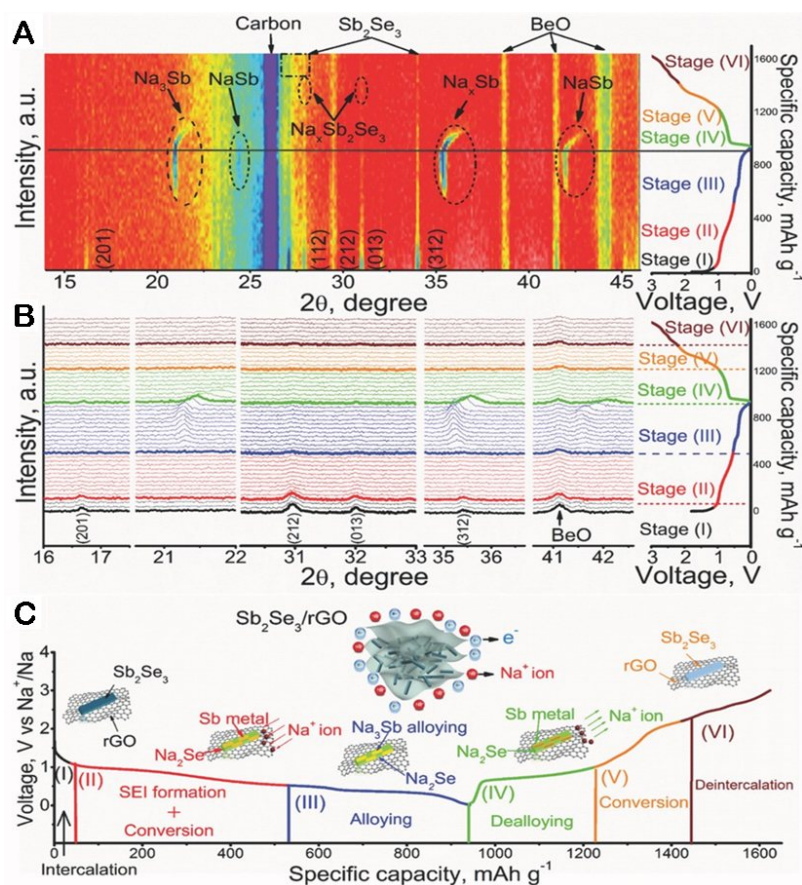


Figure 11. (A) *In-situ* XRD patterns of Sb₂Se₃/rGO SIB anode during first cycle (de)sodiation; (B) XRD patterns within a selected 2θ range during the first cycle against voltage; (C) Stepwise description of the reaction mechanism of the Sb₂Se₃/rGO hybrid during the (dis)charge process. Reproduced with permission from [139]. Copyright © 2017 John Wiley & Sons, Inc.

Hu *et al.* have also reported a composite derived from Sb₂Se₃@rGO with a highly commendable performance as an SIB anode [144]. The composite delivered a stable capacity of 260 mAh g⁻¹ at a high ampere density of 20 A g⁻¹. The rGO alleviated volume stresses with reduced particle agglomeration during repeated (de) sodiation cycles. Similarly, Chong *et al.* have presented an N-doped C-rGO composite of Sb₂Se₃ (Sb₂Se₃@rGO@NC) that bears Sp²-N [145]. This composite can sustain the Sb₂Se₃ volume stresses. The C-N-Sb bond formation has been proposed to be developed *in-situ* after initial discharging. These bonding interactions of Sp²-N have a high affinity for Na⁺, ensuring a high reversible capacity. Besides suitable capacity retention (288.5 mAh g⁻¹ over 100 cycles at 0.02 A g⁻¹), the composite SIB anode has an extended life of over 1,000 cycles with a small capacity drop of 0.18 mAh g⁻¹ per cycle.

A novel combination of Ti₃C₂T_x sheets and Sb₂S₃ nanowires has been recently reported [146]. The composite successfully aggravated most of the shortcomings of individual materials symbiotically. On the other hand, the low conductivity, volume stresses, polyselenide shuttling, and slow sodiation kinetics of Sb₃Se₂ have been bothered by MXenes. As a result, the sheet agglomeration issue of MXenes is delimited by the Sb₂Se₃. The anode can deliver a capacity of 568.9 mAh g⁻¹ at 0.1 A g⁻¹ after 100 cycles. Even after an extended life span of 500 cycles, a superior capacity (304.1 mAh g⁻¹) at a high current of 1 A g⁻¹ was attained.

Recently, Wu *et al.* have successfully recognized asymmetric phase transformational characteristics during (de)sodiation of Sb_2Se_3 nanowires^[147]. The multistep mechanism involved in sodiation includes Na^+ intercalation, conversion, and sequential alloying involving Na_xSb intermediate phases. An incomplete desodiation process has been tracked. It originated from an irreversible capacity fading. The authors were able to trace lateral and surface Na^+ diffusion, whereby a fast Na^+ surface diffusion was found with radial volume expansions. Moreover, the use of *in-situ* HRTEM and corresponding fast Fourier transformation (FFT) patterns reflected the tracing of $\text{Na}_x\text{Sb}_2\text{Se}_3$, Na_2Se , Sb, NaSb , Na_2Sb , and Na_3Sb phases showing conversion/alloying transformations.

Phosphorous-based anodes for SIBs

Phosphorous (P) is deemed to be a potential candidate due to its unique properties such as low potential (0.5 V) and ultrahigh theoretical capacity (2,596 mAh g^{-1}). In addition, it is cheap and benign similar to red Phosphorous (RP). Among various allotropes of P, RP has the most optimistic performance characters. In the amorphous phase, it can store high Na^+ . However, it has a low conductivity (10–14 Scm^{-1}). It also suffers from huge volume changes (490%). The optimum alloying phase in P is Na_3P . Although white and layered black P have also been reported to have alloying potential with Na^+ , unfortunately, white P is toxic and the black P is synthesized under harsh conditions. However, black P has a high conductivity of 300 Scm^{-1} ^[148,149].

A promising composite with nanoporous RP has been constructed by adding the rGO sheeted matrix to yield the composite (NPRP@rGO). Such addition not only enhanced conductive features of the SIB anode, but also ensured high capacity storage parameters (capacity retainability of 1,249.7 mAh g^{-1} at 173.26 mA g^{-1} @ 150 cycles and rate performance of about 656.9 mAh g^{-1} at 3.462 A g^{-1})^[150]. The improved performance was due to more interfacial contacts and effective electrolyte penetrability along with confinement of NPRP nanoparticles on rGO sheets through P-C chemical bonding. Furthermore, electrochemical impedance spectroscopy (EIS) highlighted the peculiar role of a highly conductive rGO network, which guaranteed effective and quick Na^+/e^- transportation.

A durable phosphorus anode for SIBs with an extended cycle life span has been developed through coupling of sulfurized Polyacrylonitrile (SPAN), RP, and C black^[151]. The hybrid has plenty of P-S bonds that could help withstand large volume variations. It offers a high capacity of about 1,300 mAh g^{-1} at a current density of 520 mA g^{-1} , with high CE (> 99%) and good cycling performance (i.e., CE = 91% for 100 cycles).

Capone *et al.* have utilized synergy of particle size of RP, its retainability in the C matrix, and its correlation with the capacity^[152]. Through a two-step milling process using wet and dry ball milling to first reduce the particle size and later composite it with the C (graphite), this methodology has impacted the performance of the anode for SIBs application to achieve 1,354 mAh g^{-1} as initial charging capacity along with an overall CE of 88% over 100 cycles. Xiao *et al.* have established a correlation between stability of the RP composite electrode in ambient conditions and its performance^[153]. The composited electrode (derived from RP and C black) showed a good initial performance (1,070 mAh g^{-1} of capacity retention over 200 cycles at 400 mAh g^{-1}). When exposed to air, the electrode showed a decrement in capacity retainability, while synchrotron-based XAS showed a concurrent appearance of phosphate species that passivated capacitive reactions.

To optimize the SIB anode performance in the C compositing of RP, various modest synthetic modifications have been adapted. For instance, Liu *et al.* have reported a controlled synthesis of RP-rGO composite using ethylenediamine additive to get ultra-small and well-dispersed RP particles on the surface of rGO^[154]. The composite showed highly admiring performance with a storage capacity of 2,057 mAh g^{-1} at

100 mA g⁻¹ while sustaining 65.6% of the capacity over 5,000 cycles at an ampere density of 2 A g⁻¹. During (dis)charging, the strong interaction between rGO and NRP/Na₃P inhibited volume variations.

To better protect the RP-C composites from air exposure and the resultant capacity engulfing process, a protective coating of polypyrrole (PPy) has been proposed, which could enhance the conductivity and impart electrolyte and air stabilization^[155]. This strategy resulted in stable electrode material at ambient conditions having a high RP content with a stable reversible capacity of 800 mAh g⁻¹ at a current density of 50 mA g⁻¹. Jin *et al.* have adopted an assisted double annealing strategy to ensure highly porous conductive networks interconnected inside the P host^[156]. The extra-short Na⁺/e⁻ diffusion pathways in the conductive matrix supported the structure from volume variations and exhibited an astonishing longevity over 2,000 cycles with 1,027 mAh g⁻¹ of steady capacity at 4 A g⁻¹ and an equally competitive rate behavior.

An SIB anode with a distinguished performance and real-time performance-mechanistic evaluation has been reported by Liu *et al.*^[157]. *In-situ* TEM and simulations detected “liquid-like” properties, metallic character, and structural endurance in the RP CNF composite. The highly encapsulated RP inside the C matrix, akin to a core-shell structure, mitigated side reactions. This observation of liquidity of RP on sodiation was dually verified using time-lapse scanning TEM (STEM) images. The optimized capacity of 1,019 mAh g⁻¹ over 5,000 cycles at 1 A g⁻¹ was a benchmark. Details are shown in Figure 12.

MXene-supported uniform-sized RP nanoparticles were additionally integrated with multi-walled CNTs (MWCNTs), leading to outstanding stability and improved mobility of Na⁺/e⁻ transportation^[158]. The hybrid showed a capacity of 371.6 mAh g⁻¹ at 0.2 A g⁻¹ over 100 cycles. A facile methodology for high-capacity SIB anodes with high mass loadings has been reported by Zhu *et al.*^[159]. A composite of wood-derived carbon and CNTs was coupled to RP. Multi-channeled ion and electronic pathways with a compact but porous framework synchronously improved the capacity retention ability at high mass loadings. Although optimal redox kinetics at a lower mass loading (8.2 mg cm⁻²) was achieved even at a high mass loading of ~14 mg cm⁻², capacity preservation of 53.9% was attained. A superior gravimetric capability of 468.8 mAh g⁻¹ and real rate capacity of 1.63 mAh g⁻¹ at 106.6 mAcm⁻² were captured. A liquid exfoliation strategy for amorphous RP nanoplates synthesis and their composite with CNTs has been proposed recently by Kaur *et al.*^[160]. A superior air stability was achieved with low oxidative degradation that enabled the composite to attain higher capacities above 2,000 mAh g⁻¹ over 1,000 cycles. Other composite hybrids and phosphorous alloys have been extensively explored as SIB alloying anodes with many recent detailed reviews^[161-164]. Zhang *et al.* have reported a composite SIB anode (Sb/P@C) that could deliver a capacity of 350 mAh g⁻¹ at 500 mA g⁻¹. At 50 mA g⁻¹, a capacity of above 400 mAh g⁻¹ was sustained over 100 cycles^[165].

Germanium-based anodes for SIBs

Germanium (Ge) has been highlighted for its strong alloying potential with Na⁺ and less volume expansion than Sn and Sb conversion-alloying anodes. However, its theoretical capacity (369 mAh g⁻¹) is limited for SIBs because 1 mol of Na⁺ in the resulting NaGe formulation showed unfavored kinetics in the crystalline Ge, which rendered it below the limelight of energy storage community. Although it has 1,000 times superior electrical conduction than Si, the crystalline Ge has a very minor affinity for Na⁺ that can only provide a capacity of 20 mAh g⁻¹. Thus, many derivatives, especially those with amorphous Ge, have been proposed both theoretically and experimentally, whereby a theoretical capacity of 576 mAh g⁻¹ (corresponding to Na_{1.56}Ge) has been achieved in the amorphous phase^[45,166,167]. Lu *et al.* have presented detailed *in-situ* TEM-supported evidence of (de)sodiation changes in amorphous Ge nanowires^[45]. The unique appearance of pores in the desodiated state and their reappearance upon sodiation in the Ge nanowires were due to sodiation-induced defects during *in-situ* HRTEM. The large volume expansion of

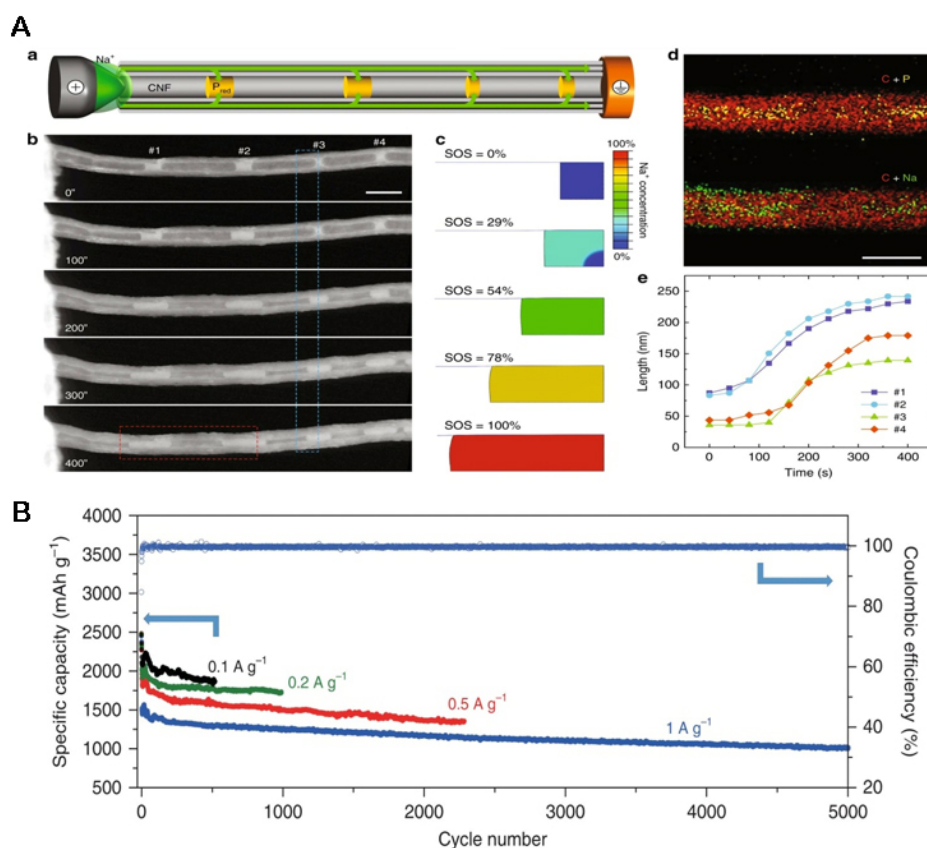


Figure 12. (A) (a) A schematic illustration of *in-situ* TEM setup. (b) STEM image series captured in real-time showing P_{red} volume expansion during sodiation (scale bar: 200 nm). (c) Simulated SOS according to the P_{red} morphological evolution of the region labeled with a blue rectangle in image (b). (d) EDS maps of phosphorus (green), sodium (yellow), and carbon (red) elements of the region labeled with a red rectangle in image (b) (scale bar: 200 nm). (e) Length changes of four P_{red} segments marked in image (b) as a function of time during the sodiation process. (B) Extended cycling of the P_{red}@CNF anodes with variable current densities. Reproduced with permission from [157]. Copyright © 2020 Springer Nature Limited.

300% corresponded to a higher sodiated state than NaGe and closely resembled Na_{1.56}Ge. These findings highlight the structural robustness with higher potential of Ge as an SIB anode.

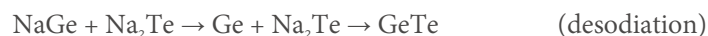
A very cheap and benign combination of amorphous Ge loaded onto the graphite network has achieved an augmented performance (526 mAh g⁻¹ over 120 cycles along with 160 mAh g⁻¹ at 10 C of ampere density) that highlights possibilities for more superior capacity Ge-based SIB anodes particularly having 2D and 3D structures [167]. A highly functionalized C source derived from dopamine has been added to mitigate the conductivity and sluggish kinetics and stabilize the Zn₂GeO₄-derived SIB anode [168]. In comparison with the isolated Zn₂GeO₄ (capacity = 113 mAh g⁻¹ at 0.1 A g⁻¹ over 50 cycles), the C-coated Zn₂GeO₄ micro-rods delivered a suitable capacity of 317 mAh g⁻¹ (CE 88%) at 0.1 A g⁻¹ over 50 cycles with a rate capability of 150 mAh g⁻¹ at 2 A g⁻¹. The dopamine-derived amorphous carbon offered a large electrode-electrolyte interface to facilitate ion/electron transportation at shorter distances apart from volume buffering.

A highly reversible capacity-delivering SIB anode synthesized by a template-free solvothermal approach with controlled nanosized (10 nm) germanium phosphide (GeP_x) organized into micro-spherical architecture has been presented by Tseng *et al.* [169]. The superior patterning without an additional C matrix could cope with volume stresses and lead to an excellent performance, which is a testament to the advantage of the structural design approach. A high ICE of 65.28% along with a capacity of 704 mAh g⁻¹ was acquired

at 0.2 C after 100 cycles. An excellent mechanistic approach for capacity origination and fading has been adopted by Shen *et al.* The material demonstrated promising capacity retention and stability, as shown in Figure 13A. The capacity fading issue was traced using *in-situ* HRTEM with allied techniques to detect species causing capacity degradation during (de)sodiation cycles, as shown in Figure 13B and C^[170]. An ICE of 88.61% and a capacity of 330 mAh g⁻¹ over 100 cycles were offered by the electrode in half cell. Expansion during sodiation was captured by TEM in a time-lapse experimental setup, which showed GeP nanoflake expansion from 0.93 to 1.25 µm without any cracking in the nanoflake. The SAED pattern also recorded anisotropic expansions along different planes, leading to intermediate orthorhombic NaGe₃P₃ that ultimately resulted in amorphous phase NaGe and Na₃P. The *in-situ* TEM also revealed that after completing the first cycle of sodiation, the amorphous phase could not revert back to the crystalline GeP upon desodiation.

Li *et al.* have trailed the path of sodiation in the GeP@C anode for SIBs^[171]. The self-healing anode has the capability of structural reformation under a multistep sodiation process involving intercalation followed by the conversion and, finally, the alloying step. This self-healing property was attained due to a low formation energy (-0.19 eV) of the layered material, which further stabilized the graphitic incorporation, creating P-C bonds that synchronously sustained more Na⁺ at improved kinetics and conduction. The GeP anode has the potential to achieve a high ICE (93%) and a high sodiation rate capacity (360 mAh g⁻¹ at 2 A g⁻¹). Although inspiring, such performance was lower than that of the GeP@C that sustained a high ICE (above 90%), a long cycling life with a capacity of 850 mAh g⁻¹ at 0.1 A g⁻¹ over 300 cycles and a sodiation rate capacity of 533 mAh g⁻¹ at 2 A g⁻¹. The high metallic conductivity of the intermediate Na_xGeP with metallic conductive behavior and interlayer bonding compatibility of graphite and GeP created stronger P-C interactions that alleviated capacity performance and stability.

Besides GeP, GeTe has also been demonstrated by many researchers for SIBs anode capabilities. A GeTe/C composite proposed by Sung *et al.* can yield good gravimetric capacity (98.5% after 100 cycles) and rate performances (704 mAh g⁻¹ at 1 C and 630 mAh g⁻¹ at 3 C)^[172]. The conversion/alloying mechanism in the composite anode of GeTe/C material has been investigated using *ex-situ* XRD and extended X-ray absorption fine structure (EXAFS) during different (dis)charging states. In the first sodiation state, amorphization led to metallic Ge, followed by Na-Ge bond formation. In contrast, the desodiated state showed reappearance of the Ge-Ge bond proceeded by the reappearance of GeTe, which was evident as presented by the following reactions:



A mechanism-directed approach has revealed the significance of amorphous structures in nullifying the influence of stress-induced limitations and interfacial inhomogeneities that plague the SIB anode capacity^[173]. For this purpose, 2D porous GeS₂ nanosheets with amorphous structures have been constructed. They demonstrated highly stable capacity and rate performance, as shown in Figure 14A(a-d). The electrode maintained a highly uniform electrode/electrolyte interface, ensuring fast and isotropic Na⁺ diffusion channels to assist in the complete conversion reaction for optimum capacity without particle aggregation [Figure 14B(a-c)]. The amorphous GeS₂ also tolerated a capacity of 512.8 mAh g⁻¹ at 10 A g⁻¹ after an extended 1,000 cycling period. The mechanism of stress forbearance was illustrated based on Raman and TEM results [Figure 14B(d-h)], whereby the sheet-like morphology managed stresses incurred during cycling.

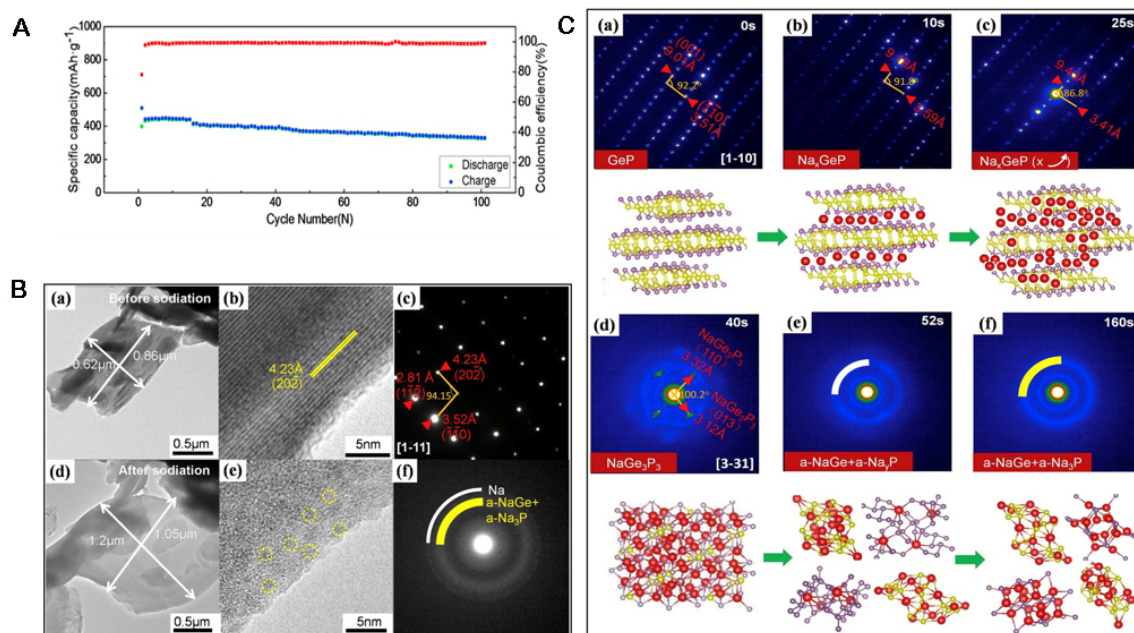


Figure 13. (A) Cycling behavior of GeP anode. (B) Morphology and structural changes in GeP: (a-c) before sodiation and (d-f) after sodiation via TEM, HR-TEM, and SAED. (C) Structural evolution of the GeP nanoflake during sodiation recorded by SAED patterns. (a) GeP crystal before sodiation, (b and c) Na⁺ intercalation into the GeP lattice with the gradual increase in d-spacing (001), (d) Formation of NaGe₃P₃ intermediate phase, and (e and f) Amorphous Na-Ge and Na-P alloys. Reproduced with permission from [170]. Copyright © 2019 Elsevier.

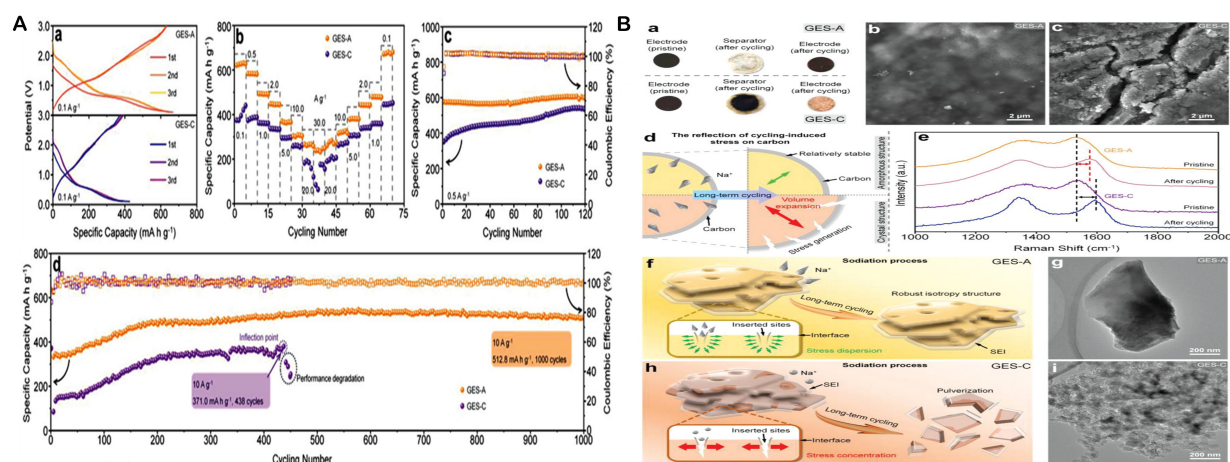


Figure 14. (A) (a) The (dis)charging curves at 0.1 A g⁻¹, (b) Rate performance at various ampere densities, (c) Cycling behavior at 0.5 A g⁻¹, and (d) High-rate cycling at 10 A g⁻¹ for GES-A and GES-C samples. (B) (a) Digital photos of electrodes and separators before cycling and after completing 100 cycles. (b and c) Corresponding SEM images after 100 cycles for GES-A and GES-C samples. (d) Mechanistic layout of inner stress. (e) Raman spectra before and after cycling for GES-A and GES-C. (f-i) TEM supported illustration of enhanced structural stability after 100 cycles for (f and g) GES-A and (h and i) GES-C. Reproduced with permission from [173]. Copyright © 2022 John Wiley & Sons, Inc.

A Ge-based C NF with N, S doping has been fabricated by centrifugal spinning and subsequent thermal treatment methodology to yield N, S-Ge@PCNF [174]. N, S doping, in addition to the porous CF, improved electronic conduction and ionic mobility in a way to sustain a capacity of 443 mAh g⁻¹ over 200 cycles as an SIB anode. The composite also delivered a rate capacity of 300 mAh g⁻¹ at 1 A g⁻¹ in contrast to a capacity of 236 mAh g⁻¹ delivered by the composite with no N or S functionalities (Ge@PCNF). Detailed characterization of the N, S-Ge@PCNFs composite showed uniformly dispersed Ge nano-assemblies on tubular PCNFs. Overall, N, S-doping imparted conductivity enhancement that, together with

interconnected PCNFs framework, facilitated Na^+ transfer kinetics and buffered volume changes to maximize Na storage.

Silicon-based anodes for SIBs

Silicon (Si), a cheap, abundant, and environmentally friendly material, is an ideal choice for alloying SIBs whereby a single mol of Na^+ in the NaSi can result in a theoretical capacity of 960 mAh g^{-1} . However, a very low practically obtained capacity (less than 40 mAh g^{-1}) has been shown by the crystalline Si. Hence, Si was declared electrochemically inactive previously (with $+0.6 \text{ eV}$ binding energy of Na)^[175]. However, many theoretical studies have verified the potential of Si for SIB anodes, although this needs to be experimentally verified^[176,177]. Compared to crystalline Si with limited Si uptake, the performance of amorphous Si as an SIB anode is practically more optimistic. The conversion of crystalline Si to amorphous Si after initial cycles also reincarnates the capacity of Si anodes. Various other prepositions for improved anode characters in Si have been proposed, such as C coating^[178], porous structuring^[179], and other composite modifications^[180].

Regarding composite modifications, Kempf *et al.* have studied the temperature-dependent performance of ion carbon-rich Sn-SiOC composites for SIB anodes^[181]. The best performance was shown by the composite (SnO_2) pyrolyzed at 900 C , which could deliver a steady capacity of 234 mAh g^{-1} at 37.2 mA g^{-1} . At a current density of $2,380 \text{ mAh g}^{-1}$, it could sustain a capacity of 131 mAh g^{-1} . Their findings have opened a door for temperature-dependent material synthesis as temperature-performance correlations have been widely addressed to control the morphology and thereby the corresponding capacity, although the alloying mechanism in Si is unclear and somewhat controversial. Very recently, an electrochemical derivatized varyingly ordered Si has been proposed by Li *et al.*^[175]. The combination of short, medium, and long-range ordering induced strong Na-Si interactions well matched for fast ion/-transfer phenomena. The anode in bare form delivered a capacity of 352.7 mAh g^{-1} at 50 mA g^{-1} (95.2% CE), while its C composite Si/C supplied a capacity of 449.5 mAh g^{-1} [Figure 15]. Interestingly, they proved an adsorption-interaction mechanism instead of the commonly evidenced alloying mechanism.

Amorphous Si comprising nanocubes or boxes with hollow structures has been composited with rGO to exploit the SIB anode potential of this novel architecture material^[182]. The composite imparted stable performance over 2,000 cycles with rate capacities of 261.2 and 73.3 mAh g^{-1} at 0.1 A and 3 A g^{-1} , respectively. An ordered mesoporous C with Si/SiO₂ hybrid constituting 2D mesochannels was found to be highly effective in enhancing Na^+ and e^- transfer kinetics, suppressing volume variation effects, and providing highly conductive Na^+ diffusion pathways. It showed a daring storage capacity of 423 mAh g^{-1} at 0.02 A g^{-1} after 100 cycles with an extended longevity (capacity of 190 mAh g^{-1} at 1 A g^{-1} after 500 cycles)^[183]. The mechanistic-driven phase conversions have been presented in C-composited SiP_2 SIB anodes using *in-situ/ex-situ* XRD and TEM^[184]. The proposed anode showed an ICE of 76% with a 100-cycle capability of 410 mAh g^{-1} together with a rate performance of 198 mAh g^{-1} at 1 A g^{-1} . *In-situ* XRD and *ex-situ* XRD with 2D contour plots have outlined their real-time performance and conversion behavior. Sodiation resulted in diminished peak intensities of SiP_2 resulting from amorphization, while partial recovery of the SiP_2 peak (along with features of P and S peaks) was observed in charging. During discharge, new peaks related to Na_3P and NaSi_6 appeared, with some peaks from some unreacted SiP_2 . Furthermore, these observations were counter-verified by fabricating a nano-battery for *in-situ* TEM and SAED patterns. In the charging process, the clear amorphous behavior with dual crystalline/amorphous SiP_2 phase was well confronted in the initial cycle, with complete amorphization in the third cycle as observed in the *in-situ* TEM/SAED.



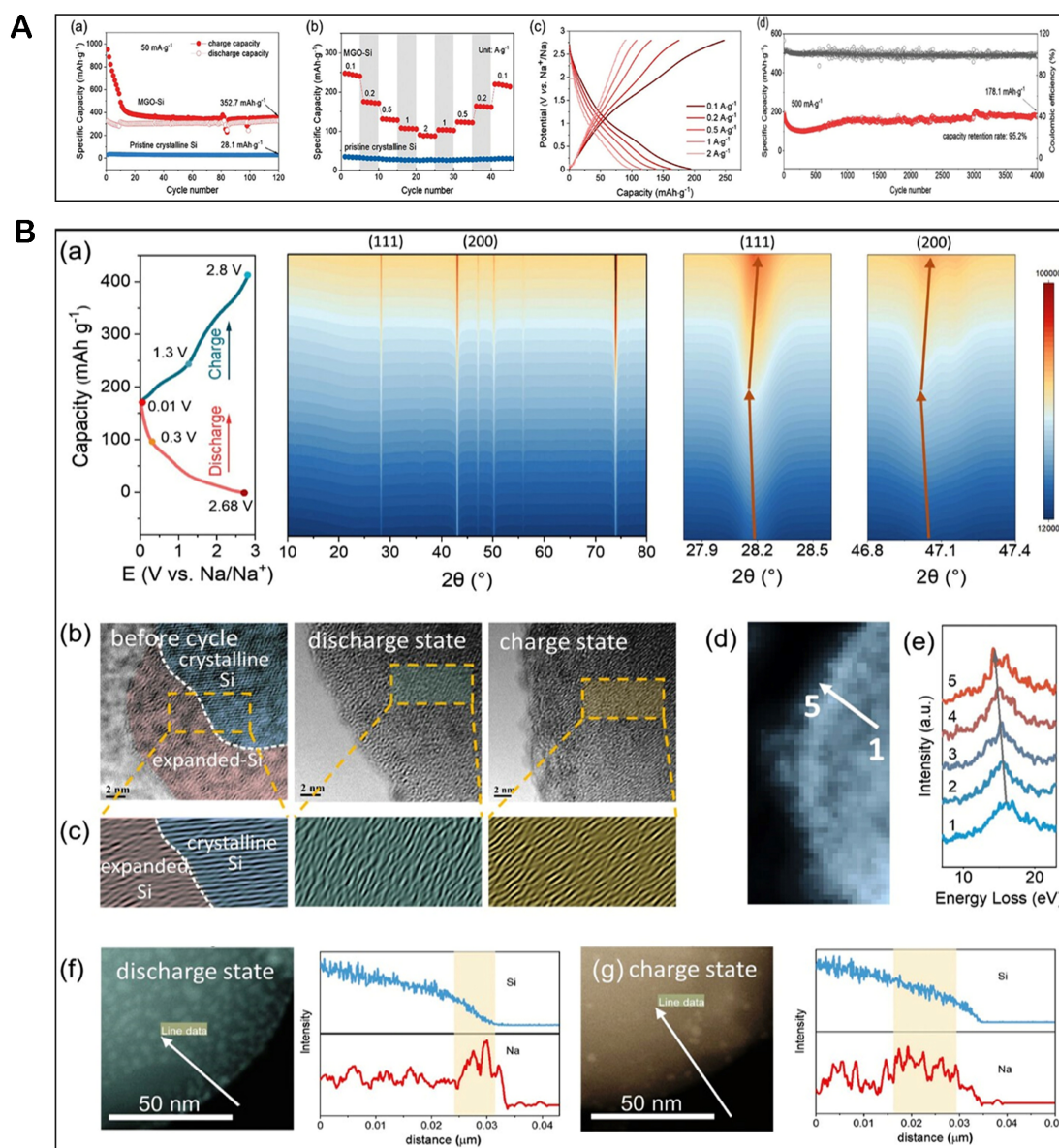


Figure 15. (A) Electrochemical Na⁺ storage capabilities of MGO-Si and crystalline Si. (a) Cyclic performances of MGO-Si and pristine crystalline Si at 50 mA g⁻¹. (b) Comparison of rate capabilities. (c) Charge/discharge curves of the MGO-Si electrode at different current densities. (d) Long-term cycling stability of MGO-Si at 500 mA g⁻¹. (B) Investigation of the reaction mechanism of the MGO-Si electrode. (a) Contour plot of *ex-situ* XRD patterns of the (111) and (200) MGO-Si peaks at different reaction cut-off voltages during the discharge cycles. (b) *Ex-situ* TEM images and (c) enlarged filtered HR-TEM images of MGO-Si before cycling and when discharged and charged. (d and e) STEM-EELS line scan and corresponding EELS spectra of sodiated MGO-Si. (f and g) TEM line scans of MGO-Si when discharged and charged. Reproduced with permission from [175]. Copyright © 2023 John Wiley & Sons, Inc.

A biomass-derived C-sheathed Si composite has been fabricated by Gong *et al.* [185]. It showed a good affinity for Na⁺ (de) insertion as an anode and sustained 99.7% of capacity retention after 1,000 cycles. Recently, a ternary composite formed by hybridizing CoSi₃P₃, FeSi₄P₄, and CNTs was first pre-deliathiated to create a LiF-rich SEI film that later sustained during (de)sodiation [186]. This novel strategy showed a superior CE of 80% with high initial discharging and charging capacities of 581 and 464 mAh g⁻¹. It sustained a capacity of 417 mAh g⁻¹ over 150 cycles.

Bismuth-based anodes for SIBs

Bismuth (Bi) has been regarded as a “green” choice for energy storage materials because of its non-toxicity, good electronic properties, and layered structure with a larger interlayer distance of 0.395 nm to accommodate Na^+ that can reversibly give Na_3Bi an optimal gravimetric capacity of 385 mAh g^{-1} ^[17,187]. Although Bi suffers low volume expansion (250%) (lower than 290% and 430% in Sb and Sn, respectively) compared to other alloying anodes, it still has commercial real-time performance potential^[188,189]. Many modifications of Bi have been proposed for stabilized performance, mostly through C compositing. However, C compositing mostly limits the capacity (less than 200 mAh g^{-1}) by imposing an additional barrier layer for ion diffusion^[188,190,191]. Although other derivatives, including intermetallics^[30], oxides^[192], sulfides^[193], selenides^[194], tellurides^[195], and others, have also been reported for high Na^+ affinity as SIB anodes^[196-198].

Both bulk and nanosized Bi anodes employing various synthetic and structural modifications have been explored widely in recent years to delimit their capacity. However, they have posed considerable bottlenecks. Mechanistic pathways during sodiation in bulk and nanoscale have not been well understood yet^[199,200]. Previously, Sottmann *et al.* have excellently addressed the impact of crystallite size in Bi SIB anodes using synchrotron XRD and XAS^[200]. Ball-milled C composited Bi samples for 20 min (Bi/C-20 min) and 24 h (Bi/C-24 h) having crystallite sizes of 129.6 and 34 nm, respectively, showed different capacity retainability. At the same time, the nanocrystalline- Bi/C-24 h sample sustained much higher capacity (about 80% of the theoretical capacity) than the Bi/C-20 min sample (20% of theoretical capacity retention). The metastable Na_3Bi cubic and hexagonal polymorphs generated during sodiation in Bi/C-24 h and Bi/C-20 min samples, respectively, had varying degrees of volume expansions responsible for the difference in sodiation capacity. *Ex-situ* XRD revealed high pulverization in the sample (Bi/C-20 min), whereby the original particle size reduced to about one-third (with inactive role). However, the particle size in the Bi/C-24 h sample did not effectively change.

Bi nanosphere-based SB anode has been recently updated by Zhang *et al.*^[201]. It showed an ultrahigh and stable capacity with an impressive longevity (10,000 cycles) at a high current density (i.e., 2 A g^{-1}). Although it delivered an unimpressive ICE (53.4%, $422.4/790.3 \text{ mAh g}^{-1}$, C/D), the electrode's high CEs of above 99% and a good capacity retention of 333.4 mAh g^{-1} were sustained at an exceedingly high ampere density of 100 A g^{-1} . An ultrafast (dis)charging SIB anode consisting of MOF-derived nanospherical Bi@C with hard C has been reported recently by Liang *et al.*^[202]. After an initial cycle capacity of 347.8 mAh g^{-1} (CE 52.4%), the composite showed a high CE of about 99% in subsequent cycles. Even at an ampere density of 80 A g^{-1} , it can provide a capacity of 308.8 mAh g^{-1} , leading to full (dis)charging in 15 s.

A potential Bi nanosheet array on CNTs for an SIB anode has been recently reported by Liu *et al.*^[203]. It delivered a stable capacity of $311.68 \text{ mAh g}^{-1}$ over 1,000 cycles at 1 A g^{-1} . Importantly, the material showed an equally admired performance when it was applied in full cell configuration with $\text{Na}_3(\text{VOPO}_4)\text{F@rGO}$ cathodic material, where an operating voltage of above 4 V was achieved with an overall energy density of $221.99 \text{ Wh kg}^{-1}$.

To minimize volume expansion and subsequent pulverization effects in Bi-contained SIB anodes, a novel galvanic replacement (with iodine ion assisted) synthesis of Bi NTs for anodes has been presented [Figure 16A]^[204]. It surpassed the currently reported performance of Bi alloying anodes in SIBs [Figure 16B]. The anode lived for 65,000 cycles (capacity of 241 mAh g^{-1} , 74% CE) at 50 A g^{-1} . It also furnished 355 mAh g^{-1} over 15,000 cycles at 20 A g^{-1} . *In-situ* TEM [Figure 16C] and *in-situ* XRD [Figure 16D] provided conclusive evidence of Bi NT stability during sodiation along with species evolution

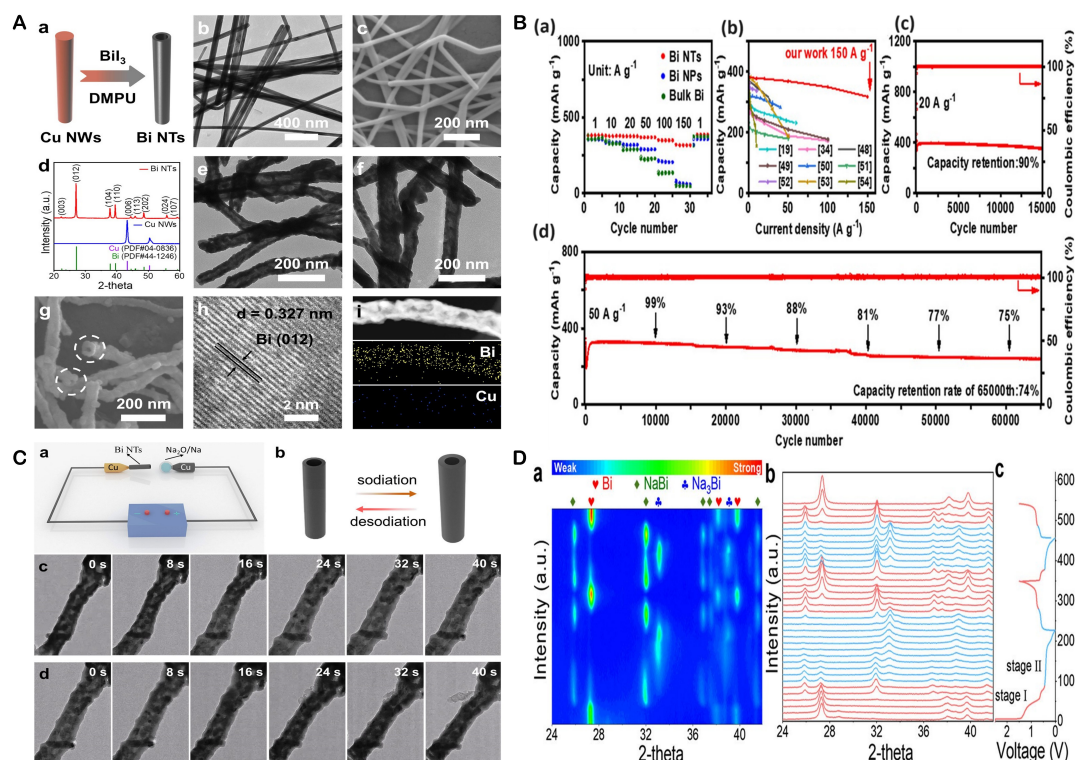


Figure 16. (A) Material characterization. (a) Illustration of Bi-NTs synthesis. (b) TEM image and (c) SEM image of Cu-NWs. (d) XRD powder patterns of Cu-NWs and Bi-NTs. (e and f) TEM images, (g) SEM image, and (h) HRTEM image of Bi-NTs. (i) Elemental mapping and EDS spectrum of Bi-NTs. (B) (a) Rate performance of Bi-NTs, Bi-NPs, and commercial bulk Bi. (b) Comparison of rate performance of Bi-NTs with many previously reported Bi-based anodes for SIBs. Long-term cycling performance of Bi-NTs at (c) 20 A g⁻¹ and (d) 50 A g⁻¹. (C) *In-situ* TEM analysis of a single Bi-NT. (a) Schematic representation of the *in-situ* nano-battery used and (b) morphological evolution of Bi-NT during cycling. Time-lapse TEM imaging of a single Bi-NT during the first (c) sodiation and (d) desodiation steps. (D) *In-situ* XRD study of the Bi-NT electrode during (dis)charge. (a) *In-situ* XRD contour plot, (b) *In-situ* XRD patterns and (c) Charge/discharge profiles of the Bi-NT electrode during initial and second (dis)charge steps. Reproduced with permission from [204]. Copyright © 2022 American Chemical Society.

at different (de)sodiation stages. Initially, the sodiation induced a high volume-change in the tubular structure, expanding the diameter from 85 to 124 nm. However, hollow structured NTs successfully accommodated stress strains during (de)sodiation without any visible cracks together. The *in-situ* XRD showed the formation of a NaBi (tetragonal) sodiated state that further moved to Na₃Bi (hexagonal) with a reverse conversion pattern during desodiation.

The compromised conductivity and volume enlargements during sodiation/desodiation of Bi anodes necessitates modification at an atomic level to leverage the conductivity along with the addition of some volume buffering media. A Bi-C-based composite has been fabricated in a multistep process that could serve as an ultrafast SIB anode with superb high-temperature utility along with optimum performance at high current densities [189]. The multi-layered design helped mitigate volumetric stresses and particle aggregation during sodiation/desodiation. It also improved ionic mobility, electrolyte wetting, and conductivity [Figure 17A]. The material was tested both in half-cell and full-cell with excellent stability and capacity retention [Figure 17B]. The initial cycle capacity was 301 mAh g⁻¹ at high temperatures. It was diminished to 245 mAh g⁻¹ at high temperatures and a current density of 200 A g⁻¹ with a good reversibility (capacity retention of 78%). The full cell with NVP sustained a capacity of 93 mAh g⁻¹ at 1 A g⁻¹ over 700 cycles and a capacity of 66 mAh g⁻¹ at a current density of 2 A g⁻¹, manifesting an ultrafast charging/discharging in just 75 S. The stability of the anode was reflected in a post cycling morphological study whereby the modified

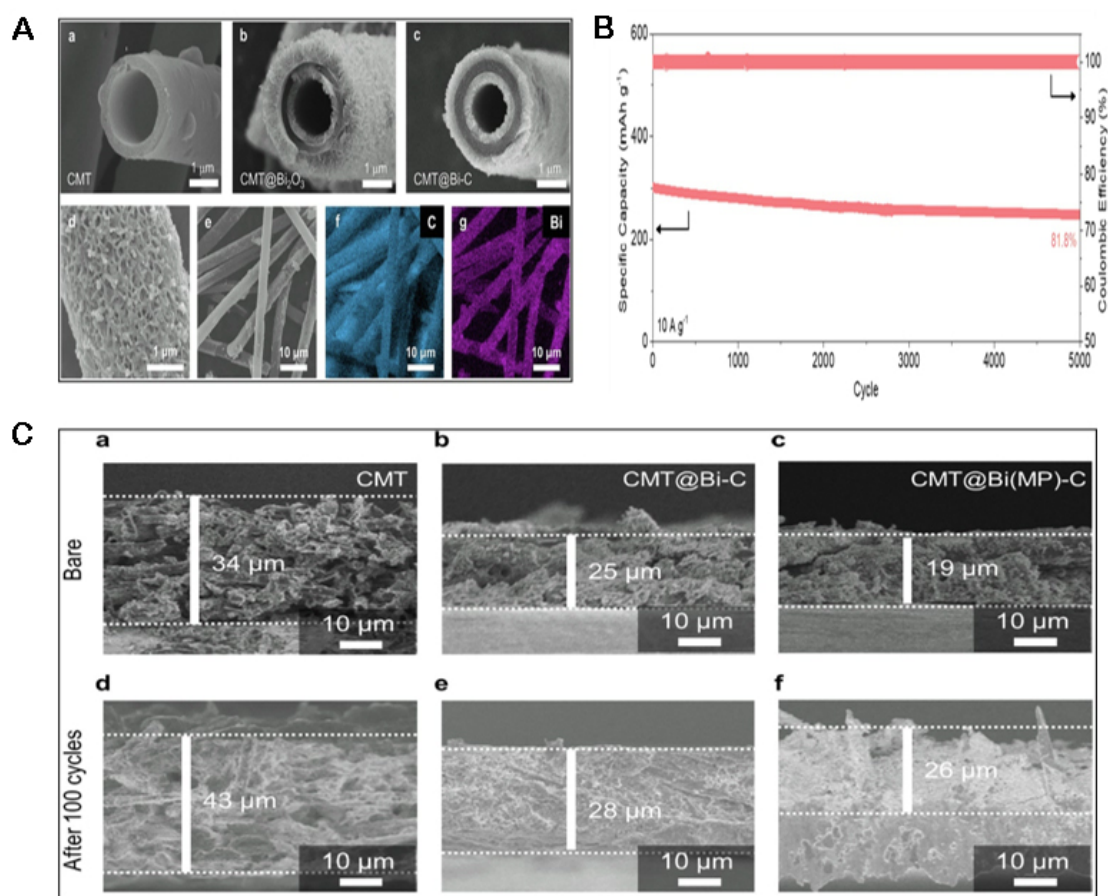


Figure 17. (A) Cross-sectional SEM images of (a) CMT, (b) CMT@Bi₂O₃, and (c) CMT@Bi-C. (d) Image showing surface morphology and (e-g) elemental mapping of CMT@Bi-C. (B) Cycle performance of CMT@Bi-C at 10 A g⁻¹ at high temperature. (C) Post cycling analysis of CMT@Bi-C. Cross-section SEM images before and after battery cycling test for (a and d) CMT, (b and e) CMT@Bi-C, and (c and f) CMT@Bi(MP)-C anodes are shown. Reproduced with permission from [189]. Copyright © 2023 Elsevier.

electrode showed good integrity with diminished SEI and minimal structural changes [Figure 17C]. Similarly, Sb₃Bi₂ alloy anodes in SIBs delivered a high ICE of 87.1% at 0.1 A g⁻¹. The electrode exhibited low polarization effects. It could furnish a high capacity of 625 mAh g⁻¹ after 100 cycles at 1 A g⁻¹ [42]. Electrochemical performances of representative alloy-based anode materials explored for SIBs were compared. Results are provided in Table 2.

MATERIAL DESIGN STRATEGIES

Nanostructuring and controlling morphology

Alloying SIB anodes face multiple issues, including high volume expansions, particle aggregation with pulverization, high drop in ICE, low Na⁺ and electronic mobilities, and unfavored kinetics, all leading to low reversible capacities. From the material's perspective, many of these limitations can be fixed by opting for rational material design such as nanostructuring and controlled morphological architectures to have a real-world benefit of improved performance. The high and active surface area of nanostructured alloys not only enhances interfacial interactions between electrolyte and electrode, but also offers high Na⁺ diffusion at shortened paths, particularly over carefully designed nano-morphologies, thereby enhancing the kinetics of ion transfer. Although nanosizing offers the above-mentioned benefits of adding mechanical strength and mitigating pulverization of other detrimental effects, they entail different degrees of drawbacks, including

Table 2. Comparison of electrochemical performances of representative alloy-based anode materials for SIBs

| Anode materials | Synthetic method | ICE [%] | Charge/discharge capacity [mAh g ⁻¹] | Cycles | Current density [mA g ⁻¹] | Electrolyte | Ref. |
|--|--|---------|--|--------|---------------------------------------|--|-------|
| Tin-based anode materials | | | | | | | |
| Tin-based oxides | | | | | | | |
| SnO ₂ @CNFs/CNTs | Electrospinning | 54.3 | 460.3 | 200 | 100 | NaClO ₄ /EC/PC/FEC | [76] |
| SnO _{2-x} /C | Electrospinning | 55.2 | 565 | 2,000 | 1,000 | NaClO ₄ /EC/DEC | [77] |
| SnO ₂ /NG | Hydrothermal | 27.8 | 409.6 | 100 | 50 | NaClO ₄ /PC/EC/FEC | [78] |
| SnO ₂ /NiO@C | Electrospinning/deposition/carbonization | 69.0 | 320 | 200 | 100 | NaClO ₄ /EC/DEC/FEC | [205] |
| SnO ₂ NRs/GA | Hydrothermal | 58.4 | 232 | 100 | 50 | NaClO ₄ /EC/DEC | [79] |
| SnO ₂ -hard carbon | Hydrothermal carbonization | 36.6 | 184 | 250 | 0.1 C | NaClO ₄ /EC/PC | [80] |
| a-SnO ₂ NH | Oblique angle deposition | 53.1 | 915 | 50 | 2,000 | NaPF ₆ /EC/DMC/FEC | [81] |
| SnO ₂ @hCNT | Hydrothermal | 50.0 | 223 | 100 | 100 | NaClO ₄ /EC/DEC | [82] |
| SnO ₂ @CC | Solvothermal | 85 | 498 | 100 | 200 | NaClO ₄ /EC/DMC | [83] |
| SnO ₂ /MXene | Hydrothermal | 36.54 | 208.6 | 100 | 400 | NaClO ₄ /EC/DEC | [84] |
| BTO@SnO ₂ @P-C | Template assisted solvothermal synthesis | - | 144.4 | 10,000 | 10,000 | NaClO ₄ /EC/DEC/FEC | [206] |
| Tin-based sulfides | | | | | | | |
| SnS ₂ /Co ₃ S ₄ | Co-precipitation and hydrothermal | 59.16 | 1,141.8 | 50 | 100 | NaClO ₄ /DEC/EC/FEC | [85] |
| SnO ₂ @SnS ₂ @NG | Hydrothermal | 54.6 | 100 | 200 | 3,000 | NaClO ₄ /EC/DEC | [92] |
| SMS/C NBs | Wet chemical method | 90.8 | 522.5 | 500 | 5,000 | NaCF ₃ SO ₃ /DEGDME | [93] |
| SnS ₂ /EPC | Nanocasting | 68 | 340 | 450 | 2,000 | NaPF ₆ /DME | [86] |
| SnS ₂ QDs/Ti ₃ C ₂ | Hydrothermal | 55.1 | 345.3 | 600 | 100 | NaClO ₄ /EC/DEC/DMC | [87] |
| SnS ₂ /FeS ₂ /rGO | Hydrothermal | 65 | 768.3 | 100 | 100 | NaClO ₄ /EC/DEC/FEC | [207] |
| PEG-SnS ₂ /rGO | Hydrothermal | 74.2 | 770 | 100 | 100 | NaPF ₆ /EC/DEC | [88] |
| 1T-SnS ₂ /RGO | CVD/spray coating | 97.4 | 648.1 | 100 | 500 | NaClO ₄ /EC/DMC | [89] |
| SnS-SnS ₂ @GO | Solvothermal | 69.7 | 450.6 | 100 | 100 | NaClO ₄ /EC/DMC/MEC/FEC | [90] |
| ZnS/SnS ₂ @NCNFs | Electrostatic spinning | - | 174.5 | 1,000 | 5,000 | NaClO ₄ /PC/EC/FEC | [91] |
| Tin-based selenides | | | | | | | |
| SnSe ₂ @C | Solvothermal | 83.1 | 182.7 | 1,000 | 5,000 | NaCF ₃ SO ₃ /DIGLYME | [94] |
| SnSe ₂ /ZnSe@PDA | Mechanical mixing | 71.6 | 616 | 1,000 | 1,000 | NaPF ₆ /DME | [96] |
| SnSe ₂ /Ti ₃ C ₂ T _x | Liquid phase reduction and selenylation | - | 245 | 445 | 1,000 | NaPF ₆ /DOL/DIGLYME | [97] |
| MoSe ₂ /SnSe ₂ @C | hydrothermal reaction | 63.7 | 591.4 | 110 | 100 | NaClO ₄ /EC/PC/FEC | [98] |
| Tin-based phosphide | | | | | | | |
| Sn ₄ P ₃ -GA | Hydrothermal-phosphidation | 67.3 | 657 | 100 | 100 | NaClO ₄ /EC/DMC | [102] |
| Sn ₄ P ₃ @C | Solvothermal-phosphidation | 64 | 420 | 300 | 200 | NaClO ₄ /EC/DMC/FEC | [103] |
| Micron-sized Sn ₄ P ₃ | High energy mechanical milling | 89.8 | 719.7 | 100 | 100 | M NaPF ₆ in diglyme (DGM) | [104] |
| Sn ₄ P ₃ @CNT/C | Hydrothermal reaction | 85.2 | 742 | 150 | 200 | NaPF ₆ /DME | [105] |
| Sn _x P _y /RGO | Reduction/phosphorization | 54.57 | 421.8 | 100 | 500 | - | [101] |
| Sn ₄ P ₃ HS@MXene | Phosphorization | 82.3 | 373.2 | 150 | 100 | NaPF ₆ /DEC/EC/FEC | [106] |
| Sn/Sn ₄ P ₃ @MXene | Solvothermal | 65.7 | 127.8 | 1,000 | 2,000 | NaPF ₆ /DEC/EC/FEC | [107] |
| Sn _x P _y /NG | Carbonization-phosphorization | 52.6 | 203.1 | 300 | 1,000 | NaClO ₄ /EC/DEC/FEC | [99] |

Antimony-based anode materials**Antimony-based oxides**

| | | | | | | | |
|--|--|------|-------|-----|------------------------|--------------------------------|-------|
| Octahedral Sb ₂ O ₃ | Hydrothermal | 53.3 | 435.6 | 50 | 100 | NaClO ₄ /PC/FEC | [123] |
| Sb ₂ O ₃ @Sb | single-step dealloying | 67.9 | 659 | 200 | 29.7 A g ⁻¹ | NaClO ₄ /PC/FEC | [125] |
| Sb/Sb ₂ O ₃ @NCNFs | electrospinning and carbon thermal reduction | 69.9 | 527.3 | 100 | 100 | NaClO ₄ /EC/DMC | [126] |
| Sb ₂ O ₃ @Sb | Dealloying/oxidation | 79.8 | 526.2 | 150 | 1,000 | NaPF ₆ /EC/DEC/FEC | [127] |
| Sb ₆ O ₁₃ NPs@C | Hydrothermal | 40.2 | 239 | 170 | 1,000 | NaClO ₄ /EC/DEC/FEC | [128] |
| Sb ₂ O ₃ -CNT-Graphene aerogel | Hydrothermal | 46.9 | 360 | 100 | 100 | NaClO ₄ /PC/FEC | [130] |
| Sb ₂ O ₃ -EGO | Wet chemical | - | 345 | 100 | 100 | NaClO ₄ /PC/DMC/FEC | [129] |

Antimony-based sulfides

| | | | | | | | |
|---|---------------------------------------|-------|-------|-------|---------------------|--|-------|
| I-S@MCNTs | Solvothermal | - | 400 | 1,000 | 400 | NaClO ₄ /EC/DEC/FEC | [133] |
| Sb ₂ S ₃ /SCS | Solvothermal | 61.27 | 455.8 | 100 | 100 | NaClO ₄ /PC/FEC | [131] |
| Sb ₂ S ₃ /CS | Electrospinning/hydrothermal | 61 | 321 | 200 | 200 | NaClO ₄ /PC/EC/FEC | [132] |
| α-Sb ₂ S ₃ -CuSbS ₂ | Closed-space sublimation | 82.19 | 506.7 | 50 | 50 | NaCF ₃ SO ₃ in diglyme | [208] |
| Sb ₂ S ₃ @FeS ₂ | Solvothermal method | 82.4 | 534.8 | 1,000 | 5,000 | NaCF ₃ SO ₃ in DEGDME | [134] |
| Sb/CNTs | Electrochemical desulfurization | 71 | 510 | 200 | 100 | NaClO ₄ /PC/FEC | [209] |
| Sb ₂ S ₃ @SnS@C | Hydrothermal/calcination | 79.0 | 442 | 200 | 1,000 | NaClO ₄ /EC/DMC/FEC | [135] |
| Sb ₂ S ₃ @m-Ti ₃ C ₂ T _x | Wet Chemical | - | 156 | 100 | 100 | NaClO ₄ /EC/PC/FEC | [136] |
| Sb ₂ S ₃ @NCR | Carrboniazation/gas-phase sulfuration | 67.8 | 208 | 100 | 200 | NaClO ₄ /EC/DMC/FEC | [210] |
| MoS ₂ @Sb ₂ S ₃ /rGO | Hydrothermal/sulfidation | 80.6 | 162.1 | 1,100 | 5,000 | NaClO ₄ /EC/DEC | [138] |
| NF-Sb ₂ S ₃ @rGO | Hydrothermal | 72.6 | 544.8 | 200 | 100 | NaClO ₄ /PC/EC/FEC | [211] |
| Sb ₂ S ₃ /S@S-doped carbon | Template assisted/coupling reaction | 63.5 | 310 | 500 | 1 A g ⁻¹ | NaClO ₄ EC/DEC/DMC/FEC | [212] |

Antimony-based selenides

| | | | | | | | |
|--|------------------------------------|------|-------|-----|-------|--------------------------------|-------|
| α-Sb ₂ Se ₃ /C | Ball milling | 65.7 | 378 | 50 | 50 | NaClO ₄ /EC/PC/FEC | [141] |
| ZnS/Sb ₂ S ₃ @NC | Solvothermal | 67.9 | 511.4 | 450 | 1,000 | NaPF ₆ /diEGME | [213] |
| Sb ₂ Se ₃ /CNT | Ball milling | 78.9 | 428 | 200 | 50 | NaClO ₄ /EC/PC/FEC | [143] |
| Sb ₂ Se ₃ /rGO | Solvothermal | 67.3 | 511 | 50 | 500 | NaClO ₄ /EC/DMC/FEC | [144] |
| Sb ₂ Se ₃ @rGO@NC | Solvothermal | 56.0 | 288.5 | 100 | 50 | NaClO ₄ /DEC/EC/FEC | [145] |
| Sb ₂ Se ₃ /Ti ₃ C ₂ T _x | Electrostatic Self-assembly method | 87.1 | 568.9 | 100 | 100 | NaClO ₄ /PC | [146] |

Phosphorous-based anode materials

| | | | | | | | |
|--|--|--------|---------|-------|---------|--------------------------------|-------|
| NPRP@RGO | Typical redox reaction | 78.5 | 1,249.7 | 150 | 173.261 | NaClO ₄ /PC/FEC | [150] |
| P-SPAN | Ball milling | 71.7 | 1,355 | 100 | 520 | NaClO ₄ /EC/DEC/FEC | [151] |
| RP/Graphite | Wet milling/dry milling | ≈ 70.0 | 1,354 | 100 | - | NaPF ₆ /EC/DEC/FEC | [152] |
| NRP-rGO | Phosphorus-amine-based method | 61.2 | 662 | 1,400 | 2,000 | NaClO ₄ /EC/DEC/FEC | [154] |
| RP-Porous C | Ball milling | 87.3 | 1,070 | 200 | 400 | NaClO ₄ /EC/DEC/FEC | [153] |
| P@AC@PPy | VDC/interfacial polymerization | - | 484 | 200 | 200 | NaClO ₄ /EC/DEC/FEC | [155] |
| RP/CS | vaporization-condensation | 49.3 | 1,027 | 2,000 | 4,000 | HClO ₄ /EC/DMC/FEC | [156] |
| P _{red} @CNF | Vaporization-condensation | - | 1,850 | 500 | 100 | NaPF ₆ /EC/DEC/FEC | [157] |
| RP@CNC | Phosphorus-amine method/evacuation-filling process | 67.5 | 1,363 | 150 | 100 | NaClO ₄ /EC/DEC/FEC | [214] |
| Sb _x -RP _(70-x) /C ₃₀ | Ball milling | ≈ 90 | 1,650 | 70 | 0.333 C | NaPF ₆ /PC/FEC | [215] |
| WDC/CNTs@RP | Vaporization-condensation | 81.21 | 636.3 | 700 | 1 C | NaClO ₄ /EC/DMC/FEC | [159] |
| RP-MWCNT/MXene | Blending/grinding | 65 | 371.6 | 100 | 500 | NaPF ₆ /EC/DEC/FEC | [158] |

| | | | | | | | |
|--|---|-------|-------|--------|--------|--|-------|
| RP@BP/3DNG | Solvothermal | 65.3 | 706.5 | 200 | 500 | NaClO ₄ /EC/DMC/FEC | [216] |
| 2D-Nanoplatelets RP/SWCNTs | Liquid phase exfoliation | 81 | 451 | 1,000 | 2,500 | NaPF ₆ /EC/DMC/FEC | [160] |
| S-doped P/C | Chemical presodiation strategy | 98.7 | 853.6 | 100 | 200 | NaClO ₄ /EC/PC/FEC | [217] |
| Germanium-based anode materials | | | | | | | |
| Zn ₂ GeO ₄ @C | Hydrothermal/pyrolysis | 67.6 | 317 | 50 | 100 | NaOTf/diglyme | [168] |
| MGePx | Solvothermal | 65.28 | 704 | 100 | 240 | NaPF ₆ /FEC/DEC | [169] |
| GeP | High temperature - pressure solid state synthesis | 78 | 330 | 100 | 100 | CF ₃ NaO ₃ S/TEGDME | [94] |
| GeP/C | Ball milling | 93 | 850 | 300 | 100 | NaCF ₃ SO ₃ /Diglyme | [171] |
| GeTe/C | Ball milling | 73 | 315 | 100 | 50 | NaPF ₆ /EC/DMC/FEC | [172] |
| GeSe-NWs | Rapid box thermal deposition | 74.5 | 433.4 | 50 | 200 | NaClO ₄ /EC/PC | [105] |
| GeS ₂ | sulfidation- cooling and calcination | 95.1 | 512.8 | 1,000 | 10,000 | NaClO ₄ /PC/FEC | [173] |
| N,S-Ge@PCNFs | Centrifugal spinning/heat treatment | - | 443 | 200 | 1,000 | NaClO ₄ /EC/PC/FEC | [174] |
| Silicon-based anode materials | | | | | | | |
| Si/SiO ₂ -OMC | Hydrothermal-reduction | - | 423 | 100 | 50 | NaClO ₄ | [183] |
| SiP ₂ /C | Ball milling | 76 | 410 | 100 | 50 | NaClO ₄ /EC/DEC/FEC | [218] |
| Si _{0.07} Sb _{0.93} | Co-sputtering | - | 663 | 140 | 100 | NaClO ₄ /EC/DEC/FEC | [184] |
| Si@C | Thermal treatment | - | 174 | 1,000 | 100 | - | [185] |
| MGO-Si | - | - | 178.1 | 4,000 | 500 | NaPF ₆ /DEGDME | [175] |
| Bismuth-based anode materials | | | | | | | |
| Bi@N-C | Carbonization | 57.08 | 307 | 400 | 1,000 | NaPF ₆ /DEGDME | [219] |
| Bi ₂ Se ₃ @C | Spin coating-thermal treatment | - | 375.3 | 100 | 100 | NaClO ₄ /EC/DMC/EMC/FEC | [220] |
| N-C@Bi/G | Hydrothermal/thermal | 78.87 | 260 | 1,000 | 2,000 | - | [221] |
| Sn-Bi@C | Hydrothermal/thermal | 83.6 | 461 | 100 | 100 | NaPF ₆ /EGDME | [222] |
| Bi@NC | Solvothermal/carbonization | 85.1 | 324.2 | 5,000 | 10,000 | NaPF ₆ /1,2-dimethoxyethane | [223] |
| Bi ₂ S ₃ @C@CoS ₂ | Solvothermal/calcination | 93.6 | 417.7 | 1,600 | 2,000 | NaCF ₃ SO ₃ /DEGDME | [224] |
| LC-Bi | Solvothermal | 96 | 264 | 10,000 | 5,000 | NaPF ₆ /DME | [201] |
| Bi-NS | Molten thermal reduction | 75.6 | 409.7 | 3,000 | 500 | NaPF ₆ /DIGLYME | [225] |

highly reactive nanodomains that participate in parasitic side reactions involving Na⁺ that can add to unstable SEI, causing more irreversible capacity loss.

The most important challenge in designing alloying materials for SIBs is enhancing their electrochemical performance. In both LIBs and SIBs, the energy storage mechanisms of alloying materials are not significantly different. So, tracking the path of material design strategies for LIB applications has eased the selection of suitable methodologies for uniform and controlled assembling of electrode materials for optimum performances in SIBs. However, it is also important to recognize the differences in the physical properties of Na and Li ions. Many studies have explored the effectiveness of precisely designed morphologies with 0D, 1D, 2D, and 3D patterning ranging from nanowires, NTs, and yolk-shell structures to various porous nano-assemblies and many other morphological displays previously proven successful in the LIBs^[24,226]. These improved structures have been proven to be effective in volume buffering, improved

interfacial contacts, and ionic and electronic conductivities. In many cases, a porous composite structure has dual benefit of involvement of multiple active species at different stages of the sodiation/desodiation, which helps in overall improved kinetics along with shuttering effects of volumetric stresses, which ensures stable capacities over extended cycling^[17,28].

Heterostructure and composites design

Recently, compositing methodologies have been much in the limelight for their adaptable surface and bulk properties, matching with desired SIB anode characteristics. In this regard, fabrication of metallic, polymeric, and other hybrid composites often involving a carbonaceous material comes as the foremost choice primarily due to enhanced conductivity and multiple short diffusion pathways with intermittent pores in 3D materials that can afford volume expansions with other added advantages. Often, binary or ternary phase composites have some surface functionalities and defects that garner their effectiveness. Nonetheless, these hybrid phases contribute to side reactions that, in many instances, have been directly linked to initial high-capacity losses^[26].

Ahead of others, carbon-based materials always positively contribute to overall performance and long-cyclic capacity retention. It is worth mentioning that capacity boosting, conductivity enhancement, and volume shuttling effect of graphitic carbons in the form of graphene, CNTs, CF, and others often afford 3D interconnected channels that cascade ion shuttling kinetics with improved stability, particularly buffering volumetric expansion and particle aggregation drawbacks^[33,227]. Delocalized electrons in the defect/vacancies of graphitic frameworks are grave concerns and entailed as Na⁺ ion binding sites. Thus, defect/vacancy creation using single and dual heteroatom doping at a certain level is vitally benign in improving SIB anode performance^[17,145,228-231].

Tailoring intermetallic alloy composition

Many recent studies have determined the potential of definite intermetallic alloy compositing for SIBs anode. In these advanced heterostructure cum compositing-alloying methodologies, binary, ternary, and even quaternary phases can synergistically and coherently support sodiation/desodiation processes^[29,164,232-234]. These synthetic strategies have allowed notable improvisations in the material's performance as SIB anodes. They have been discussed in detail in optimization strategies.

CHALLENGES ASSOCIATED WITH SIBS

SIBs are on the way to improved performance, particularly aimed at grid-level applications. However, there are still several challenges that need immense attention to dominate in the lithium era. Despite the aforementioned material design strategies in Section "MATERIAL DESIGN STRATEGIES", there are still main bottlenecks in the vast applicability of alloying SIB anodes. The challenges facing the SIB system include Volume Variations, Voltage Hysteresis, Inadequate Mechanistic Understanding, and Unstable Solid Electrolyte Interphase, as presented in Figure 18. In the case of carbon-composited SIB alloying anodes, scanning the role of defects/functionalities in high initial capacity fading needs to be fixed before presenting SIBs commercially. In the case of intermetallic and conversion-alloying anodes, evolution of intermediate phases and the volume variations need to be probed to deliver sustaining capacities as SIB anodes.

Volume variations

Large-sized Na⁺ insertion with subsequent alloying during the sodiation causes drastic volume variations that can lead to irreparable structural damage to the alloying host. Accompanying issues include pulverization of the uniquely designed active material to the point of losing electrical contact with current collectors and rendering the SEI unstable, thereby imparting huge initial capacitive losses. Typical volume expansions for alloying anodes vary. They are often reported to range from 200% to 400%, with the highest

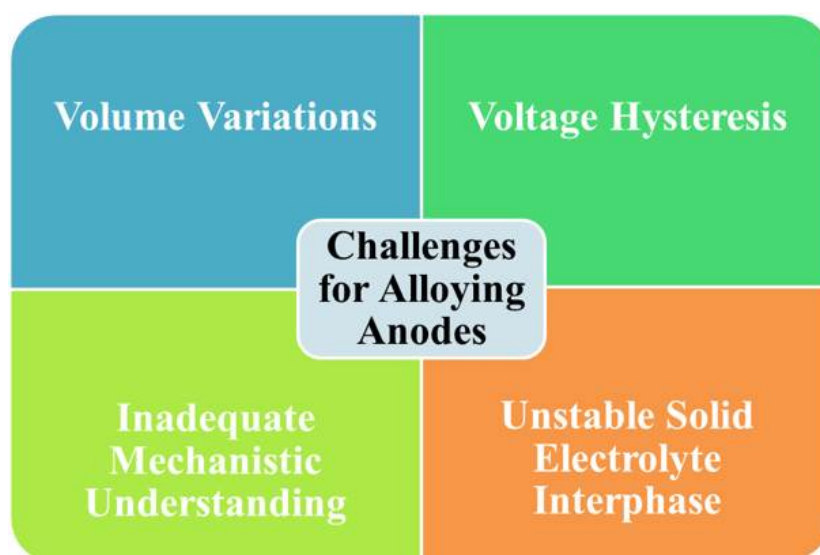


Figure 18. Major challenges faced by alloying SIB anodes.

expansions in the most promising anodes such as Sn, Sb, Bi, and P. Besides universal methodologies of C compositing, various structural engineering methodologies to introduce a volume buffering medium have been vastly reported^[17,29].

Voltage hysteresis

Voltage hysteresis is another challenge that both LIBs and SIBs alloying anodes suffer. Despite various prepositions made for the origin of voltage hysteresis, the root cause is not very well understood yet. Voltage hysteresis reflects capacity loss. It has both kinetic and thermodynamic origins. Unstable SEI, low ionic motilities, structural transformations, and other barriers in ionic/electronic transportation have been mostly nominated as causes of voltage hysteresis.

Voltage hysteresis represents a potential gap between discharge and charge cycles. It highlights an unsteady performance of the selected electrode material in SIBs. Electrodes showing large voltage hysteresis have impractical cyclic efficiency. Large voltage hysteresis is associated with other capacity deprivation problems. Reaction overpotential, ohmic polarization, and component inhomogeneity between charged and discharged stages are labeled as culprits for overpotential. They can be determined using galvanostatic and potentiostatic intermittent titrimetric analysis. Among these three factors, composition inhomogeneity arises from diffusion of Na^+ in the solid state with different Na^+ rich and Na^+ deficient layers being formed at the material's surface during sodiation and desodiation, respectively^[17,41].

Unstable solid electrolyte interphase

The most addressed and key issue in LIBs and SIBs is unstable SEI formation that is always formed at an electrode-electrolyte interface. Anode materials having high fermi levels can induce reduction of electrolytes, whose LUMO lies below that of anode material. The SEI layer is ion-conducting in nature. It is an electron insulator. However, it does offer much resistance to Na^+ diffusion in a thick form. While a stable, suitably thin SEI is vital for suppressing electrolyte side reactions although, in most cases, it is highly difficult to have a stable and non-degrading thin SEI. One of the major capacity-fading roles is displayed by this SEI, which often constantly forms and degrades, causing a substantial loss of Na^+ . Particularly for alloy anodes, stabilizing SEI is quite difficult. When stress generated at the interface during sodiation/desodiation

exceeds the stability limit of SEI, it causes its degradation and makes a fresh surface prone to generation of new SEI that eventually gets peeled off after a certain thickness, making a portion of Na^+ unavailable. Many studies have detailed the origin, morphology, and mechanism of SEI formation, along with its detection and evidence during electrochemical charging/discharging. SEI formation and its stabilization have been extensively presented in the literature and various modulating methods such as the use of electrolytes and additives have been proposed^[17,66,235–237]. A detailed account is presented in the optimization section of electrolyte.

Inadequate mechanistic understanding

Multicomponent battery systems need detailed mechanistic understandings that vary with the type and morphologies of materials used as anodes, cathodes, electrolyte systems, and many other factors involved in the charging and discharging processes. Unfortunately, for alloying SIB anodes, there is little consensus on the mechanism of charge storage as the compact and sealed battery environment presents challenges in *ex-situ* characterization. There is a need for applications of operando characterization techniques for the detailed origin of species in different states of (de)sodation^[235]. Although there is a slow but increasing trend in utilizing operando advanced characterization tools, they pose many difficulties in terms of specific assemblies to truly track the origin of species, capacity failure, the role of materials and intermediates evolved in capacity degradation. Due to the complex nature of species that evolve with different chemical states, such as the presence of variant oxidation states and crystalline/amorphous phases in different levels of (de)sodiated states, a single *in-situ* characterization tool often proves less useful for a concrete understanding of the mechanism. Similarly, the first sodiation cycle often shows different characteristics than subsequent cycles due to diverse mechanisms/species involved in SEI formation and other side reactions. For binary and ternary alloy composites, further complications can occur due to multiple phases that arise during cycling^[26,31].

OPTIMIZATIONS OF SIBS

The development of SIBs started alongside LIBs. However, their low energy density, coupled with other effects partly due to large Na^+ size, has not ascended at a commercial scale to replace costly LIBs. Although many commercial-scale SIBs have been presented by companies such as Novasis, Faradion, Natron Energy, AGM, TIAMAT, Altris, and others, they have proven renaissance for improvisations in SIBs performance^[238]. Recently, many companies (including China's BYD and Swedish NORTHVOLT) have claimed breakthroughs in SIBs, nominating them as “Rising stars” for commercial-scale applications^[239]. Despite that, it seems realistic that the current decade will be dominated by high-performing LIBs because most research studies on SIBs put forth hitherto suffer from major capacity degradation processes that need to be addressed immediately. In this regard, many optimizations in electrolyte, binder, structural, and surface engineering are necessary to cope with challenges alloying SIB anodes face.

Efficient electrolyte system

A major concern in SIB alloy anodes is their low ICE with a major contributor being the electrolyte, which participates in formation of SEI, which, in turn, determines capacity retention, cyclic stability, and performance. Particularly, the stability of an SEI and the overall capacity and efficiency highly depend on the electrolyte system. Few electrolyte systems have proven their compatibility when coupled with alloying anode materials in SIBs. A relatively thin and sustaining SEI formed from a well-matched electrolyte and additive combination consumes electrolyte molecules and Na^+ into the active passivation layer. The electrolyte in SIBs should have the following characteristics: (i) a low difference between its LUMO and the electrode's Fermi level; (ii) a good ionic conductivity along with lower viscosity; (iii) anode and cathode material's compatibility with the electrolyte; (vi) thermal stability; and (v) cost effectiveness^[31].

Commonly employed electrolytes in SIBs include NaClO_4 , NaPF_6 , sodium bis(trifluoromethane) sulfonamide (NaTFSI) in conjunction with organic solvents such as ethylene carbonate (EC), propylene carbonate (PC), dimethyl carbonate, and so on^[66,240-242]. However, each electrolyte system inherently involves some capacity fading phenomena to a different degree. NaClO_4 is less moisture adsorbing than NaPF_6 . However, when they are combined with carbonate-based solvents, both could not minimize ICE loss in a wide variety of SIBs, although ICE losses are much diminished in ether-based solvent systems (diglyme, triglyme, DME, tetrahydrofuran (THF), and so on)^[243]. Other than ether-based additives, the most concerned and effective electrolyte additive in SIBs is fluoroethylene carbonate (FEC), which, in combination with other additives, has a pivotal ICE-sustaining role^[26]. Electrolyte additives not only play a vital role in stabilizing the SEI and electrochemical capacity retention, but also have diverse effects on the electrolyte itself. Electrolyte additives are believed to participate in SEI formation and stabilization. They can also inhibit side reactions that deteriorate the SEI^[65].

The recent shift toward the utilization of ionic liquid^[244-246] and solid^[247,248] electrolytes has ample success stories. A wide potential window, low flammability, and high temperature workability are some of the features that have received much interest. However, both ionic liquid^[244-246] and solid^[247,248] electrolytes need optimizations in terms of electrochemical and techno-economic limitations for their commercialization. Although various models for SEI have been proposed, there is very little knowledge of SEI formation mechanism and its *in-situ* analysis in alloy-based anodes^[249-251]. The composition of the SEI film can give some clues about the species' involvement along with possible underlying reaction mechanisms. Recently, Zhang *et al.* have designed 3D carbon-coated Bi nanospheres as SIB anodes^[201]. These anodes showed a stable performance of up to 10,000 cycles at 2 A g^{-1} with a rate capability performance of 94% under 100 A g^{-1} . They compared SEI compositions using linear and cyclic ether-based and ester electrolytes to confirm the presence of an inorganic-rich composition of the SEI along with organic species. In both ether and ester-based solvents, the formation of Na_2CO_3 , NaF , and other organic species was detected. Particularly, the presence of NaF facilitated Na^+ diffusion. Whereas in an ester-based solvent, the increased F-content at depth rendered more organic species at the electrode surface, contributing to low ion conduction with thick and unstable SEI formation. Meanwhile, in ether-based solvents, a homogeneous distribution of NaF resulted in stable SEI that improved the performance of the Bi nanosphere-based anode. However, such studies are not very common to elucidate the exact mechanism or involvement of different species in the charge/discharge reaction.

Lately, Yang *et al.* have also given details about the origin of SEI components by performing in-depth XPS studies^[75]. They also validated the presence of organic and inorganic species evolving from electrolyte decomposition in different electrolyte systems with their effects on SEI stabilization. In the DEGDME solvent, a stable fluorinated SEI evolved by decomposition of the NaPF_6 electrolyte optimized the SIB performance. Also, the DEGDME and its complex $[\text{NaPF}_6\text{-DEGDME}]^+$ presented a higher HOMO energy and helped form sustaining cathode electrolyte interphase, as shown in Figure 19A. In fact, electrolyte has various interactive roles, among which solvation of Na^+ is very critical as it can affect SEI growth and its stability. The DEGDME solvent has recently been shown to be able to create a hybrid organic-inorganic SEI that synergistically involves carbonaceous materials to impart stability to SEI without much ionic hindrance. The DEGDME solvent also interacts with the C in heterostructured composites to maintain structural variations upon cycling. The cyclic performance in DEGDME and EC/PC solvent [Figure 19B] highlighted improved capacity and cyclability. The flair of DEGDME solvent for better compatibility with NaPF_6 than the commonly used EC/PC solvent was proved by DFT calculations that showed a higher energy difference for electron promotion from HOMO to LUMO than in commonly employed carbonate-based electrolytes^[241].

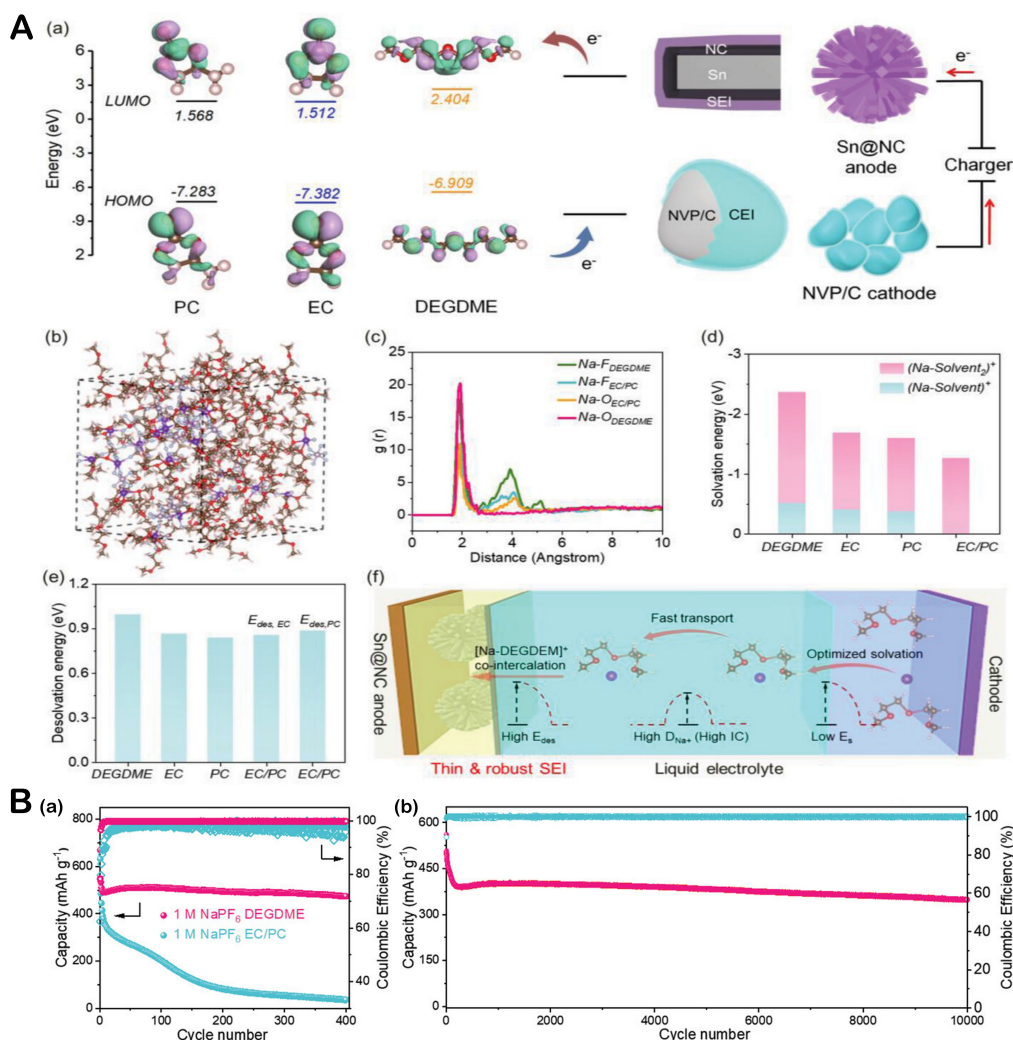


Figure 19. (A) Diagram of HOMO and LUMO energy levels showing electron acceptance and donation ability of EC, PC, and DEGDME. (b) AIMD simulation snapshots of DEGDME-based electrolyte. (c) Radial distribution functions $g(r)$ of Na-O and Na-F pairs in both electrolytes. (d) Solvation energy and (e) desolvation energy of Na^+ -solvent complexes. (f) Schematic illustration of reaction kinetics of Sn@NC full cells with DEGDME-based electrolyte. (B) (a) Cyclic performances at 1.0 A g^{-1} in both electrolytes (b) Long-term cycling for 10,000 cycles of composite anodes at 5.0 A g^{-1} in DEGDME-based electrolyte. Reproduced with permission from [75]. Copyright © 2023 John Wiley & Sons, Inc.

Effective binders

The biggest dilemma of high-volume expansions in alloying anode materials in SIB may have multifactorial origination. However, the role of the binder is very crucial in this regard. The binder not only holds the active material onto the current collector, but also plays a role in managing the stress for volume variations, particularly in alloying anodes. In addition, it safeguards the integrity of isolated electrode particles. Huge volume variations also have detrimental effects on the electrical conductivity of the active material, which is ensured by an efficient network established by the binder. The commonly employed polyvinylidene fluoride (PVDF) binder has been proven to be inefficient in SIBs. Its decomposition products have been found to be responsible for low ICE with a negative impact on long-term cycling performance^[26,252,253]. Moreover, the binder has a typical role in minimizing the pulverization issue. It also mitigates regrowth of fresh SEI and sustains SEI to ensure a high ICE. Other than PVDF, many binders have shown to have suitable performances in SIBs, including Chitosan, sodium carboxymethyl cellulose, sodium alginate, and so

on^[252,254-256]. These binders have very little volume swelling effects in organic electrolytes, which is beneficial for inducing solvent-binder interactive effects that can marginalize the capacity. The 3D cross-linkage connectivity between the binder and the alloying anode material can highly ameliorate adhesion in electrode components, involving greater interaction with the metallic current collector to ensure high electrical conductivity and integrity. Feng *et al.* have reported that their Sb@C anode shows capacities of 553 and 435 mAh g⁻¹ over 50 cycles at 50 mA g⁻¹ using sodium alginate and PVDF binders, respectively^[257].

Performance influence of binder modifications has very recently been detailed for alloy-type SIB anodes by Yao *et al.* in a comprehensive study focusing on the cross-linking effect of glycerin (GLY) on poly(acrylic acid) (PAA) binders^[72]. They also optimized cross-linking conditions, particularly the cross-linking temperature. They tested the cross-linking influence on micro-sized Sn, Bi, and Sb electrodes. The cross-linking not only enhanced mechanical properties, but also promoted electrolyte diffusion and wettability and lessened the electrode presodiation step. The cross-linked binder in μ -Sn anodes furnished a high capacity of 668.5 mAh g⁻¹ at 2 A g⁻¹ after cycling 500 times. Afterward, the capacity dropped to 457.8 mAh g⁻¹ with extended cycling of 2,000 times. Rendering to the electrolyte's effective percolation, an initial CE of just above 90% was obtained with a final capacity retention of 68.5%. In comparison, electrodes fabricated with the same μ -Sn but with different binders, such as PVDF or PAA, showed inferior performances. Thick electrodes with high mass loading have also been fabricated to further broaden the scope of the cross-linking effect. It has been successfully demonstrated that electrodes with mass loading from 1.6 to 8.3 mg cm⁻² all show linear increase in areal capacity from 1.3 to 6.8 mAh cm⁻². Another conclusive evidence of an optimized multifunctional binder has been presented by Patra *et al.*^[258]. SnO₂@CMK (C mesostructured by KAIST) conversion-alloying SIB anodes fabricated using different binders such as PVDF, sodium carboxymethylcellulose (NaCMC), sodium polyacrylate (NaPAA), and NaCMC/NaPAA have shown capacities of 460, 530, 560, and 650 mAh g⁻¹, respectively, under a current of 100 mA g⁻¹ over 300 cycles. The uplifted performance of NaCMC/NaPAA mixed binder effectively increased the strength, binding characteristics, and volumetric forbearance during expansion/contraction with excellent wettability, all coherently stabilized the SEI and capacity. These results highlight the imperative role of binders in screening and optimizing performances of next-generation SIBs.

Some recent studies have focused on binder-free electrodes where C-fiber often hosts the active material assembly either in the form of a support on which the active material is grown or embedded inside the C matrix. Another approach is to use C foam as a binder-free support^[120,259]. A binder-free SIB alloying anode constructed from MOF-derived C and Bi nanodots has shown a higher performance than the bare electrode^[260]. The electrode sustained a high ICE and maintained a capacity of 550 mAh g⁻¹ at 100 mA g⁻¹, coupled with a specific rate capacity of 110 mAh g⁻¹ at 2.4 A g⁻¹. The excellent volume buffering with efficient diffusion kinetics of Na⁺ ensured resilience with SIB potential. Another binder-free Sb/NiSb alloying anode has been tested. It achieved a capacity of 521 mAh g⁻¹ over 100 cycles at 200 mA g⁻¹, with an excellent rate performance and a high ICE^[117].

Reducing voltage hysteresis

Many recent efforts in reducing voltage hysteresis have shown improved cyclic performance. A recent attempt has been made to identify the role of phase transformations and hysteresis using Na-Sb and Na-P systems with electrode materials having stable phases to minimize polarization effects and have better cyclability^[261]. Similarly, the Sb₈Bi₁ alloy anode in SIBs has been recently selected for delivering a high ICE of 87.1% at 0.1 A g⁻¹. The electrode exhibited low polarization effects. It could furnish a high capacity of 625 mAh g⁻¹ after 100 cycles at 1 A g⁻¹^[42]. Selecting suitable interfaces can mitigate the voltage hysteresis issue, as recently reported in Co-Sn alloy, where dually functioning active/inactive phases can reduce dendrite growth in sodium metal batteries^[262]. Although roles of structural modifications, electrolyte

additives, and counter electrodes have been highlighted in recent studies to diminish voltage hysteresis, the detailed significant role contributing to hysteresis needs to be mechanistically probed for each material in a specific set of cell assembly and operating conditions^[41,263,264].

Structural defects and surface engineering

One of the essential and perhaps overemphasized strategies of tuning the performance of the battery materials is by performing structural modifications that often can achieve suitably sustaining performances. Various methodologies have been reported, including nanosizing, designing functional surfaces by introducing functionalities, coatings, elemental doping, multicomponent design, and compositing to construct 1D, 2D, and 3D structures to introduce interconnected channels, pores, and other short pathways to achieve high conductivity with efficient ion/electron transfer and manage volume expansions. Although many of these optimizations for high-capacity SIB electrodes are difficult to achieve without compromising on one or more performance aspects, they always show some negative traits. For example, nanosized alloy particles have a high surface area that can effectively shuttle more Na^+ along with high electrode/electrolyte interfacial contacts. However, when the surface area is beyond a certain size, it can enhance mechanical cracking of electrode materials similar to in alloying nanostructures, which bear high volume expansions during charge/discharge. An exceptionally high surface area also offers highly reactive surfaces for undesired reaction pathways. Alongside smaller nanoparticles, incomplete alloying can occur because smaller equilibrium ion concentrations can lessen the overall capacity. Many nano morphological optimizations, including porous architectures, nanorods, nanowires, nanosheets, hollow structures, and yolk-shell morphologies, have effectively yielded high capacity and managed other shortcomings in alloying SIBs^[24,228,230,265].

Structural resilience of nanostructured alloying anodes during the charge process is critically important as it is directly linked to the performance. However, in some instances, it has been reported that structural evolutions also have a cohesive impact on capacity retention, as crystalline to amorphous phase conversions are often detected during *in-situ* characterization^[81,173]. Similarly, dual active/inactive phases have also been shown to take part alternatively during charge/discharge phenomena. Versatile and multi-modal stability is often ensured by introducing some carbonaceous material such as CNTs, graphene, N-doped C, C NF, hard C, and others in bulk or using some coating methodology. Besides improving conductivity and Na^+ transport kinetics, it offers functional surfaces for sustaining the capacity. Nanosizing effects have also been imparted in C-derived alloy anodes. Volume buffering effects are primarily of interest when carbonaceous hybrid alloying anodes with low ICE are targeted^[201,228,266].

Various intermetallic alloys have been tuned with carbonaceous materials for stable SIB anode performance. For example, when ultrasmall 3D-SnSb/NPC (nanoporous carbon) was utilized as an SIB anode, it furnished an optimal capacity of 266.6 mAh g⁻¹ over 15,000 cycles at 2 A g⁻¹ with rate performance of 566.1 mAh g⁻¹ at 10 A g⁻¹. Thus, it is highly appreciated among various SnSb C-coated materials reported^[267]. Other than the superior ultrasmall-coated nanoparticle assembly, multiple optimizations were applied, including electrolyte and binder modifications, all of which improved the ICE and long-term performance of the derived SIB anode.

A recent exciting electrode design has been presented by Kang *et al.*^[268]. They compared anode performances of synthesized AlSb, AlSb@C, and oxide terminated Al/AlSb/Sb_xO_y multicomponent anode with N-doped C. The superb oxide terminated array (Al/AlSb/Sb_xO_y) enabled the anode to deliver a stable 258 mAh g⁻¹ capacity at 10 C, much higher than previously reported micro-sized Sb SIB anodes. The specific nanoparticle structural assembly helps buffering volumetric strains and stable SEI creation, ensuring

longevity of the anode in half and full-cell operations.

An intermetallic Sn-Bi SIB anode has been recently proposed, showing stable and sustaining capacity as an SIB anode. The optimized SnBi composition showed a capacity of 508 mAh g⁻¹ in the first cycle and a capacity of 420 mAh g⁻¹ at 1 C after cycling 200 times^[269]. The synchrotron operando XRD showed the origin of different Sn and Bi intermetallic alloyed compositions during (dis)charging phases. At different electrochemical potentials, Sn and Bi particles in the intermetallic get sodiated to various levels. When one phase is active (sodiated), the other is dormant. In this way, the system is buffered to manage volumetric stresses. An anode-less configuration has recently been opted to utilize the Bi array deposited onto a copper foil to form Cu@Bi alloy^[270]. The fabricated material was tested in both half-cell and full-cell configurations after initial activation. The full cell comprising the Cu@Bi anode and NVP as cathode delivered a capacity of 95.6 mAh g⁻¹ over 80 cycles. A binary melt-spun alloy Fe-As has recently been tested as an SIB anode by Patel *et al.*^[271]. This anode delivered an ultrahigh and stable capacity of 965 mAh g⁻¹ at 50 mA g⁻¹ over 400 cycles. Additionally, it demonstrated an excellent sodiation rate performance of 668 mAh g⁻¹ at 2 A g⁻¹, surpassing most of the common SIB anodes. Beyond that, melt-spun fibers showed 770 mAh g⁻¹ of sodiation capacity after 200 cycles at 50 mA g⁻¹ (with over 97% CE). Detailed *ex-situ* XRD highlighted the compositional and phase transformations, confirming the formation of Na₃As during sodiation and the appearance of an iron-rich phase. This study highlighted the excellent potential of intermetallic alloy materials for being opted as commercial anodes for SIBs. Similarly, Sb-Zn electrodeposited intermetallic alloy showed superior Na⁺ storage capacity as a binder-free anode in SIBs, whereby different Sb and Zn alloying with sodium was traced during the charge/discharge process^[120].

Recently, a hybrid SIB anode composed of FeSb₂S₄/Sb/rGO that offers a highly stable capacity of 366.1 mAh g⁻¹ over 100 cycles at 0.1 A g⁻¹ has been reported^[115]. The material showed quite durable performance at higher current densities and offered a capacity of 252.7 mAh g⁻¹ at 10 A g⁻¹ over 100 cycles. The reaction mechanism involved dual alloying/dealloying followed by a conversion reaction with good reversibility, which could mitigate challenges faced by SIB anodes. Shen *et al.* have newly proposed a Sb-Co-P alloying anode showing superior SIB anode performance^[164]. Among those with the best compositions, Sb_{21.0}Co_{46.9}P_{32.1} delivered a capacity of 586.3 mAh g⁻¹ after 100 cycles at a current density of 100 mA g⁻¹ (CE: 77.6%). *In-situ* XRD demonstrated changes in peak intensities and the formation of Na₃P and Na₃Sb with Co nanoparticles. A nanoalloy of Sn-Ni doped with N-doped C presented an efficient 3D structure with a pomegranate-like morphology. It has been tested for an SIB anode both in half-cell and full-cell configuration^[272]. The SIB had a half-cell capacity of 332.1 mAh g⁻¹ over 100 cycles at 0.2 A g⁻¹ and a full-cell capacity of 112.5 mAh g⁻¹ at 0.1 A g⁻¹ over 60 cycles. The intact morphology with N-doped C improved the electronic conductivity with multiple ion transport pathways for effective ion shuttling.

In fact, a unique strategy has recently been employed by Li *et al.* to fabricate a modified anode material^[273]. They incorporated Sn into copper sulfide and then partially substituted Sn with Zn, which garnered a sodium uptake capability of the electrode with stable performance and fast charging behavior. The Sn-Zn-based copper sulfide maintained a capacity of 560 mAh g⁻¹ at 0.2 A g⁻¹ with a retention capacity of 100% for 80 K cycles. The material furnished a highly fast charging of 4 s per charge with an input of 190 mAh g⁻¹. A freshly developed mesoporous Sn/SnO₂-Ni@C composited alloy has shown marked performance as an SIB anode. The composite furnished a stable capacity of 342.6 mAh g⁻¹ at 0.2 A g⁻¹ after 200 cycles while the anode delivered a capacity of 219.3 mAh g⁻¹ at 1.0 A g⁻¹ when cycled 1,000 times^[274]. The excellent interplay between the Sn/SnO₂ and Ni has mitigated effects of volume expansion and capacity degradation. Another fascinating study has highlighted a 3D core-shell heterostructured SnO₂ coated with barium titanate (acting as core) and covered with phosphorous-doped C (BTO@SnO₂@P-C) [Figure 20A]^[206]. The unique selection

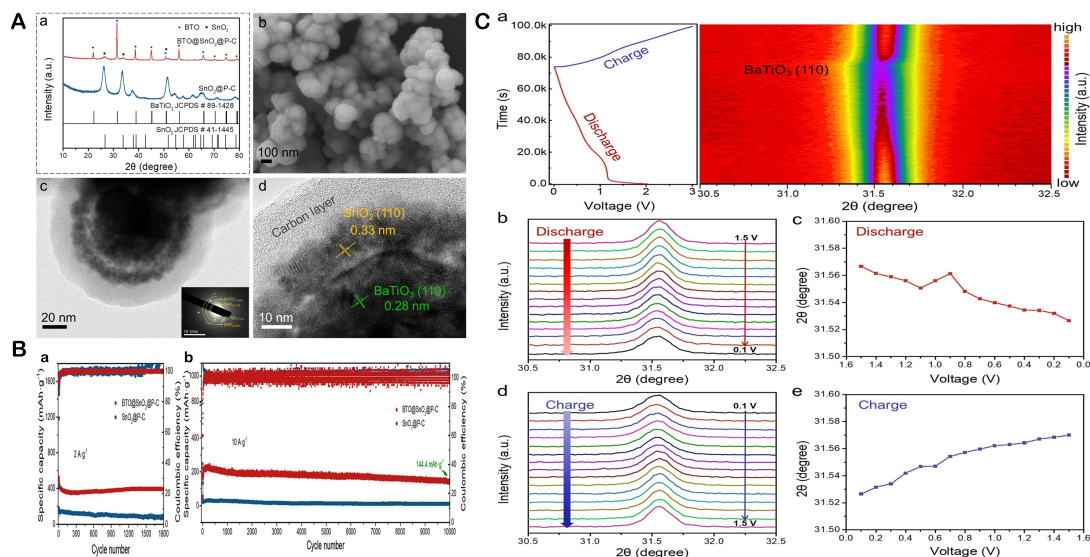


Figure 20. (A) (a) XRD pattern of BTO@SnO₂@P-C and SnO₂@P-C, (b) SEM image, (c) TEM with SAED pattern image (inset), and (d) HR-TEM image. (B) Long cycle performance of BTO@SnO₂@P-C at (a) 2 A g⁻¹ and (b) 10 A g⁻¹. (C) *In-situ* XRD analysis of BTO@SnO₂@P-C at the initial cycle: (a) Voltage-time curves at 0.1 A g⁻¹ (left) and BTO (110) plane contour pattern (right), (b) XRD profile of BTO (110) when discharged from 1.5 to 0.1 V, and (c) Corresponding voltage-2θ curves, (d) XRD profile of BTO (110) charged from 0.1 to 1.5 V, and (e) Corresponding voltage-2θ curves. Reproduced with permission from [206]. Copyright © 2022 Elsevier.

provided the built-in electric field effect generated by the BTO layer due to ferroelectric polarization, further augmented by the piezoelectric effect that could increase due to volume expansion during alloying of SnO₂ in the core-shell structure. These synchronous effects highly improved the performance as an SIB anode with an awe-inspiring reversible capacity of 144.4 mAh g⁻¹ over 10,000 cycles at 10 A g⁻¹ with extra fast charging (99% charged in 1 min), as shown in Figure 20B. Detailed *in-situ* XRD studies [Figure 20C] proved that the BTO (110) plane showed evident peak shifts during (dis)charging and participated in the stability of the anode.

A rGO composite of Sn/Sb as an SIB anode delivered a capacity of 320 mAh g⁻¹ over 300 cycles at 500 mAh g⁻¹. However, upon continued cycling 600 times, the capacity continuously faded to 175 mAh g⁻¹ [275]. Multiple reports have realized that the potential of Sb₂SnO₅ (SSO) can be at par with other commercial anodes because of its high theoretical capacity of 1,195 mAh g⁻¹. Main issues that need to be addressed are its slow ion transfer kinetics and poor electronic conductivity. Chen *et al.* have recently developed an electrospun PCNF matrix embedding SSO nanoparticles along with a Sn/Sb array [276]. The hybrid can cope with the above issues. In addition, it can inhibit side reactions, offer volume buffering, and expand grain boundaries with more active sites for Na⁺ storage. The material showed a capacity retention of 440 mAh g⁻¹ over 450 cycles at 0.5 C while sustaining a rate capability of 281.8 mAh g⁻¹ at 500 mA g⁻¹. In another recent report, Sn and Sb oxides composited within porous carbon wires showed decent Na⁺ storage capacity as an anode. The SSO-based composite delivered a sustaining capacity of 448 mAh g⁻¹ at 50 mA g⁻¹ after 150 cycles [277]. At a high current density of 3 A g⁻¹, the composited SSO anode showed a capacity of 427 mAh g⁻¹ after 200 cycles. The performance was attributed to the hybrid structural design in which the porous C wires encompassed the metallic Sn, Sb, and the oxide SSO state that could excellently bear the volumetric stress. The unique morphology provides abundant diffusion pathways in the form of channel-like arrays that make ionic diffusion faster. It also bears a high number of active sites that, along with well-distributed metallic and oxide domains, can enhance the conductivity and improve the kinetics of the charge transfer process.

Bhar *et al.* have recently reported a freestanding carbon fiber-based composite electrode composed of Sn-rich Ni-Sn/CF with leaf-like morphology^[278]. The electrode was tested as an SIB anode without a metallic current collector. It delivered a capacity of 220 mAh g⁻¹ after 300 cycles at 150 mAh g⁻¹. The unique framework was able to buffer volume expansion/contraction changes accompanying the charge/discharge process. This is appealing as it can avoid the use of a current collector that can lower the cost. A CuS/Sn₂Sb₃ hybrid alloying-based anode that furnishes an initial discharge capacity of 659 mAh g⁻¹ in the initial cycle at 0.1 A g⁻¹ while the composite sustains almost total (266 mAh g⁻¹) capacity in 100 cycles has been proposed^[279].

Recently, Sb porous hollow microspheres presented by Hou *et al.* have shown a good SIB alloying anode potential, delivering an ICE of 64.6% (a charging capacity of 634.6 mAh g⁻¹ at 100 mA g⁻¹) with a reasonable rate performance of about 313 mAh g⁻¹ over 100 cycles at 3,200 mA g⁻¹^[280]. Sn nanorods modified by N-doped C proposed by Yang *et al.* have been presented as SIB anodes that could deliver stable extra-long cycle performance with a wide temperature window (-20-50 °C)^[75]. Performances of the anode in various electrolytes and full-cell configurations have been presented along with optimized morphology. In DEGDM-based electrolytes, an ICE of 78.4% has been achieved with a rate performance as high as 437 mAh g⁻¹ at 5.0 A g⁻¹. Element doping is essential for attenuating the crystal structure, band gap, and oxidation states and creating vacancies. Thus, an overall increase of conductive properties can enhance the SIB alloy behavior for higher Na⁺ uptake.

Another common strategy is to create defects and oxygen vacancies with potential to enhance the intrinsic electronic conductivity and sodiation potential of a material^[61,229,281,282]. Amorphous-crystalline defect-bearing hetero-conjunctions formed between the amorphous SeP and crystalline graphene conductive framework have been proposed to facilitate the SIB performance of SeP@HCG (high conductive crystalline graphene)^[283]. The material effectively sodiated into an amorphous Na_xSeP phase, leading to nanocrystalline Na₂Se and Na₃P to attain a high capacity of 855 mAh g⁻¹ at 0.2 A g⁻¹ with an extended cyclability. After 500 cycles, it maintained a capacity of 732 mAh g⁻¹.

Recently, Liu *et al.* have reported a high-capacity 3D Bi-derived electrode that undergoes a dual alloying-stripping mechanism, unlike conventional alloying anodes^[284]. The bulk Bi material was converted to a 3D framework after activation and alloying, followed by subsequent plating, resulting in a sodiophilic Na@3D Na₃Bi framework that dually exploited SIBs and sodium-metal batteries (SMBs)'s characteristic ion exchange process. Above all, the ultimate capacity delivered by the anode was about 7.7 times higher than that of the alloying Bi anode, retaining a capacity of 2,000 mAh g⁻¹ for 800 h at a current density of 1 A g⁻¹. The hybrid 3D-designed anode could shuttle Na⁺ for alloying in combination with Na⁺ plating in the inner space of the Na₃Bi network, which suppressed dendrite formation, unlike in SNBs. Similarly, MoS₂/SnS showed a superior capacity retention behavior to store 634 mA g⁻¹ after 100 cycles at 2 A g⁻¹. It also sustained a capacity of 745 mAh g⁻¹ at 10 A g⁻¹ during rate capacity cycling^[285].

Suitable cathode materials

There are a variety of cathode materials in SIBs, including layered sodium transition metal oxide-based materials, polyanionic compounds (sulfate, oxalate, phosphates, *etc.*), Prussian blue analogs, and others^[238,286,287]. Although many of these cathodes have demonstrated their commercial viability, such as oxides, Prussian blue, Prussian white analogs, and Na₃V₂(PO₄)₂F₃ (NVPF), unfortunately, all of them are coupled with hard carbon anode materials without any major research breakthrough using alloying-based anodes^[238,287]. Noteworthy, each category poses specific shortfalls that need to be overcome. For example, oxide-based materials always have stability issues despite their high capacity. Polyanionic cathodes have a

poor capacity and low electronic conductivity known to hamper their utilization. Prussian blue analogs (PBAs) suffer from lower tap density and the presence of water of crystallization in their structures known to pose safety threats and thermal runaway issues. The most critical challenge for cell SIBs is the choice of suitable anodes with a matching high capacity and stability cathode material that could offer a high voltage. The potential of composited cathodes can also improve the overall performance of SIBs. This must be considered for alloying-based anode counterparts^[59,288]. Vast material, structural, and compositional options for alloying anodes need immense experimental and theoretical screening using the latest machine-learning tools to determine their compatibility with commercially successful cathodes to achieve high-performing SIB cells ultimately.

Other optimization parameters

Alloying SIB anodes have been modified to entrap more (de)sodiation capacity using various strategies including presodiation, dealloying, and so on. The presodiation strategy offers an excellent solution to complement the Na⁺ concentration consumed and depleted in the SEI formation and side reactions. Presodiation at a certain level in both anode and cathodes is known to augment the SIB performance. Some recent studies have highlighted its importance^[289,290]. Presodiation must be optimized to maximize benefits, as in the Sn-C composite anode presented previously. The effectiveness of presodiation has been evident. An optimized presodiated anode can deliver a steady capacity of 130 mAh g⁻¹ without capacity losses for 60 cycles^[291]. In fact, a presodiated Sb anode presented by Liu *et al.* can improve ICE from 75% to 100%. After 300 cycles, this presodiated anode maintained 85% of its capacity^[292]. Presodiation can be done by adding sodiating agents with many standard methodologies. It has the potential to get the optimal design architecture. Recently, the presodiation strategy has been employed by Shen *et al.* for Sn-based anodes^[73]. They took a commercially available Sn powder and sodiating agents, such as sodium biphenyl, and so on, and achieved a marvelous capacity of 602 mAh g⁻¹ after 7,500 cycles. This Sn-based anode kept 71% of its capacity in the full cell configuration. They extended their presodiation methodology for synthesizing other porous alloying anodes such as Sb and Bi.

Various researchers have also adopted dealloying to achieve the optimized morphology for SIB alloying electrode materials, although dealloying has not been explored extensively. In this strategy, some element (sacrificial element) is often selectively removed to achieve the desired 3D porous/hollow/network structure. Some reports have claimed to attain superior and stable capacities using a dealloying methodology. For example, Sb₂O₃@Sb proposed by Ma *et al.* could sustain 200 mAh g⁻¹ at a high current rate of 29.7 A g⁻¹ in rate capacity^[125]. It showed 99.8% cyclic capacity retention. Recently, a novel approach to improve the performance of alloying SIB anode has been highlighted. In this approach, K⁺ incorporated into the electrolyte can highly improve the performance of Sn alloying anode, yielding an energy of 565 mAh g⁻¹ over 3,000 cycles at 2 A g⁻¹^[71]. Dimensional structure and electrode formulations can also be used for achieving the optimized SIB performance using (a) tin; (b) antimony; (c) phosphorus; (d) germanium; (e) silicon; and (f) bismuth-based anode materials. These are provided in Table 3.

SUMMARY AND FUTURE PROSPECTIVE

Recent trends in synthetic methodologies for robust structural design, material selection, and analysis tools focusing on intermediate evolutions during (de)sodiation were highlighted in detail from a capacity-stability aspect for SIB alloying anode materials. Moreover, challenges faced by the current generation of alloying materials in terms of mechano-electrochemical changes incurred during cycling and strategies diversely employed to overcome those challenges were summarized. Detailed remediation strategies diversely employed to overcome the limitations were also highlighted. Conclusively, more focus on the latest mechanistic-driven characterization tools is obligatory for the upcoming high energy-density SIBs based on alloying anodes.

Table 3. Effects of dimensional structure and electrode formulations on optimized SIB performance using alloy-based anodes

| Dimensional structure | Materials | Synthesis methods | Electrolyte system | Electrode composition (%) | ICE (%) | Specific capacity (mAh g ⁻¹) | Current density (A g ⁻¹) | Cycle number | Rate Performance (mAh g ⁻¹) | Current density (A g ⁻¹) | Ref. |
|--|--|---|---|---|---------|--|--------------------------------------|--------------|---|--------------------------------------|-------|
| Tin-based anode materials | | | | | | | | | | | |
| 0D | Sn@CFC | Electrospinning method | 1M NaClO ₄ in EC/DMC with 5% FEC | Freestanding | 42.3 | 255 | 0.05 | 200 | 100 | 1 | [293] |
| | Porous carbon nanocages@Sn | Template-assisted CVD and in-situ reduction | 1M NaClO ₄ in EC/PC with 5% FEC | AM:carbon black:PVDF (80:10:10) | 73 | 202 | 1.28 | 550 | 188 | 2.56 | [294] |
| | Sn nanoparticles@C | Aerosol spray pyrolysis method | 1M NaClO ₄ in EC/DEC | AM:super P carbon:CMC (70:15:15) | 67 | 415 | 1 | 500 | 349 | 4 | [295] |
| 1D | Sn nanofibers | Electrodeposition | 1M NaClO ₄ in PC with 2% FEC | - | 68 | 776 | 0.1 C | 100 | -260 | 5 C | [296] |
| | Sn@N-doped carbon | Annealing | 1M NaPF ₆ in DME | AM:acetylene black:sodium carboxymethylcellulose (80:10:10) | 78.4 | 347 | 5 | 10,000 | 437 | 5 | [75] |
| 3D | Microsized gray-Sn | Commercial | 1M NaPF ₆ in DGM | Am:acetylene black:CMC (70:20:10) | 80 | 451 | 2 | 3,500 | 464 | 4 | [297] |
| | Porous Sn | Replacement reaction | 1M NaPF ₆ in DME | AM:super P carbon:PVDF (70:20:10) | - | 660 | 2.5 | 400 | 667.6 | 6.5 | [298] |
| Antimony-based anode materials | | | | | | | | | | | |
| 0D | Sb@NS-3DPC | Pyrolysis | 1M NaClO ₄ in PC with 10% FEC | AM:conductive carbon:CMC (70:15:15) | 61.1 | 259 | 10 | 20,000 | 283.8 | 10 | [299] |
| 1D | SbSn nanoarrays | Electro deposition and annealing | 1M NaPF ₆ in DME | AM: carbon black:PVDF (80:10:10) | 83 | 511 | 2 C | 800 | 521 | 5 C | [300] |
| | Bi _{0.75} Sb _{0.25} pyramid arrays | Electro deposition and annealing | 1M NaPF ₆ in DME | AM:carbon black:PVDF (80:10:10) | 86 | 284 | 0.5 | 2,000 | 335 | 2.5 | [301] |
| 2D | antimonene/C | Liquid-phase exfoliation | 1M NaPF ₆ in EC/DMC with 5% FEC | - | 71.2 | 451.3 | 0.2 | 150 | 334.5 | /5 | [302] |
| | few-layer antimonene | Liquid-phase exfoliation | 1M NaClO ₄ in EC/DEC with 5% FEC | AM: carbon black:CMC (65:20:15) | 64.7 | 620 | 0.5 C | 150 | 429 | 5 C | [303] |
| 3D | Nanoporous Bi ₂ Sb ₆ | Dealloying | 1M NaPF ₆ in PC with 5% FEC | AM:acetylene black -super P:CMC (60:25:15) | 69.8 | 258 | 0.2 | 2,000 | 304.2/15 | | [304] |
| Phosphorous-based anode materials | | | | | | | | | | | |
| 0D | P/TiN | Mechanical milling method | 1M NaClO ₄ in EC/DEC with 5% | AM:super-P carbon:CMC (80:10:10) | 86.8 | 91.3 | 0.2 | 300 | 339 | 20 | [305] |

| | | | | | | | | | | | | |
|-------------------------------|---|--|--|--|------|---------|------|--------|-------|------|-----------------------|--|
| | | | FEC | | | | | | | | | |
| | Red P@ nitrogen-doped porous carbon tubes | Vaporization condensation method | 1M NaClO ₄ in EC/DMC with 5% FEC | Freestanding electrode | - | 1,157 | 2 | 100 | 572 | 10 | [306] | |
| | Hierarchical porous carbon nanospheres/P | Vaporization condensation process | 1M NaClO ₄ in EC/DEC | AM:acetylene black:PVDF (80:10:10) | 75.1 | 861.8 | 5 | 1,000 | 831.1 | 10 | [307] | |
| | red@black P/N-graphene | Solvothermal treatment | 1M NaClO ₄ in EC/DMC with 5% FEC | AM:Carbon black:PVDF (80:10:10) | 65.3 | 465.5 | 10 | 1,200 | 521.3 | 10 | [216] | |
| | P@CNTs backbone mesoporous carbon | Vaporization condensation conversion | 1M NaClO ₄ in EC/DEC with 5% FEC | AM:C-black:Na-CMC, (75:10:15) | 69.8 | 580 | 2.5 | 800 | 430 | 8 | [308] | |
| | Nanoscale red P/rGO | Phosphorus-amine-based method | 1M NaClO ₄ in EC/DEC with 10% FEC | AM:super P acetylene black:PVDF (70:20:10) | 61.2 | 390 | 5 | 5,000 | 718 | 5 | [154] | |
| 1D | Se-induced fibrous nano red P | Selenium-induced method | 1M NaClO ₄ in EC/PC with 5% FEC | - | 89.7 | 1,785 | 1C | 2,800 | 1,190 | 25 C | [309] | |
| | Red P@carbon nanofiber | Vaporization condensation method | 1M NaPF ₆ in EC/DEC | Freestanding films | - | 1,850 | 0.1 | 500 | - | | [157] | |
| 2D | Phosphorene/Ti ₃ C ₂ T _x MXene | Self-assembly | 1M NaClO ₄ in EC/PC | AM:carbon black:CMC (70:20:10) | 63.1 | 340 | 1 | 1,000 | 193 | 5 | [310] | |
| | phosphorene graphene | Self-assembly | 1M NaPF ₆ in EC/DEC with 10% FEC | - | ~80 | 2,440 | 0.05 | 100 | - | | [311] | |
| | phosphorene graphene | Electrochemically exfoliated and solution method | 1M NaClO ₄ in PC with 5% FEC | AM:super P:CMC (70:15:15) | 80.6 | 1,582.6 | 1 | 200 | 1,499 | 5 | [312] | |
| | Black P/graphene | Pressure synthesis | 1M NaClO ₄ in DMC with 10% FEC | Freestanding films | 89.5 | 1,250 | 1 | 500 | 720.8 | 40 | [313] | |
| 3D | Sb7-RP63/C30 | High-energy ball milling process | 1M NaPF ₆ in PC with 2% FEC | AM:super-P:sodium alginate (70:15:15) | 88 | 2,356 | C/3 | 70 | 1,779 | 2 C | [215] | |
| | Red P@Carbon nanocages | Evacuation-filling process | 1M NaClO ₄ in EC/DEC with 10% FEC | AM:carbon black:PVDF (70:20:10) | - | 1363 | 0.1 | 150 | 750 | 5 | [214] | |
| | Nanoporous red P@rGO | Boiling | 1M NaClO ₄ in PC with 5% FEC | AM:super P:CMC (70:15:15) | 78.5 | 1,250 | 0.17 | 150 | 657 | 3.47 | [150] | |
| Bismuth-based anode materials | | | | | | | | | | | | |
| 0D | Bi@N-doped carbon nanospheres | Annealing | 1M NaPF ₆ in DME | AM:super P:PVDF (70:20:10) | 36.5 | 235 | 10 | 2,000 | 152 | 100 | [314] | |
| | Bismuth Nanoparticle@Carbon | Annealing | 1M NaPF ₆ in DME | AM:Super P:PVDF (80:10:10) | 50.3 | 265 | 8 | 30,000 | 232 | 60 | [315] | |

| | | | | | | | | | | | |
|-----------|----------------------------|--|---------------------------------|---|------|-------|-----|--------|-------|-----|-----------------------|
| Composite | | | | | | | | | | | |
| 1D | Bi nanowires@graphene film | Vacuum filtration assembly | 1M NaPF ₆ in DME | - | 82.7 | 276 | 1 | 1,000 | 295 | 5 | [316] |
| | Bi nanotubes | Iodine-ion-assisted galvanic replacement | 1M NaPF ₆ in DME | AM:carbon black:CMC (90:5:5) | 69.2 | 355 | 20 | 15,000 | 319 | 150 | [204] |
| 2D | Bi@N-doped carbon | Solvothermal and carbonization | 1M NaPF ₆ in DME | AM:carbon black:PVDF (80:10:10) | 85.1 | -325 | 10 | 5,000 | 341.5 | 10 | [223] |
| 3D | Porous Bi/C | Annealing | 1M NaPF ₆ in DME | AM:carbon black: sodium alginate (70:15:15) | 95.2 | 178 | 50 | 20,000 | 101 | 72 | [317] |
| | LC-bi composite | Calcination | 1M NaPF ₆ in DME | AM:super P:PVDF (80:10:10) | 53.4 | 225.6 | 1 | 2,600 | 236.1 | 100 | [201] |
| | 3D porous Bi | Solution reduction | 1M NaPF ₆ in DME | AM:acetylene black:PVDF (70:20:10) | 65.9 | 374 | 10 | 3,000 | 354 | 60 | [318] |
| | Bulk Bi | Commercial | 1M NaPF ₆ in diglyme | AM:super P:PVDF (80:10:10) | 94.8 | 389 | 0.4 | 2,000 | 356 | 2 | [319] |

To ascertain capabilities of alloying anodes for next-generation SIBs, many modifications are necessary. Optimized alloying anode's structure, composition, matching cathodes, binders, and electrolyte systems need extensive sorting. Structural modification is a prerequisite to accommodate some alloying anodes' volume changes, voltage hysteresis, and low electronic conductivity. However, effective modulation from the commercial perspective may take years to see SIBs on the energy horizon. Without deep tunneling into mechanistic paths and limitations, it seems unlikely.

Nanosized composite/alloy hybrid design with porous 3D electronically conductive materials must focus on alloy compositions for highly stable electrode configurations. Similarly, many recent studies have extensively validated the superiority of ether-based solvent systems as they offer stable and low energy solvation structuring with Na⁺, superior wettability, electrolyte penetration, and fast and reversible (de)sedation kinetics, ensuring thin and stable SEI. These ether-based electrolyte systems should be widely explored for various SIB alloying anodes along with recent approaches using binder-free and anodeless configurations and shifting towards solid electrolytes with potential to direct the future of alloying anodes.

Diverse formulations and materials choices in alloying SIB anodes have further been diversified with nanostructuring, doping, vacancy creation, alloying, and compositing with multicomponents, enhancing possibilities and prospects for high-stability electrode materials. In this regard, hard carbon materials with already proven promise as SIB anodes need more attention when compositing with alloying materials. A straightforward approach to optimize and validate an alloying-based electrode's performance from the bulk of theoretical and experimental literature reports is to use machine learning tools and theoretical models to obtain more efficient methodologies and material combinations, thereby reducing weary efforts in random material/methodology selection.

Other than morphology, material selection, and electrolyte systems, many other recently introduced strategies such as ion incorporation including (K^+), sacrificial cathode additives, and presodiation of anodes have a good impact on capacity enhancement. However, current SIBs have much less energy density than prevailing LIBs. Most of the capacity destructive processes arise in the initial cycle, causing a low ICE, particularly in the case with alloying SIB anodes. For alloying anodes to ensure high ICE and stable long-term performance, remodeling of different constituents, especially the electrolyte system and its compatibility with the nanostructured alloying material, needs more focus. In this regard, the formation process of SEI needs to be closely observed to ensure thin, stable, non-destructive SEI that can further assist in fast kinetics.

Although promising results of alloying SIB anodes have been reported, giving some glimpse into commercial-scale achievement, they are usually limited to lab-scale breakthroughs. To sort the right combination of alloying materials and other constituents, the fundamental aspect of capacity fading must first be sorted. Notably, a complete mechanistic understanding of phases evolved during (de)sodiation needs operando characterization tools that can trace the formation and reconversion of species during continuous cycling. Unfortunately, most reports lack this vital information. The multistep alloying and alloying-conversion mechanism must be fully tracked using different operando tools. Mainly, *in-situ* TEM analysis is capable of giving atomistic details using HAADF-STEM (with corresponding SAED and FFT patterns) and EDS mapping that can ensure intermediate species while the charging-discharging proceeds. However, the current level of *in-situ* TEM has certain limitations, such as using the Na_2O electrolyte in a nano-battery setup, which could not match or withstand the same as real-world batteries. Moreover, *in-situ* TEM of the nano-battery could not offer evidence of SEI formation. Nonetheless, coupling these *in-situ* findings with other *in-situ* and theoretical studies can decipher the mechanism involved in (de)sodiation, capacity fading, and these anode materials to a greater extent. In this regard, the continually varying interphase behavior can be tracked using *in-situ* XRD under (dis)charging conditions. *Ex-situ* XRD, *in-situ* Raman, impedance, and the less employed Mossbauer, solid-state NMR spectroscopic evidence can sometimes validate the detailed mechanism for the capacity failure. However, these methods are not frequently adapted in most of the ongoing research. Operando synchrotron XPS studies are also capable of tracking solid-liquid interphases and the exact mechanism of SEI constitution in different alloying-based SIB cells that can help mitigate randomized search going on for efficient alloying anodes in SIB. Various other non-destructive synchrotron operando imaging techniques that use X-ray photons instead of e^- beam for elemental, spatial, and local electronic structures probing with the most excellent sensitivity have been reported. Remarkably, the power of tomographic techniques has allowed scanning and 3D real imaging with many highly selective techniques such as scanning transmission X-ray microscopy, scanning transmission X-ray microscopy, micro X-ray fluorescence, and transmission X-ray tomography. When coupled with X-ray absorption, they can enable detailed structural evolutions, particularly for performing morpho-chemical analysis of SEI in unique and temporal domains^[320,321]. It is worth mentioning that the ultimate alloying anodes must provide wide temperature and voltage operative windows with simple and scalable synthetic procedures at a marginal cost with the least toxicity.

DECLARATIONS

Authors' contributions

Writing-original draft: Rehman Au, Saleem S

Data curation: Ali S

Investigation: Rehman Au, Abbas SM, Choi M

Visualization: Choi M

Project administration: Choi W

Availability of data and materials

Not applicable.

Financial support and sponsorship

This research was supported by the program through the National Research Foundation of Korea (NRF) funded by the Ministry of Science and ICT (No. RS-2024-00404414, Development of High Energy Density Core Materials and High-Efficiency Cell Technology for 220Wh/kg-Class Sodium-Ion Batteries). Additional support was provided by the Korea Institute for Advancement of Technology (KIAT) grant funded by the Korean Government (MOTIE) (P0012748, HRD Program for Industrial Innovation).

Conflicts of interest

All authors declared that there are no conflicts of interest

Ethical approval and consent to participate

Not applicable.

Consent for publication

Not applicable.

Copyright

© The Author(s) 2024.

REFERENCES

1. Berry C. The paradox of green growth: challenges and opportunities in decarbonizing the lithium-ion supply chain. In: Kalantzakos S, editor. Critical minerals, the climate crisis and the tech imperium. Cham: Springer Nature Switzerland; 2023. pp. 107-23. [DOI](#)
2. Uslu S, Piriñçi F. The impact of COVID-19 on global energy security and energy geopolitics. In: Akıllı E, Gunes B, editors. World politics in the age of uncertainty. Cham: Springer Nature Switzerland; 2023. pp. 219-33. [DOI](#)
3. Singh AN, Islam M, Meena A, et al. Unleashing the potential of sodium-ion batteries: current state and future directions for sustainable energy storage. *Adv Funct Mater* 2023;33:2304617. [DOI](#)
4. Zhou G, Chen H, Cui Y. Formulating energy density for designing practical lithium-sulfur batteries. *Nat Energy* 2022;7:312-9. [DOI](#)
5. Tian H, Li Z, Feng G, et al. Stable, high-performance, dendrite-free, seawater-based aqueous batteries. *Nat Commun* 2021;12:237. [DOI](#) [PubMed](#) [PMC](#)
6. Wang X, Tang S, Guo W, Fu Y, Manthiram A. Advances in multimetallic alloy-based anodes for alkali-ion and alkali-metal batteries. *Mater Today* 2021;50:259-75. [DOI](#)
7. Wang X, Zhang C, Sawczyk M, et al. Ultra-stable all-solid-state sodium metal batteries enabled by perfluoropolyether-based electrolytes. *Nat Mater* 2022;21:1057-65. [DOI](#)
8. Sun Q, Dai L, Luo T, Wang L, Liang F, Liu S. Recent advances in solid-state metal-air batteries. *Carbon Energy* 2023;5:e276. [DOI](#)
9. Zhang L, Feng R, Wang W, Yu G. Emerging chemistries and molecular designs for flow batteries. *Nat Rev Chem* 2022;6:524-43. [DOI](#)
10. Olabi AG, Abbas Q, Al Makky A, Abdelkareem MA. Supercapacitors as next generation energy storage devices: properties and applications. *Energy* 2022;248:123617. [DOI](#)
11. Liang Y, Yao Y. Designing modern aqueous batteries. *Nat Rev Mater* 2023;8:109-22. [DOI](#)
12. Dutta A, Mitra S, Basak M, Banerjee T. A comprehensive review on batteries and supercapacitors: development and challenges since their inception. *Energy Stor* 2023;5:e339. [DOI](#)
13. Hao H, Hutter T, Boyce BL, Watt J, Liu P, Mitlin D. Review of multifunctional separators: stabilizing the cathode and the anode for alkali (Li, Na, and K) metal-sulfur and selenium batteries. *Chem Rev* 2022;122:8053-125. [DOI](#)
14. Huang L, Lu T, Xu G, et al. Thermal runaway routes of large-format lithium-sulfur pouch cell batteries. *Joule* 2022;6:906-22. [DOI](#)
15. Hong X, Mei J, Wen L, et al. Nonlithium metal-sulfur batteries: steps toward a leap. *Adv Mater* 2019;31:e1802822. [DOI](#)
16. Yabuuchi N, Kubota K, Dahbi M, Komaba S. Research development on sodium-ion batteries. *Chem Rev* 2014;114:11636-82. [DOI](#) [PubMed](#)
17. Tan H, Chen D, Rui X, Yu Y. Peering into alloy anodes for sodium-ion batteries: current trends, challenges, and opportunities. *Adv*

- Funct Mater* 2019;29:1808745. DOI
18. Sadik-zada ER, Gatto A, Scharfenstein M. Sustainable management of lithium and green hydrogen and long-run perspectives of electromobility. *Technol Forecast Soc Change* 2023;186:121992. DOI
 19. Li X, Sengupta T, Si Mohammed K, Jamaani F. Forecasting the lithium mineral resources prices in China: evidence with facebook prophet (Fb-P) and artificial neural networks (ANN) methods. *Resour Policy* 2023;82:103580. DOI
 20. Frith JT, Lacey MJ, Ulissi U. A non-academic perspective on the future of lithium-based batteries. *Nat Commun* 2023;14:420. DOI PubMed PMC
 21. Vaalma C, Buchholz D, Weil M, Passerini S. A cost and resource analysis of sodium-ion batteries. *Nat Rev Mater* 2018;3:1-11. DOI
 22. Nayak PK, Yang L, Brehm W, Adelhelm P. From lithium-ion to sodium-ion batteries: advantages, challenges, and surprises. *Angew Chem Int Ed* 2018;57:102-20. DOI PubMed
 23. Zhao L, Hu Z, Lai W, et al. Hard carbon anodes: fundamental understanding and commercial perspectives for Na-ion batteries beyond Li-ion and K-ion counterparts. *Adv Energy Mater* 2021;11:2002704. DOI
 24. Song K, Liu C, Mi L, Chou S, Chen W, Shen C. Recent progress on the alloy-based anode for sodium-ion batteries and potassium-ion batteries. *Small* 2021;17:e1903194. DOI PubMed
 25. Luo W, Shen F, Bommier C, Zhu H, Ji X, Hu L. Na-ion battery anodes: materials and electrochemistry. *ACC Chem Res* 2016;49:231-40. DOI
 26. He H, Sun D, Tang Y, Wang H, Shao M. Understanding and improving the initial Coulombic efficiency of high-capacity anode materials for practical sodium ion batteries. *Energy Stor Mater* 2019;23:233-51. DOI
 27. Patrike A, Yadav P, Shelke V, Shelke M. Research progress and perspective on lithium/sodium metal anodes for next-generation rechargeable batteries. *ChemSusChem* 2022;15:e202200504. DOI PubMed
 28. Chen J, Adit G, Li L, Zhang Y, Chua DHC, Lee PS. Optimization strategies toward functional sodium-ion batteries. *Energy Environ Mater* 2023;6:e12633. DOI
 29. Qiao S, Zhou Q, Ma M, Liu HK, Dou SX, Chong S. Advanced anode materials for rechargeable sodium-ion batteries. *ACS Nano* 2023;17:11220-52. DOI PubMed
 30. Sarkar S, Peter SC. An overview on Sb-based intermetallics and alloys for sodium-ion batteries: trends, challenges and future prospects from material synthesis to battery performance. *J Mater Chem A* 2021;9:5164-96. DOI
 31. Xu G, Amine R, Abouimrane A, et al. Challenges in developing electrodes, electrolytes, and diagnostics tools to understand and advance sodium-ion batteries. *Adv Energy Mater* 2018;8:1702403. DOI
 32. Hou Z, Lei D, Jiang M, et al. Biomass-derived hard carbon with interlayer spacing optimization toward ultrastable Na-ion storage. *ACS Appl Mater Interfaces* 2023;15:1367-75. DOI
 33. Yang G, Ilango PR, Wang S, et al. Carbon-based alloy-type composite anode materials toward sodium-ion batteries. *Small* 2019;15:e1900628. DOI
 34. Wang W, Wang B, Li Y, et al. Hard carbon derived from different precursors for sodium storage. *Chem Asian J* 2024;19:e202301146. DOI
 35. Veerasubramani GK, Park M, Nakate UT, et al. Intrinsically nitrogen-enriched biomass-derived hard carbon with enhanced performance as a sodium-ion battery anode. *Energy Fuels* 2024;38:7368-78. DOI
 36. Tang Y, He J, Peng J, et al. Electrochemical behavior of the biomass hard carbon derived from waste corncob as a sodium-ion battery anode. *Energy Fuels* 2024;38:7389-98. DOI
 37. Zhang G, Chen C, Xu C, et al. Unraveling the microcrystalline carbon evolution mechanism of biomass-derived hard carbon for sodium-ion batteries. *Energy Fuels* 2024;38:8326-36. DOI
 38. Molaiyan P, Dos Reis GS, Karupiah D, Subramaniyam CM, García-alvarado F, Lassi U. Recent progress in biomass-derived carbon materials for Li-ion and Na-ion batteries - a review. *Batteries* 2023;9:116. DOI
 39. Hu H, Xiao Y, Ling W, et al. A stable biomass-derived hard carbon anode for high-performance sodium-ion full battery. *Energy Tech* 2021;9:2000730. DOI
 40. Li N, Wang Y, Liu L, et al. "Self-doping" defect engineering in SnP₃@gamma-irradiated hard carbon anode for rechargeable sodium storage. *J Colloid Interface Sci* 2021;592:279-90. DOI
 41. Fang L, Bahlawane N, Sun W, et al. Conversion-alloying anode materials for sodium ion batteries. *Small* 2021;17:e2101137. DOI
 42. Li X, Guo Y, Hu Z, et al. Improving the initial coulombic efficiency of sodium-storage antimony anodes via electrochemically alloying bismuth. *ACS Appl Mater Interfaces* 2023;15:45926-37. DOI
 43. Zhang H, Hasa I, Passerini S. Beyond insertion for Na-ion batteries: nanostructured alloying and conversion anode materials. *Adv Energy Mater* 2018;8:1702582. DOI
 44. Zhao S, Guo Z, Yang J, Wang C, Sun B, Wang G. Nanoengineering of advanced carbon materials for sodium-ion batteries. *Small* 2021;17:e2007431. DOI
 45. Lu X, Adkins ER, He Y, et al. Germanium as a sodium ion battery material: *in situ* TEM reveals fast sodiation kinetics with high capacity. *Chem Mater* 2016;28:1236-42. DOI
 46. Chen Y, Li F, Guo Z, et al. Sustainable and scalable fabrication of high-performance hard carbon anode for Na-ion battery. *J Power Sources* 2023;557:232534. DOI
 47. Tang Z, Zhang R, Wang H, et al. Revealing the closed pore formation of waste wood-derived hard carbon for advanced sodium-ion battery. *Nat Commun* 2023;14:6024. DOI PubMed PMC

48. Perveen T, Siddiq M, Shahzad N, Ihsan R, Ahmad A, Shahzad MI. Prospects in anode materials for sodium ion batteries - a review. *Renew Sust Energy Rev* 2020;119:109549. DOI
49. Xiao B, Rojo T, Li X. Hard carbon as sodium-ion battery anodes: progress and challenges. *ChemSusChem* 2019;12:133-44. DOI PubMed
50. Fang S, Bresser D, Passerini S. Transition metal oxide anodes for electrochemical energy storage in lithium- and sodium-ion batteries*. In: Nanda J, Augustyn V, editors. *Transition metal oxides for electrochemical energy storage*. Wiley; 2022. pp. 55-99. DOI
51. Lim YV, Li XL, Yang HY. Recent tactics and advances in the application of metal sulfides as high-performance anode materials for rechargeable sodium-ion batteries. *Adv Funct Mater* 2021;31:2006761. DOI
52. Hao Z, Shi X, Yang Z, Li L, Chou S. Developing high-performance metal selenides for sodium-ion batteries. *Adv Funct Mater* 2022;32:2208093. DOI
53. Fan H, Mao P, Sun H, et al. Recent advances of metal telluride anodes for high-performance lithium/sodium-ion batteries. *Mater Horiz* 2022;9:524-46. DOI
54. Zhang W, Liu T, Wang Y, et al. Strategies to improve the performance of phosphide anodes in sodium-ion batteries. *Nano Energy* 2021;90:106475. DOI
55. Li G, Guo S, Xiang B, et al. Recent advances and perspectives of micro-sized alloying-type porous anode materials in high-performance Li- and Na-ion batteries. *Energy Mater* 2022;2:200020. DOI
56. Shao R, Sun Z, Wang L, et al. Resolving the origins of superior cycling performance of antimony anode in sodium-ion batteries: a comparison with lithium-ion batteries. *Angew Chem Int Ed* 2024;136:e202320183. DOI
57. Chen Z, Wu X, Sun Z, et al. Enhanced fast-charging and longevity in sodium-ion batteries through nitrogen-doped carbon frameworks encasing flower-like bismuth microspheres. *Adv Energy Mater* 2024;14:2400132. DOI
58. Yao Q, Zheng C, Liu K, et al. Bi nanospheres embedded in N-doped carbon nanowires facilitate ultrafast and ultrastable sodium storage. *Adv Sci* 2024:e2401730. DOI
59. Li W, Ke L, Wei Y, et al. Highly reversible sodium storage in a GeP₃/C composite anode with large capacity and low voltage. *J Mater Chem A* 2017;5:4413-20. DOI
60. Li X, Qu J, Zhao Y, Lai Q, Wang P, Yi T. Reaction mechanisms, recent progress and future prospects of tin selenide-based composites for alkali-metal-ion batteries. *Compos Part B Eng* 2022;242:110045. DOI
61. Wu X, Lan X, Hu R, Yao Y, Yu Y, Zhu M. Tin-based anode materials for stable sodium storage: progress and perspective. *Adv Mater* 2022;34:e2106895. DOI
62. Zheng C, Yao Q, Li R, et al. Construction of robust solid-electrolyte interphase via electrode additive for high-performance Sn-based anodes of sodium-ion batteries. *Energy Stor Mater* 2024;67:103334. DOI
63. Huang J, Guo X, Du X, et al. Nanostructures of solid electrolyte interphases and their consequences for micro-sized Sn anodes in sodium ion batteries. *Energy Environ Sci* 2019;12:1550-7. DOI
64. Duan YK, Li ZW, Zhang SC, et al. Stannate-based materials as anodes in lithium-ion and sodium-ion batteries: a review. *Molecules* 2023;28:5037. DOI PubMed PMC
65. Tian Z, Zou Y, Liu G, et al. Electrolyte solvation structure design for sodium ion batteries. *Adv Sci* 2022;9:e2201207. DOI PubMed PMC
66. Huang Y, Zhao L, Li L, Xie M, Wu F, Chen R. Electrolytes and electrolyte/electrode interfaces in sodium-ion batteries: from scientific research to practical application. *Adv Mater* 2019;31:e1808393. DOI
67. Mou H, Xiao W, Miao C, Li R, Yu L. Tin and tin compound materials as anodes in lithium-ion and sodium-ion batteries: a review. *Front Chem* 2020;8:141. DOI PubMed PMC
68. Liang J, Zhang L, Xili D, Kang J. Research progress on tin-based anode materials for sodium ion batteries. *Rare Met* 2020;39:1005-18. DOI
69. Sadan MK, Kim H, Kim C, et al. Ultra-long cycle life of flexible Sn anode using DME electrolyte. *J Alloys Compd* 2021;871:159549. DOI
70. Daali A, Zhou X, Zhao C, et al. In situ microscopy and spectroscopy characterization of micro-sized Sn anode for sodium-ion batteries. *Nano Energy* 2023;115:108753. DOI
71. Zheng C, Ji D, Yao Q, et al. Electrostatic shielding boosts electrochemical performance of alloy-type anode materials of sodium-ion batteries. *Angew Chem Int Ed* 2023;62:e202214258. DOI
72. Yao Q, Zhu Y, Zheng C, et al. Intermolecular cross-linking reinforces polymer binders for durable alloy-type anode materials of sodium-ion batteries. *Adv Energy Mater* 2023;13:2202939. DOI
73. Shen H, An Y, Man Q, et al. Chemical prelithiation/presodiation strategies toward controllable and scalable synthesis of micro-sized nanoporous tin at room temperature for high-energy sodium-ion batteries. *Adv Funct Mater* 2024;34:2309834. DOI
74. Ying H, Han WQ. Metallic Sn-based anode materials: application in high-performance lithium-ion and sodium-ion batteries. *Adv Sci* 2017;4:1700298. DOI PubMed PMC
75. Yang J, Guo X, Gao H, et al. A high-performance alloy-based anode enabled by surface and interface engineering for wide-temperature sodium-ion batteries. *Adv Energy Mater* 2023;13:2300351. DOI
76. Zhang S, Yue L, Wang M, Feng Y, Li Z, Mi J. SnO₂ nanoparticles confined by N-doped and CNTs-modified carbon fibers as superior anode material for sodium-ion battery. *Solid State Ionics* 2018;323:105-11. DOI

77. Ma D, Li Y, Mi H, et al. Robust SnO_{2-x} nanoparticle-impregnated carbon nanofibers with outstanding electrochemical performance for advanced sodium-ion batteries. *Angew Chem Int Ed* 2018;57:8901-5. DOI
78. Fan L, Song X, Xiong D, Li X. Nitrogen-doping of graphene enhancing sodium storage of SnO₂ anode. *J Electroanal Chem* 2019;833:340-8. DOI
79. Wang Y, Jin Y, Zhao C, Pan E, Jia M. 1D ultrafine SnO₂ nanorods anchored on 3D graphene aerogels with hierarchical porous structures for high-performance lithium/sodium storage. *J Colloid Interface Sci* 2018;532:352-62. DOI
80. Demir E, Aydin M, Arie AA, Demir-cakan R. Apricot shell derived hard carbons and their tin oxide composites as anode materials for sodium-ion batteries. *J Alloys Compd* 2019;788:1093-102. DOI
81. Choi IY, Jo C, Lim WG, et al. Amorphous Tin oxide nanohelix structure based electrode for highly reversible Na-ion batteries. *ACS Nano* 2019;13:6513-21. DOI
82. Han B, Zhang W, Gao D, et al. Encapsulating tin oxide nanoparticles into holey carbon nanotubes by melt infiltration for superior lithium and sodium ion storage. *J Power Sources* 2020;449:227564. DOI
83. Narsimulu D, Nagaraju G, Chandra Sekhar S, Ramulu B, Su Yu J. Three-dimensional porous SnO₂/carbon cloth electrodes for high-performance lithium- and sodium-ion batteries. *Appl Surf Sci* 2021;538:148033. DOI
84. Chen Y, Sun Y, Geng M, et al. SnO₂/MXene nanoparticles as a superior high-rate and cycling-stable anode for sodium ion batteries. *Mater Lett* 2021;304:130704. DOI
85. Wu YQ, Yang HX, Yang Y, et al. SnS₂/Co₃S₄ hollow nanocubes anchored on S-doped graphene for ultrafast and stable Na-ion storage. *Small* 2019;15:e1903873. DOI
86. He X, Liu J, Kang B, et al. Preparation of SnS₂/enteromorpha prolifera derived carbon composite and its performance of sodium-ion batteries. *J Phys Chem Solids* 2021;152:109976. DOI
87. Ding J, Tang C, Zhu G, et al. Integrating SnS₂ quantum dots with nitrogen-doped Ti₃C₂T_x MXene nanosheets for robust sodium storage performance. *ACS Appl Energy Mater* 2021;4:846-54. DOI
88. Jiang Y, Liu G, Lu S, et al. A novel interlayer-expanded tin disulfide/reduced graphene oxide nanocomposite as anode material for high-performance sodium-ion batteries. *J Colloid Interface Sci* 2022;611:215-23. DOI
89. Li Z, Zheng J, Xiao M, et al. Three-dimensional 1T-SnS₂ wrapped with graphene for sodium-ion battery anodes with highly reversible sodiation/desodiation. *Scr Mater* 2022;211:114500. DOI
90. Li Q, Yu F, Cui Y, Wang J, Zhao Y, Peng J. Multilayer SnS-SnS₂@GO heterostructures nanosheet as anode material for Sodium ion battery with high capacity and stability. *J Alloys Compd* 2023;937:168392. DOI
91. Yang X, Miao Z, Zhong Q, et al. ZnS/SnS₂ heterostructures encapsulated in N-doped carbon nanofibers for high-performance alkali metal-ion batteries. *ACS Appl Mater Interfaces* 2023;15:46881-94. DOI
92. Huang S, Wang M, Jia P, Wang B, Zhang J, Zhao Y. N-graphene motivated SnO₂@SnS₂ heterostructure quantum dots for high performance lithium/sodium storage. *Energy Stor Mater* 2019;20:225-33. DOI
93. Ou X, Cao L, Liang X, et al. Fabrication of SnS₂/Mn₂SnS₄/Carbon heterostructures for sodium-ion batteries with high initial coulombic efficiency and cycling stability. *ACS Nano* 2019;13:3666-76. DOI
94. Zhang F, Shen Y, Shao M, et al. SnSe₂ nanoparticles chemically embedded in a carbon shell for high-rate sodium-ion storage. *ACS Appl Mater Interfaces* 2020;12:2346-53. DOI
95. Yang W, Chen Y, Yin X, Lai X, Wang J, Jian J. SnSe nanosheet array on carbon cloth as a high-capacity anode for sodium-ion batteries. *ACS Appl Mater Interfaces* 2023;15:42811-22. DOI
96. Liu P, Han J, Zhu K, Dong Z, Jiao L. Heterostructure SnSe₂/ZnSe@PDA nanobox for stable and highly efficient sodium-ion storage. *Adv Energy Mater* 2020;10:2000741. DOI
97. Fan T, Wu Y, Li J, et al. Sheet-to-layer structure of SnSe₂/MXene composite materials for advanced sodium ion battery anodes. *New J Chem* 2021;45:1944-52. DOI
98. Wang W, Hu L, Li L, et al. Constructing a rapid ion and electron migration channels in MoSe₂/SnSe₂@C 2D heterostructures for high-efficiency sodium-ion half/full batteries. *Electrochim Acta* 2023;449:142239. DOI
99. Kong Z, Liang Z, Huang M, et al. Yolk-shell tin phosphides composites as superior reversibility and stability anodes for lithium/sodium ion batteries. *J Alloys Compd* 2023;930:167328. DOI
100. Liu C, Yang X, Liu J, Ye X. Theoretical prediction of two-dimensional SnP₃ as a promising anode material for Na-ion batteries. *ACS Appl Energy Mater* 2018;1:3850-9. DOI
101. Kong Z, Yao X, Shao Y, et al. Sn_xP_y nanoplate/reduced graphene oxide composites as anode materials for lithium-/sodium-ion batteries. *ACS Appl Nano Mater* 2021;4:12335-45. DOI
102. Pan E, Jin Y, Zhao C, et al. Mesoporous Sn₄P₃-graphene aerogel composite as a high-performance anode in sodium ion batteries. *Appl Surf Sci* 2019;475:12-9. DOI
103. Pan E, Jin Y, Zhao C, et al. Conformal hollow carbon sphere coated on Sn₄P₃ microspheres as high-rate and cycle-stable anode materials with superior sodium storage capability. *ACS Appl Energy Mater* 2019;2:1756-64. DOI
104. Zhang J, Wang W, Li B. Enabling high sodium storage performance of micron-sized Sn₄P₃ anode via diglyme-derived solid electrolyte interphase. *Chem Eng J* 2020;392:123810. DOI
105. Ran L, Luo B, Gentle IR, et al. Biomimetic Sn₄P₃ anchored on carbon nanotubes as an anode for high-performance sodium-ion batteries. *ACS Nano* 2020;14:8826-37. DOI
106. Fan W, Gao Y, Hui Q, et al. A closed-ended MXene armor on hollow Sn₄P₃ nanospheres for ultrahigh-rate and stable sodium storage.

- Chem Eng J* 2023;465:142963. DOI
107. Fan W, Gao Y, Liu H, Xia X. Rational design of conductive MXenes-based networks by Sn and Sn_4P_3 nanoparticles for durable sodium-ion battery. *J Power Sources* 2023;562:232750. DOI
 108. Baggetto L, Ganesh P, Sun C, Meisner RA, Zawodzinski TA, Veith GM. Intrinsic thermodynamic and kinetic properties of Sb electrodes for Li-ion and Na-ion batteries: experiment and theory. *J Mater Chem A* 2013;1:7985. DOI
 109. Liu Y, Zhou B, Liu S, Ma Q, Zhang WH. Galvanic replacement synthesis of highly uniform sb nanotubes: reaction mechanism and enhanced sodium storage performance. *ACS Nano* 2019;13:5885-92. DOI
 110. Qian J, Chen Y, Wu L, Cao Y, Ai X, Yang H. High capacity Na-storage and superior cyclability of nanocomposite Sb/C anode for Na-ion batteries. *Chem Commun* 2012;48:7070-2. DOI
 111. Xu X, Dou Z, Gu E, Si L, Zhou X, Bao J. Uniformly-distributed Sb nanoparticles in ionic liquid-derived nitrogen-enriched carbon for highly reversible sodium storage. *J Mater Chem A* 2017;5:13411-20. DOI
 112. Wu C, Shen L, Chen S, et al. Top-down synthesis of interconnected two-dimensional carbon/antimony hybrids as advanced anodes for sodium storage. *Energy Stor Mater* 2018;10:122-9. DOI
 113. Kong B, Zu L, Peng C, et al. Direct superassemblies of freestanding metal-carbon frameworks featuring reversible crystalline-phase transformation for electrochemical sodium storage. *J Am Chem Soc* 2016;138:16533-41. DOI
 114. Park J, Kim M, Choi M, et al. Sb/C composite embedded in SiOC buffer matrix via dispersion property control for novel anode material in sodium-ion batteries. *J Power Sources* 2023;568:232908. DOI
 115. Liu Y, Qing Y, Zhou B, et al. Yolk-shell Sb@Void@Graphdiyne nanoboxes for high-rate and long cycle life sodium-ion batteries. *ACS Nano* 2023;17:2431-9. DOI
 116. Nieto K, Windsor DS, Kale AR, Gallawa JR, Medina DA, Prieto AL. Structural control of electrodeposited sb anodes through solution additives and their influence on electrochemical performance in Na-ion batteries. *J Phys Chem C* 2023;127:12415-27. DOI
 117. Zheng X, You J, Fan J, et al. Electrodeposited binder-free Sb/NiSb anode of sodium-ion batteries with excellent cycle stability and rate capability and new insights into its reaction mechanism by operando XRD analysis. *Nano Energy* 2020;77:105123. DOI
 118. Baggetto L, Allcorn E, Unocic RR, Manthiram A, Veith GM. Mo_3Sb_7 as a very fast anode material for lithium-ion and sodium-ion batteries. *J Mater Chem A* 2013;1:11163. DOI
 119. Song Z, Wang G, Chen Y, Lu Y, Wen Z. In situ three-dimensional cross-linked carbon nanotube-interspersed SnSb@CNF as freestanding anode for long-term cycling sodium-ion batteries. *Chem Eng J* 2023;463:142289. DOI
 120. Shen H, Zheng X, Kang Q, et al. High-performance and sodiation mechanism of a pulse potential-electrodeposited Sb-Zn alloy as an anode for sodium-ion batteries. *Appl Surf Sci* 2023;609:155243. DOI
 121. Chen B, Liang M, Wu Q, Zhu S, Zhao N, He C. Recent developments of antimony-based anodes for sodium- and potassium-ion batteries. *Trans Tianjin Univ* 2022;28:6-32. DOI
 122. Zhou X, Deng H, Wang A, Song J, Lei Z, Xu Y. Antimony oxides-based anode materials for alkali metal-ion storage. *Chemistry* 2023;29:e202300506. DOI PubMed
 123. Deng M, Li S, Hong W, et al. Octahedral Sb_2O_3 as high-performance anode for lithium and sodium storage. *Mater Chem Phys* 2019;223:46-52. DOI
 124. Kim S, Qu S, Zhang R, Braun PV. High volumetric and gravimetric capacity electrodeposited mesostructured Sb_2O_3 sodium ion battery anodes. *Small* 2019;15:e1900258. DOI
 125. Ma W, Wang J, Gao H, et al. A mesoporous antimony-based nanocomposite for advanced sodium ion batteries. *Energy Stor Mater* 2018;13:247-56. DOI
 126. Li D, Li J, Cao J, Fu X, Zhou L, Han W. Highly flexible free-standing $\text{Sb/Sb}_2\text{O}_3$ @N-doped carbon nanofiber membranes for sodium ion batteries with excellent stability. *Sustain Energy Fuels* 2020;4:5732-8. DOI
 127. Ye J, Xia G, Zheng Z, Hu C. Facile controlled synthesis of coral-like nanostructured Sb_2O_3 @Sb anode materials for high performance sodium-ion batteries. *Int J Hydrogen Energy* 2020;45:9969-78. DOI
 128. Liao S, Wang X, Hu H, Chen D, Zhang M, Luo J. Carbon-encapsulated Sb_6O_{13} nanoparticles for an efficient and durable sodium-ion battery anode. *J Alloys Compd* 2021;852:156939. DOI
 129. Subramanyan K, Palmurukan MR, Lee Y, Aravindan V. Exfoliated graphene oxide@ Sb_2O_3 octahedrons as alloy-conversion anode for high-performance Na-ion batteries with P2-type $\text{Na}_{2/3}\text{Ni}_{1/3}\text{Mn}_{2/3}\text{O}_2$ cathode. *Electrochim Acta* 2023;470:143308. DOI
 130. Lakshmi K, Deivanayagam R, Shaijumon M. Carbon nanotube ‘wired’ octahedral Sb_2O_3 /graphene aerogel as efficient anode material for sodium and lithium ion batteries. *J Alloys Compd* 2021;857:158267. DOI
 131. Deng M, Li S, Hong W, et al. Natural stibnite ore (Sb_2S_3) embedded in sulfur-doped carbon sheets: enhanced electrochemical properties as anode for sodium ions storage. *RSC Adv* 2019;9:15210-6. DOI PubMed PMC
 132. Xie J, Xia J, Yuan Y, et al. Sb_2S_3 embedded in carbon-silicon oxide nanofibers as high-performance anode materials for lithium-ion and sodium-ion batteries. *J Power Sources* 2019;435:226762. DOI
 133. Huang Y, Wang Z, Jiang Y, et al. Conductivity and pseudocapacitance optimization of bimetallic antimony-indium sulfide anodes for sodium-ion batteries with favorable kinetics. *Adv Sci* 2018;5:1800613. DOI PubMed PMC
 134. Cao L, Gao X, Zhang B, Ou X, Zhang J, Luo WB. Bimetallic sulfide Sb_2S_3 @ FeS_2 hollow nanorods as high-performance anode materials for sodium-ion batteries. *ACS Nano* 2020;14:3610-20. DOI
 135. Lin J, Yao L, Zhang C, et al. Construction of Sb_2S_3 @ SnS@C tubular heterostructures as high-performance anode materials for sodium-ion batteries. *ACS Sustain Chem Eng* 2021;9:11280-9. DOI

136. Zhang H, Ren M, Jiang W, Yao J, Pan L, Yang J. Hierarchical $\text{Sb}_2\text{S}_3@\text{m-Ti}_3\text{C}_2\text{T}_x$ composite anode with enhanced Na-ion storage properties. *J Alloys Compd* 2021;887:161318. DOI
137. Li D, Li J, Liu H, et al. $\text{Ti}_3\text{C}_2\text{T}_x$ constrained Sb_2S_3 composite biomass-derived carbon ribbon film achieves stable sodium storage for flexible quasi-solid full-battery. *Chem Eng J* 2023;477:147045. DOI
138. Zhu M, Li J, Yang X, Li X, Wang L, Lü W. 3D reduced graphene oxide wrapped $\text{MoS}_2@\text{Sb}_2\text{S}_3$ heterostructures for high performance sodium-ion batteries. *Appl Surf Sci* 2023;624:157106. DOI
139. Ou X, Yang C, Xiong X, et al. A new rGO-overcoated Sb_2Se_3 nanorods anode for Na^+ battery: in situ X-ray diffraction study on a live sodiation/desodiation process. *Adv Funct Mater* 2017;27:1606242. DOI
140. Li J, Zhang W, Zheng W. Metal selenides find plenty of space in architecting advanced sodium/potassium ion batteries. *Small* 2024;20:e2305021. DOI
141. Nam K, Park C. 2D layered Sb_2Se_3 -based amorphous composite for high-performance Li- and Na-ion battery anodes. *J Power Sources* 2019;433:126639. DOI
142. Wang Y, Cao D, Zhang K, et al. Cation-exchange construction of $\text{ZnSe/Sb}_2\text{Se}_3$ hollow microspheres coated by nitrogen-doped carbon with enhanced sodium ion storage capability. *Nanoscale* 2020;12:17915-24. DOI
143. Ihsan-ul-haq M, Huang H, Wu J, et al. Unveiling solid electrolyte interface morphology and electrochemical kinetics of amorphous $\text{Sb}_2\text{Se}_3/\text{CNT}$ composite anodes for ultrafast sodium storage. *Carbon* 2021;171:119-29. DOI
144. Hu L, Pan J, Zhao P, Shi G, Wang B, Huang F. A new method of synthesis of $\text{Sb}_2\text{Se}_3/\text{rGO}$ as a high-rate and low-temperature anode for sodium-ion batteries. *Mater Adv* 2022;3:3554-61. DOI
145. Chong S, Ma M, Yuan L, et al. Hierarchical encapsulation and rich sp^2N assist Sb_2Se_3 -based conversion-alloying anode for long-life sodium- and potassium-ion storage. *Energy Environ Mater* 2023;6:e12458. DOI
146. Yang J, Li J, Lu J, et al. Synergistically boosting reaction kinetics and suppressing polyselenide shuttle effect by $\text{Ti}_3\text{C}_2\text{T}_x/\text{Sb}_2\text{Se}_3$ film anode in high-performance sodium-ion batteries. *J Colloid Interf Sci* 2023;649:234-44. DOI
147. Wu Y, Luo W, Gao P, et al. Unveiling the microscopic origin of asymmetric phase transformations in (de)sodiated Sb_2Se_3 with in situ transmission electron microscopy. *Nano Energy* 2020;77:105299. DOI
148. Wang Y, Niu P, Li J, Wang S, Li L. Recent progress of phosphorus composite anodes for sodium/potassium ion batteries. *Energy Stor Mater* 2021;34:436-60. DOI
149. Dong S, Wang L, Huang X, Liang J, He X. Challenges and prospects of phosphorus-based anode materials for secondary batteries. *Batteries Supercaps* 2023;6:e202300265. DOI
150. Liu S, Xu H, Bian X, et al. Nanoporous red phosphorus on reduced graphene oxide as superior anode for sodium-ion batteries. *ACS Nano* 2018;12:7380-7. DOI
151. Hu Y, Li B, Jiao X, Zhang C, Dai X, Song J. Stable cycling of phosphorus anode for sodium-ion batteries through chemical bonding with sulfurized polyacrylonitrile. *Adv Funct Mater* 2018;28:1801010. DOI
152. Capone I, Hurlbutt K, Naylor AJ, Xiao AW, Pasta M. Effect of the particle-size distribution on the electrochemical performance of a red phosphorus-carbon composite anode for sodium-ion batteries. *Energy Fuels* 2019;33:4651-8. DOI PubMed PMC
153. Xiao W, Sun Q, Banis MN, et al. Unveiling the interfacial instability of the phosphorus/carbon anode for sodium-ion batteries. *ACS Appl Mater Interf* 2019;11:30763-73. DOI
154. Liu W, Ju S, Yu X. Phosphorus-amine-based synthesis of nanoscale red phosphorus for application to sodium-ion batteries. *ACS Nano* 2020;14:974-84. DOI PubMed
155. Fang K, Liu D, Xiang X, et al. Air-stable red phosphorus anode for potassium/sodium-ion batteries enabled through dual-protection design. *Nano Energy* 2020;69:104451. DOI
156. Jin H, Lu H, Wu W, et al. Tailoring conductive networks within hollow carbon nanospheres to host phosphorus for advanced sodium ion batteries. *Nano Energy* 2020;70:104569. DOI
157. Liu Y, Liu Q, Jian C, et al. Red-phosphorus-impregnated carbon nanofibers for sodium-ion batteries and liquefaction of red phosphorus. *Nat Commun* 2020;11:2520. DOI PubMed PMC
158. Subramaniyam CM, Kang MA, Li J, VahidMohammadi A, Hamed MM. Additive-free red phosphorus/ $\text{Ti}_3\text{C}_2\text{T}_x$ MXene nanocomposite anodes for metal-ion batteries. *Energy Adv* 2022;1:999-1008. DOI
159. Zhu Z, Pei Z, Liu B, et al. Hierarchical ion/electron networks enable efficient red phosphorus anode with high mass loading for sodium ion batteries. *Adv Funct Mater* 2022;32:2110444. DOI
160. Kaur H, Konkena B, Gabbett C, et al. Amorphous 2D-nanoplatelets of red phosphorus obtained by liquid-phase exfoliation yield high areal capacity Na-ion battery anodes. *Adv Energy Mater* 2023;13:2203013. DOI
161. Li Z, Zhao H. Recent developments of phosphorus-based anodes for sodium ion batteries. *J Mater Chem A* 2018;6:24013-30. DOI
162. Chang G, Zhao Y, Dong L, et al. A review of phosphorus and phosphides as anode materials for advanced sodium-ion batteries. *J Mater Chem A* 2020;8:4996-5048. DOI
163. Zhou J, Shi Q, Ullah S, et al. Phosphorus-based composites as anode materials for advanced alkali metal ion batteries. *Adv Funct Mater* 2020;30:2004648. DOI
164. Shen H, Han X, Zheng X, et al. One-step electrochemical synthesis and optimization of Sb-Co-P alloy anode for sodium ion battery. *Electrochim Acta* 2023;438:141529. DOI
165. Zhang N, Chen X, Zhao J, He P, Ding X. Mass produced Sb/P@C composite nanospheres for advanced sodium-ions battery anodes. *Electrochim Acta* 2023;439:141602. DOI

166. Jung SC, Jung DS, Choi JW, Han YK. Atom-level understanding of the sodiation process in silicon anode material. *J Phys Chem Lett* 2014;5:1283-8. DOI PubMed
167. Liu C, Jiang Y, Meng C, Liu X, Li B, Xia S. Amorphous germanium nanomaterials as high-performance anode for lithium and sodium-ion batteries. *Adv Mater Technol* 2023;8:2201817. DOI
168. Li M, Zhang Z, Ge X, et al. Enhanced electrochemical properties of carbon coated Zn_2GeO_4 micron-rods as anode materials for sodium-ion batteries. *Chem Eng J* 2018;331:203-10. DOI
169. Tseng K, Huang S, Chang W, Tuan H. Synthesis of mesoporous germanium phosphide microspheres for high-performance lithium-ion and sodium-ion battery anodes. *Chem Mater* 2018;30:4440-7. DOI
170. Shen H, Ma Z, Yang B, et al. Sodium storage mechanism and electrochemical performance of layered GeP as anode for sodium ion batteries. *J Power Sources* 2019;433:126682. DOI
171. Li W, Li X, Liao J, et al. Structural design of Ge-based anodes with chemical bonding for high-performance Na-ion batteries. *Energy Stor Mater* 2019;20:380-7. DOI
172. Sung G, Nam K, Choi J, Park C. Germanium telluride: layered high-performance anode for sodium-ion batteries. *Electrochim Acta* 2020;331:135393. DOI
173. Wang C, Wang D, Ma X, et al. Isotropy-induced stress relaxation and strong-tolerance for high-rate and long-duration sodium storage by amorphous structure engineering. *Adv Funct Mater* 2022;32:2204687. DOI
174. Yanilmaz M, Cihanbeyoglu G, Kim J. Centrifugally spun binder-free n, s-doped Ge@PCNF anodes for Li-ion and Na-ion batteries. *ACS Omega* 2023;8:16987-95. DOI PubMed PMC
175. Li Y, Wu F, Li Y, et al. Multilevel gradient-ordered silicon anode with unprecedented sodium storage. *Adv Mater* 2024;36:e2310270. DOI
176. Arrieta U, Katcho NA, Arcelus O, Carrasco J. First-principles study of sodium intercalation in crystalline $\text{Na}_x\text{Si}_{24}$ ($0 \leq x \leq 4$) as anode material for Na-ion batteries. *Sci Rep* 2017;7:5350. DOI PubMed PMC
177. Majid A, Hussain K, Ud-din Khan S, Ud-din Khan S. First principles study of SiC as the anode in sodium ion batteries. *New J Chem* 2020;44:8910-21. DOI
178. Zhao Q, Huang Y, Hu X. A Si/C nanocomposite anode by ball milling for highly reversible sodium storage. *Electrochem Commun* 2016;70:8-12. DOI
179. Han Y, Lin N, Xu T, et al. An amorphous Si material with a sponge-like structure as an anode for Li-ion and Na-ion batteries. *Nanoscale* 2018;10:3153-8. DOI
180. Jangid MK, Vemulapally A, Sonia FJ, Aslam M, Mukhopadhyay A. Feasibility of reversible electrochemical Na-storage and cyclic stability of amorphous silicon and silicon-graphene film electrodes. *J Electrochem Soc* 2017;164:A2559-65. DOI
181. Kempf A, Kiefer S, Graczyk-zajac M, Ionescu E, Riedel R. Tin-functionalized silicon oxycarbide as a stable, high-capacity anode material for Na-ion batteries. *Open Ceram* 2023;15:100388. DOI
182. Zhang Y, Tang YC, Li XT, et al. Porous amorphous silicon hollow nanoboxes coated with reduced graphene oxide as stable anodes for sodium-ion batteries. *ACS Omega* 2022;7:30208-14. DOI PubMed PMC
183. Zeng L, Liu R, Han L, et al. Preparation of a Si/SiO₂-ordered-mesoporous-carbon nanocomposite as an anode for high-performance lithium-ion and sodium-ion batteries. *Chemistry* 2018;24:4841-8. DOI
184. Kalisvaart WP, Olsen BC, Lubner EJ, Buriak JM. Sb-Si alloys and multilayers for sodium-ion battery anodes. *ACS Appl Energy Mater* 2019;2:2205-13. DOI
185. Gong H, Du T, Liu L, et al. Self-source silicon embedded in 2D biomass-based carbon sheet as anode material for sodium ion battery. *Appl Surf Sci* 2022;586:152759. DOI
186. Nazarian-samani M, Nazarian-samani M, Haghighat-shishavan S, Kim K. Predelithiation-driven ultrastable Na-ion battery performance using Si,P-rich ternary M-Si-P anodes. *Energy Stor Mater* 2022;49:421-32. DOI
187. Din MA, Li C, Zhang L, Han C, Li B. Recent progress and challenges on the bismuth-based anode for sodium-ion batteries and potassium-ion batteries. *Mater Today Phys* 2021;21:100486. DOI
188. Sun J, Li M, Oh JAS, Zeng K, Lu L. Recent advances of bismuth based anode materials for sodium-ion batteries. *Mater Technol* 2018;33:563-73. DOI
189. Park B, Lee S, Han D, et al. Multiscale hierarchical design of bismuth-carbon anodes for ultrafast-charging sodium-ion full battery. *Appl Surf Sci* 2023;614:156188. DOI
190. Hu C, Zhu Y, Ma G, et al. Sandwich-structured dual carbon modified bismuth nanosphere composites as long-cycle and high-rate anode materials for sodium-ion batteries. *Electrochim Acta* 2021;365:137379. DOI
191. Xue P, Wang N, Fang Z, et al. Rayleigh-instability-induced bismuth nanorod@nitrogen-doped carbon nanotubes as a long cycling and high rate anode for sodium-ion batteries. *Nano Lett* 2019;19:1998-2004. DOI
192. Yin H, Cao M, Yu X, et al. Self-standing Bi₂O₃ nanoparticles/carbon nanofiber hybrid films as a binder-free anode for flexible sodium-ion batteries. *Mater Chem Front* 2017;1:1615-21. DOI
193. Liu R, Yu L, He X, et al. Constructing heterointerface of Bi/Bi₂S₃ with built-in electric field realizes superior sodium-ion storage capability. *eScience* 2023;3:100138. DOI
194. Lin J, Lu S, Zhang Y, Zeng L, Zhang Y, Fan H. Selenide-doped bismuth sulfides (Bi₂S_{3-x}Se_x) and their hierarchical heterostructure with ReS₂ for sodium/potassium-ion batteries. *J Colloid Interf Sci* 2023;645:654-62. DOI
195. Pang S, Hu Z, Fan C, et al. Insights into the sodium storage mechanism of Bi₂Te₃ nanosheets as superior anodes for sodium-ion

- batteries. *Nanoscale* 2022;14:1755-66. DOI
196. Meija R, Lazarenko V, Rublova Y, et al. Electrochemical properties of bismuth chalcogenide/MXene/CNT heterostructures for application in Na-ion batteries. *Sustain Mater Technol* 2023;38:e00768. DOI
 197. Wang Y, Xu X, Li F, et al. Rational design of bismuth metal anodes for sodium-/potassium-ion batteries: recent advances and perspectives. *Batteries* 2023;9:440. DOI
 198. Li X, Ni J, Savilov SV, Li L. Materials based on antimony and bismuth for sodium storage. *Chemistry* 2018;24:13719-27. DOI
 199. Ellis LD, Wilkes BN, Hatchard TD, Obrovac MN. In situ XRD study of silicon, lead and bismuth negative electrodes in nonaqueous sodium cells. *J Electrochem Soc* 2014;161:A416-21. DOI
 200. Sottmann J, Herrmann M, Vajeeston P, et al. How crystallite size controls the reaction path in nonaqueous metal ion batteries: the example of sodium bismuth alloying. *Chem Mater* 2016;28:2750-6. DOI
 201. Zhang X, Qiu X, Lin J, et al. Structure and interface engineering of ultrahigh-rate 3D bismuth anodes for sodium-ion batteries. *Small* 2023;19:e2302071. DOI
 202. Liang Y, Song N, Zhang Z, et al. Integrating Bi@C nanospheres in porous hard carbon frameworks for ultrafast sodium storage. *Adv Mater* 2022;34:e2202673. DOI
 203. Liu Y, Wang Y, Wang H, et al. Binder-free 3D hierarchical Bi Nanosheet/CNTs arrays anode for full sodium-ion battery with high voltage above 4 V. *J Power Sources* 2022;540:231639. DOI
 204. Pu B, Liu Y, Bai J, et al. Iodine-ion-assisted galvanic replacement synthesis of bismuth nanotubes for ultrafast and ultrastable sodium storage. *ACS Nano* 2022;16:18746-56. DOI
 205. Zhang W, Cao P, Li L, et al. Carbon-encapsulated 1D SnO₂/NiO heterojunction hollow nanotubes as high-performance anodes for sodium-ion batteries. *Chem Eng J* 2018;348:599-607. DOI
 206. Li R, Zhang G, Zhang P, et al. Accelerating ion transport via in-situ formation of built-in electric field for fast charging sodium-ion batteries. *Chem Eng J* 2022;450:138019. DOI
 207. Chen Y, Liu H, Guo X, et al. Bimetallic sulfide SnS₂/FeS₂ nanosheets as high-performance anode materials for sodium-ion batteries. *ACS Appl Mater Interf* 2021;13:39248-56. DOI
 208. Zhou J, Dou Q, Zhang L, et al. A novel and fast method to prepare a Cu-supported α-Sb₂S₃@CuSbS₂ binder-free electrode for sodium-ion batteries. *RSC Adv* 2020;10:29567-74. DOI PubMed PMC
 209. Li X, Qu J, Hu Z, Xie H, Yin H. Electrochemically converting Sb₂S₃/CNTs to Sb/CNTs composite anodes for sodium-ion batteries. *Int J Hydrogen Energy* 2021;46:17071-83. DOI
 210. Li D, Yuan Z, Li J, et al. A bioconfined synthesis strategy of Sb₂S₃@N-doped carbon ribbons for boosting ultralong-life sodium storage. *J Power Sources* 2022;546:231875. DOI
 211. Zhou J, Ding Y, Dou Q, et al. Enhancing sodium-ion batteries performance enabled by three-dimensional nanoflower Sb₂S₃@rGO anode material. *Mater Chem Phys* 2023;303:127837. DOI
 212. Li K, Yue L, Hu J, et al. Construction of hollow core-shell Sb₂S₃/S@S-doped C composite based on complexation reaction for high performance anode of sodium-ion batteries. *Appl Surf Sci* 2023;613:156111. DOI
 213. Dong C, Shao H, Zhou Y, et al. Construction of ZnS/Sb₂S₃ heterojunction as an ion-transport booster toward high-performance sodium storage. *Adv Funct Mater* 2023;33:2211864. DOI
 214. Liu W, Du L, Ju S, et al. Encapsulation of red phosphorus in carbon nanocages with ultrahigh content for high-capacity and long cycle life sodium-ion batteries. *ACS Nano* 2021;15:5679-88. DOI
 215. Liu X, Xiao B, Daali A, et al. Stress- and interface-compatible red phosphorus anode for high-energy and durable sodium-ion batteries. *ACS Energy Lett* 2021;6:547-56. DOI
 216. Ma X, Ji C, Li X, Liu Y, Xiong X. Red@Black phosphorus core-shell heterostructure with superior air stability for high-rate and durable sodium-ion battery. *Mater Today* 2022;59:36-45. DOI
 217. Song J, Wu M, Fang K, Tian T, Wang R, Tang H. NaF-rich interphase and high initial coulombic efficiency of red phosphorus anode for sodium-ion batteries by chemical presodiation. *J Colloid Interf Sci* 2023;630:443-52. DOI
 218. Saddique J, Zhang X, Wu T, et al. Enhanced silicon diphosphide-carbon composite anode for long-cycle, high-efficient sodium ion batteries. *ACS Appl Energy Mater* 2019;2:2223-9. DOI
 219. Ababaikeri R, Sun Y, Wang X, et al. Scalable fabrication of Bi@N-doped carbon as anodes for sodium/potassium-ion batteries with enhanced electrochemical performances. *J Alloys Compd* 2023;935:168207. DOI
 220. He B, Cunha J, Hou Z, Li G, Yin H. 3D hierarchical self-supporting Bi₂Se₃-based anode for high-performance lithium/sodium-ion batteries. *J Colloid Interf Sci* 2023;650:857-64. DOI
 221. Wang M, Li H, Cheng X, Tian S, Wang X. Graphene-encapsulated nitrogen-doped carbon@Bi enables rapid, ultrahigh and durable sodium storage. *Batteries Supercaps* 2023;6:e202300055. DOI
 222. Chen J, Zhang G, Xiao J, et al. A stress self-adaptive bimetallic stellar nanosphere for high-energy sodium-ion batteries. *Adv Funct Mater* 2024;34:2307959. DOI
 223. Wei S, Li W, Ma Z, Deng X, Li Y, Wang X. Novel bismuth nanoflowers encapsulated in N-doped carbon frameworks as superb composite anodes for high-performance sodium-ion batteries. *Small* 2023;19:e2304265. DOI
 224. Wang J, Bai W, Zhou Y, et al. Sea cucumber-inspired multi-phase metal sulfides with hierarchical structure towards energy storage with promoted safety. *J Energy Stor* 2024;76:109743. DOI
 225. Hu K, Chen Y, Zheng C, et al. Molten salt-assisted synthesis of bismuth nanosheets with long-term cyclability at high rates for

- sodium-ion batteries. *RSC Adv* 2023;13:25552-60. DOI PubMed PMC
226. Ma D, Cao Z, Hu A. Si-based anode materials for Li-ion batteries: a mini review. *Nanomicro Lett* 2014;6:347-58. DOI PubMed PMC
227. Pan Q, Wu Y, Zheng F, et al. Facile synthesis of M-Sb (M = Ni, Sn) alloy nanoparticles embedded in N-doped carbon nanosheets as high performance anode materials for lithium ion batteries. *Chem Eng J* 2018;348:653-60. DOI
228. Guo S, Feng Y, Wang L, Jiang Y, Yu Y, Hu X. Architectural engineering achieves high-performance alloying anodes for lithium and sodium ion batteries. *Small* 2021;17:e2005248. DOI
229. Ma D, Li Y, Zhang P, Lin Z. Oxygen vacancy engineering in tin(IV) oxide based anode materials toward advanced sodium-ion batteries. *ChemSusChem* 2018;11:3693-703. DOI
230. Liang S, Cheng Y, Zhu J, Xia Y, Müller-buschbaum P. A chronicle review of nonsilicon (Sn, Sb, Ge)-based lithium/sodium-ion battery alloying anodes. *Small Methods* 2020;4:2000218. DOI
231. Wang X, Feng B, Huang L, et al. Superior electrochemical performance of Sb-Bi alloy for sodium storage: understanding from alloying element effects and new cause of capacity attenuation. *J Power Sources* 2022;520:230826. DOI
232. Zheng Y, Wei S, Shang J, Wang D, Lei C, Zhao Y. High-performance sodium-ion batteries enabled by 3D nanoflowers comprised of ternary Sn-based dichalcogenides embedded in nitrogen and sulfur dual-doped carbon. *Small* 2023;19:e2303746. DOI
233. Gao H, Wang Y, Guo Z, et al. Dealloying-induced dual-scale nanoporous indium-antimony anode for sodium/potassium ion batteries. *J Energy Chem* 2022;75:154-63. DOI
234. Fu R, Pan J, Wang M, et al. In situ atomic-scale deciphering of multiple dynamic phase transformations and reversible sodium storage in ternary metal sulfide anode. *ACS Nano* 2023;17:12483-98. DOI
235. Wu J, Ihsan-ul-haq M, Chen Y, Kim J. Understanding solid electrolyte interphases: advanced characterization techniques and theoretical simulations. *Nano Energy* 2021;89:106489. DOI
236. Peled E, Menkin S. Review - SEI: past, present and future. *J Electrochem Soc* 2017;164:A1703-19. DOI
237. Yu F, Du L, Zhang G, Su F, Wang W, Sun S. Electrode engineering by atomic layer deposition for sodium-ion batteries: from traditional to advanced batteries. *Adv Funct Mater* 2020;30:1906890. DOI
238. Yadav P, Shelke V, Patrike A, Shelke M. Sodium-based batteries: development, commercialization journey and new emerging chemistries. *Oxford Open Mater Sci* 2023;3:itac019. DOI
239. Eddie Spence, Annie Lee; Bloomberg. Tesla rival BYD and other battery giants are betting on sodium for EVs and energy storage - and challenging the dominance of lithium-ion. Available from: <https://fortune.com/2023/11/26/battery-giants-sodium-bet-electric-vehicles-energy-storage-lithium-ion/> [Last accessed on 1 Jul 2024].
240. Gebert F, Knott J, Gorkin R, Chou S, Dou S. Polymer electrolytes for sodium-ion batteries. *Energy Stor Mater* 2021;36:10-30. DOI
241. Li Y, Wu F, Li Y, et al. Ether-based electrolytes for sodium ion batteries. *Chem Soc Rev* 2022;51:4484-536. DOI
242. Sirengo K, Babu A, Brennan B, Pillai SC. Ionic liquid electrolytes for sodium-ion batteries to control thermal runaway. *J Energy Chem* 2023;81:321-38. DOI
243. Westman K, Dugas R, Jankowski P, et al. Diglyme based electrolytes for sodium-ion batteries. *ACS Appl Energy Mater* 2018;1:2671-80. DOI
244. Kulova TL, Skundin AM. Electrode/electrolyte interphases of sodium-ion batteries. *Energies* 2022;15:8615. DOI
245. Usui H, Domi Y, Fujiwara K, et al. Charge-discharge properties of a Sn_4P_3 negative electrode in ionic liquid electrolyte for Na-ion batteries. *ACS Energy Lett* 2017;2:1139-43. DOI
246. Domingues LS, de Melo HG, Martins VL. Ionic liquids as potential electrolytes for sodium-ion batteries: an overview. *Phys Chem Chem Phys* 2023;25:12650-67. DOI PubMed
247. Ahmad H, Kubra KT, Butt A, Nisar U, Ifikhar FJ, Ali G. Recent progress, challenges, and perspectives in the development of solid-state electrolytes for sodium batteries. *J Power Sources* 2023;581:233518. DOI
248. Gandi S, Chidambara Swamy Vaddadi VS, Sripada Panda SS, et al. Recent progress in the development of glass and glass-ceramic cathode/solid electrolyte materials for next-generation high capacity all-solid-state sodium-ion batteries: a review. *J Power Sources* 2022;521:230930. DOI
249. Tripathi AM, Su WN, Hwang BJ. In situ analytical techniques for battery interface analysis. *Chem Soc Rev* 2018;47:736-851. DOI PubMed
250. Zhou L, Cao Z, Wahyudi W, et al. Electrolyte engineering enables high stability and capacity alloying anodes for sodium and potassium ion batteries. *ACS Energy Lett* 2020;5:766-76. DOI
251. Zhang J, Gai J, Song K, Chen W. Advances in electrode/electrolyte interphase for sodium-ion batteries from half cells to full cells. *Cell Rep Phys Sci* 2022;3:100868. DOI
252. Li Z, Wu Z, Wu S, et al. Designing advanced polymeric binders for high-performance rechargeable sodium batteries. *Adv Funct Mater* 2024;34:2307261. DOI
253. Chen H, Zhang S, Liu G, Yan C. Polymeric binders in modern metal-ion batteries. In: Zhang S, Lu J, editors. Functional polymers for metal-ion batteries. New York: Wiley; 2023. pp. 61-117. DOI
254. Li RR, Yang Z, He XX, et al. Binders for sodium-ion batteries: progress, challenges and strategies. *Chem Commun* 2021;57:12406-16. DOI
255. Bresser D, Buchholz D, Moretti A, Varzi A, Passerini S. Alternative binders for sustainable electrochemical energy storage - the transition to aqueous electrode processing and bio-derived polymers. *Energy Environ Sci* 2018;11:3096-127. DOI

256. Rasheed T, Anwar MT, Naveed A, Ali A. Biopolymer based materials as alternative greener binders for sustainable electrochemical energy storage applications. *ChemistrySelect* 2022;7:e202203202. DOI
257. Feng J, Wang L, Li D, Lu P, Hou F, Liang J. Enhanced electrochemical stability of carbon-coated antimony nanoparticles with sodium alginate binder for sodium-ion batteries. *Prog Nat Sci* 2018;28:205-11. DOI
258. Patra J, Rath PC, Li C, et al. A water-soluble NaCMC/NaPAA binder for exceptional improvement of sodium-ion batteries with an SnO₂-ordered mesoporous carbon anode. *ChemSusChem* 2018;11:3923-31. DOI
259. Sarkar S, Roy S, Zhao Y, Zhang J. Recent advances in semimetallic pnictogen (As, Sb, Bi) based anodes for sodium-ion batteries: structural design, charge storage mechanisms, key challenges and perspectives. *Nano Res* 2021;14:3690-723. DOI
260. Zhang Y, Su Q, Xu W, et al. A confined replacement synthesis of bismuth nanodots in MOF derived carbon arrays as binder-free anodes for sodium-ion batteries. *Adv Sci* 2019;6:1900162. DOI
261. Choi Y, Lee J. Continuous/reversible phase transition behaviors and their effect on the hysteresis energy loss of the anodes in Na-ion batteries. *Electrochim Acta* 2019;328:135106. DOI
262. Huang Z, Zheng X, Liu H, et al. Long cycle life and high-rate sodium metal batteries enabled by an active/inactive Co-Sn alloy interface. *Adv Funct Mater* 2024;34:2302062. DOI
263. Sarkar S, Mukherjee PP. Synergistic voltage and electrolyte mediation improves sodiation kinetics in μ -Sn alloy-anodes. *Energy Stor Mater* 2021;43:305-16. DOI
264. Wang XZ, Zuo Y, Qin Y, et al. Fast Na⁺ kinetics and suppressed voltage hysteresis enabled by a high-entropy strategy for sodium oxide cathodes. *Adv Mater* 2024;36:e2312300. DOI
265. Liu G, Sun Z, Shi X, et al. 2D-layer-structure Bi to quasi-1D-structure NiBi₃: structural dimensionality reduction to superior sodium and potassium ion storage. *Adv Mater* 2023;35:e2305551. DOI
266. Feng D, Tang S, Xu H, Zeng T. High performance sodium-ion anodes based on FeSb₂S₄/Sb embedded within porous reduced graphene oxide/carbon nanotubes matrix. *J Alloys Compd* 2023;931:167576. DOI
267. Li C, Pei YR, Zhao M, Yang CC, Jiang Q. Sodium storage performance of ultrasmall SnSb nanoparticles. *Chem Eng J* 2021;420:129617. DOI
268. Kang J, Lee JI, Choi S, Choi Y, Park S, Ryu J. Nonporous oxide-terminated multicomponent bulk anode enabling energy-dense sodium-ion batteries. *ACS Appl Mater Interf* 2023;15:26576-84. DOI
269. Gandharapu P, Das A, Tripathi R, Srihari V, Poswal HK, Mukhopadhyay A. Facile and scalable development of high-performance carbon-free Tin-based anodes for sodium-ion batteries. *ACS Appl Mater Interf* 2023;15:37504-16. DOI PubMed
270. Cheng X, Li D, Peng S, et al. In-situ alloy-modified sodiophilic current collectors for anode-less sodium metal batteries. *Batteries* 2023;9:408. DOI
271. Patel PC, Awasthi S, Mishra PK, Lakharwal P, Kashyap J. Fe-as intermetallic alloys: a way out for sodium-ion batteries. *Energy Fuels* 2023;37:16062-71. DOI
272. Li H, He Y, Li X, et al. Pomegranate-like Sn-Ni nanoalloys@N-doped carbon nanocomposites as high-performance anode materials for Li-ion and Na-ion batteries. *Appl Surf Sci* 2023;611:155672. DOI
273. Li W, Yu C, Huang S, et al. Synergetic Sn incorporation-Zn substitution in copper-based sulfides enabling superior Na-ion storage. *Adv Mater* 2024;36:e2305957. DOI
274. Ye W, Feng Z, Xiong D, He M. Mesoporous C-covered Sn/SnO₂-Ni nanoalloy particles as anode materials for high-performance lithium/sodium-ion batteries. *Electrochim Acta* 2023;471:143401. DOI
275. Sohan A, Kumar A, Narayanan TN, Kollu P. Tin antimony alloy based reduced graphene oxide composite for fast charging sodium-ion batteries. *J Energy Stor* 2023;74:109312. DOI
276. Chen X, Zhang N, He P, Ding X. High-capacity Sb₂SnO₅ with controlled Sb/Sn phase modulation as advanced anode material for sodium-ion batteries. *J Alloys Compd* 2023;938:168472. DOI
277. Meng F, Chen X, Zhou H, et al. Controllable fabrication of Sn/Sb nanodomains improved Sb₂SnO₅ anodes for sodium ion batteries. *ChemistrySelect* 2023;8:e202302417. DOI
278. Bhar M, Pappu S, Bhattacharjee U, Bulusu SV, Rao TN, Martha SK. Designing a freestanding electrode of intermetallic Ni-Sn alloy deposit as an anode for lithium-ion and sodium-ion batteries. *J Electrochem Soc* 2023;170:040501. DOI
279. Priyanka P, Nalini B, Soundarya GG, Christopher Selvin P, Dutta DP. Effect of pulverisation on sulfide and tin antimonide anodes for sodium-ion batteries. *Front Energy Res* 2023;11:1266653. DOI
280. Hou H, Jing M, Yang Y, et al. Sb porous hollow microspheres as advanced anode materials for sodium-ion batteries. *J Mater Chem A* 2015;3:2971-7. DOI
281. Kebede MA. Tin oxide-based anodes for both lithium-ion and sodium-ion batteries. *Curr Opin Electrochem* 2020;21:182-7. DOI
282. Li Z, Zheng Y, Liu Q, et al. Recent advances in nanostructured metal phosphides as promising anode materials for rechargeable batteries. *J Mater Chem A* 2020;8:19113-32. DOI
283. Sang J, Zhang X, Liu K, et al. Effective coupling of amorphous selenium phosphide with high-conductivity graphene as resilient high-capacity anode for sodium-ion batteries. *Adv Funct Mater* 2023;33:2211640. DOI
284. Liu M, Zhang J, Sun Z, et al. Dual mechanism for sodium based energy storage. *Small* 2023;19:e2206922. DOI
285. Ru J, He T, Chen B, et al. Covalent assembly of MoS₂ nanosheets with SnS nanodots as linkages for lithium/sodium-ion batteries. *Angew Chem Int Ed* 2020;59:14621-7. DOI
286. Xu S, Dong H, Yang D, et al. Promising cathode materials for sodium-ion batteries from lab to application. *ACS Cent Sci*

- 2023;9:2012-35. DOI PubMed PMC
287. Dai Z, Mani U, Tan HT, Yan Q. Advanced cathode materials for sodium-ion batteries: what determines our choices? *Small Methods* 2017;1:1700098. DOI
288. Jing WT, Yang CC, Jiang Q. Recent progress on metallic Sn- and Sb-based anodes for sodium-ion batteries. *J Mater Chem A* 2020;8:2913-33. DOI
289. Lin K, Liu Q, Zhou Y, et al. Fluorine substitution and pre-sodiation strategies to boost energy density of V-based NASICON-structured SIBs: combined theoretical and experimental study. *Chem Eng J* 2023;463:142464. DOI
290. Li F, Yu X, Tang K, Peng X, Zhao Q, Li B. Chemical presodiation of alloy anodes with improved initial coulombic efficiencies for the advanced sodium-ion batteries. *J Appl Electrochem* 2023;53:9-18. DOI
291. Oh SM, Myung ST, Jang MW, Scrosati B, Hassoun J, Sun YK. An advanced sodium-ion rechargeable battery based on a tin-carbon anode and a layered oxide framework cathode. *Phys Chem Chem Phys* 2013;15:3827-33. DOI
292. Liu M, Yang Z, Shen Y, et al. Chemically presodiated Sb with a fluoride-rich interphase as a cycle-stable anode for high-energy sodium ion batteries. *J Mater Chem A* 2021;9:5639-47. DOI
293. He W, Chen K, Pathak R, et al. High-mass-loading Sn-based anode boosted by pseudocapacitance for long-life sodium-ion batteries. *Chem Eng J* 2021;414:128638. DOI
294. Chen S, Ao Z, Sun B, Xie X, Wang G. Porous carbon nanocages encapsulated with tin nanoparticles for high performance sodium-ion batteries. *Energy Stor Mater* 2016;5:180-90. DOI
295. Liu Y, Zhang N, Jiao L, Tao Z, Chen J. Ultrasmall Sn nanoparticles embedded in carbon as high-performance anode for sodium-ion batteries. *Adv Funct Mater* 2015;25:214-20. DOI
296. Nam DH, Kim TH, Hong KS, Kwon HS. Template-free electrochemical synthesis of Sn nanofibers as high-performance anode materials for Na-ion batteries. *ACS Nano* 2014;8:11824-35. DOI PubMed
297. Zhu Y, Yao Q, Shao R, et al. Microsized gray Tin as a high-rate and long-life anode material for advanced sodium-ion batteries. *Nano Lett* 2022;22:7976-83. DOI
298. Wang L, Ni Y, Lei K, Dong H, Tian S, Li F. 3D porous Tin created by tuning the redox potential acts as an advanced electrode for sodium-ion batteries. *ChemSusChem* 2018;11:3376-81. DOI
299. Chen B, Zhang H, Liang M, et al. NaCl-pinned antimony nanoparticles combined with ion-shuttle-induced graphitized 3D carbon to boost sodium storage. *Cell Rep Phys Sci* 2022;3:100891. DOI
300. Li X, Xiao S, Niu X, Chen JS, Yu Y. Efficient stress dissipation in well-aligned pyramidal SbSn alloy nanoarrays for robust sodium storage. *Adv Funct Mater* 2021;31:2104798. DOI
301. Ni J, Li X, Sun M, et al. Durian-inspired design of bismuth-antimony alloy arrays for robust sodium storage. *ACS Nano* 2020;14:9117-24. DOI
302. Zhang R, Yang Y, Guo L, Luo Y. A fast and high-efficiency electrochemical exfoliation strategy towards antimonene/carbon composites for selective lubrication and sodium-ion storage applications. *Phys Chem Chem Phys* 2022;24:4957-65. DOI
303. Tian W, Zhang S, Huo C, et al. Few-layer antimonene: anisotropic expansion and reversible crystalline-phase evolution enable large-capacity and long-life Na-ion batteries. *ACS Nano* 2018;12:1887-93. DOI
304. Gao H, Niu J, Zhang C, Peng Z, Zhang Z. A dealloying synthetic strategy for nanoporous bismuth-antimony anodes for sodium ion batteries. *ACS Nano* 2018;12:3568-77. DOI
305. Li W, Han C, Gu Q, Chou S, Liu HK, Dou SX. Three-dimensional electronic network assisted by TiN conductive pillars and chemical adsorption to boost the electrochemical performance of red phosphorus. *ACS Nano* 2020;14:4609-17. DOI
306. Wu Y, Xing F, Xu R, et al. Spatially confining and chemically bonding amorphous red phosphorus in the nitrogen doped porous carbon tubes leading to superior sodium storage performance. *J Mater Chem A* 2019;7:8581-8. DOI
307. Liu B, Zhang Q, Li L, et al. Encapsulating red phosphorus in ultralarge pore volume hierarchical porous carbon nanospheres for lithium/sodium-ion half/full batteries. *ACS Nano* 2019;13:13513-23. DOI
308. Liu D, Huang X, Qu D, et al. Confined phosphorus in carbon nanotube-backboned mesoporous carbon as superior anode material for sodium/potassium-ion batteries. *Nano Energy* 2018;52:1-10. DOI
309. Zhu L, Xu K, Fang Y, et al. Se-induced fibrous nano red P with superior conductivity for sodium batteries. *Adv Funct Mater* 2023;33:2302444. DOI
310. Guo X, Zhang W, Zhang J, et al. Boosting sodium storage in two-dimensional Phosphorene/Ti₃C₂T_x MXene nanoarchitectures with stable fluorinated interphase. *ACS Nano* 2020;14:3651-9. DOI
311. Sun J, Lee HW, Pasta M, et al. A phosphorene-graphene hybrid material as a high-capacity anode for sodium-ion batteries. *Nat Nanotechnol* 2015;10:980-5. DOI
312. Shuai H, Ge P, Hong W, et al. Electrochemically exfoliated phosphorene-graphene hybrid for sodium-ion batteries. *Small Methods* 2019;3:1800328. DOI
313. Liu Y, Liu Q, Zhang A, et al. Room-temperature pressure synthesis of layered black phosphorus-graphene composite for sodium-ion battery anodes. *ACS Nano* 2018;12:8323-9. DOI
314. Yang H, Xu R, Yao Y, Ye S, Zhou X, Yu Y. Multicore-shell Bi@N-doped carbon nanospheres for high power density and long cycle life sodium- and potassium-ion anodes. *Adv Funct Mater* 2019;29:1809195. DOI
315. Xiong P, Bai P, Li A, et al. Bismuth nanoparticle@carbon composite anodes for ultralong cycle life and high-rate sodium-ion batteries. *Adv Mater* 2019;31:e1904771. DOI

316. Cheng X, Yang H, Wei C, et al. Synergistic effect of 1D bismuth nanowires/2D graphene composites for high performance flexible anodes in sodium-ion batteries. *J Mater Chem A* 2023;11:8081-90. [DOI](#)
317. Guo S, Wei C, Wang L, et al. Micro-sized porous bulk bismuth caged by carbon for fast charging and ultralong cycling in sodium-ion batteries. *Cell Rep Phys Sci* 2023;4:101463. [DOI](#)
318. Cheng X, Shao R, Li D, et al. A self-healing volume variation three-dimensional continuous bulk porous bismuth for ultrafast sodium storage. *Adv Funct Mater* 2021;31:2011264. [DOI](#)
319. Wang C, Wang L, Li F, Cheng F, Chen J. Bulk bismuth as a high-capacity and ultralong cycle-life anode for sodium-ion batteries by coupling with glyme-based electrolytes. *Adv Mater* 2017;29:1702212. [DOI](#)
320. Hou D, Xia D, Gabriel E, et al. Spatial and temporal analysis of sodium-ion batteries. *ACS Energy Lett* 2021;6:4023-54. [DOI](#) [PubMed](#) [PMC](#)
321. Tang F, Wu Z, Yang C, et al. Synchrotron X-ray tomography for rechargeable battery research: fundamentals, setups and applications. *Small Methods* 2021;5:e2100557. [DOI](#)